DISSERTATION

submitted to the

Combined Faculty of Mathematics, Engineering and Natural Sciences

of Heidelberg University, Germany

for the degree of

Doctor of Natural Sciences

Put forward by

Johannes Anton Grimm, M.Sc.

born in: Aalen, Germany

Oral examination: April 30th, 2025

Investigation of a remote 32-channel whole-body coil for large field of view ^{1}H body imaging at 7 T

Referees: Prof. Dr. Mark E. Ladd
Prof. Dr. Leif Schröder

Für meine kleine Familie

Investigation of a remote 32-channel whole-body coil for large field of view ^{1}H body imaging at 7 T

This work aimed to evaluate the remote coil in comparison to existing local coils and to experimentally investigate the parallel transmit (pTx) capabilities of the remote coil through *in-vivo* measurements. The thesis was divided into two parts.

First, the transmit and receive performance of seven different local pTx coils and the remote coil (also in combination with a dedicated local receive array) were quantitatively assessed through phantom measurements. The remote coil demonstrated the largest excitation coverage in head-foot direction. Although, its maximum B_1^+ efficiency at the isocenter was 2.0 times lower than that of local transmit-receive coils, this limitation could be compensated with the four- or eight-fold higher total available power. While the best performing local transmit-receive coil enabled higher acceleration factors than the dedicated local receive array, the latter achieved the highest signal-to-noise ratio in the phantom's center.

Second, the pTx capabilities of the remote coil were investigated through *in-vivo* measurements. The first study demonstrated homogeneous liver excitation using static pTx. The second *in-vivo* study extended the excitation region to the whole abdomen, where two k_T-point pTx pulses were required for sufficient homogeneity across all subjects.

In conclusion, the remote coil, combined with a dedicated local receive array, represents the state-of-the-art for body imaging at 7 T. These findings highlight its potential for large field-of-excitation imaging and its necessity for translating UHF body MRI into clinical practice.

Untersuchung einer 32-Kanal-Ganzkörperspule mit großem Sichtfeld für die ^{1}H Körperbildgebung bei 7 T

Das Ziel dieser Arbeit war es, die Remote-Spule im Vergleich zu verschiedenen lokalen Spulen zu bewerten und die Fähigkeiten der Remote-Spule für parallele Sendemethoden (pTx) durch *In-vivo*-Messungen experimentell zu untersuchen. Die Arbeit wurde in zwei Teile gegliedert.

Zunächst wurde die Sende- und Empfangsperformance von sieben lokalen pTx-Spulen und der Remote-Spule (auch in Kombination mit einer dedizierten lokalen Empfangsspule) durch Phantommessungen quantitativ untersucht. Die Remote-Spule wies die größte Anregungsabdeckung in Kopf-Fuß-Richtung auf. Obwohl die maximale B_1^+-Effizienz im Isozentrum 2,0-mal niedriger war als die der lokalen Sende- und Empfangsspulen, konnte diese Einschränkung durch die vier- bzw. acht-fach höhere verfügbare Gesamtleistung kompensiert werden. Während die leistungsfähigste lokale Sende- und Empfangsspule höhere Beschleunigungsfaktoren ermöglichte, erreichte die dedizierte lokale Empfangsspule das höchste Signal-Rausch-Verhältnis in der Phantommitte.

Zweitens wurden die pTx-Fähigkeiten der Remote-Spule durch *In-vivo*-Messungen untersucht. Die erste Studie zeigte eine homogene Anregung der Leber mit statischem pTx. Die zweite *In-vivo*-Studie dehnte den Anregungsbereich auf den gesamten Bauchraum aus, wo zwei k_T-Punkt pTx Pulse für eine ausreichende Homogenität bei allen Probanden erforderlich waren.

Zusammenfassend stellt die Remote-Spule in Kombination mit einem dedizierten lokalen Empfangs-Array hinsichtlich der Sende- und Empfangsleistung sowie der pTx-Fähigkeiten den Stand der Technik für die Körperbildgebung bei 7 T dar. Diese Ergebnisse unterstreichen ihr Potenzial für die Bildgebung mit großem Anregungsfeld und ihrer Notwendigkeit für die Umsetzung der UHF-Körper-MRT in die klinische Routine.

Contents

1 Introduction

Magnetic resonance imaging (MRI) has become a crucial aspect of medical diagnostics, as it provides cross-sectional images and soft-tissue contrast of the human body, which gives information about different pathologies like cancer or multiple sclerosis, without the need of invasive procedures [1, 2, 3, 4]. Furthermore, in contrast to computed tomography, which is another promising medical imaging technique, it does not require the use of ionizing radiation for imaging. Pushing boundaries of MRI with field strengths of 7 T and above, ultra-high field (UHF)-MRI showed already promising results in brain imaging [5, 6]. There, the commercially available Nova 8 transmit (Tx) / 32 receive (Rx) head coil (Nova medical Inc., Wilmington, USA) has become the standard coil at 7 T using multiple transmit channels.

In recent years, UHF-MRI body imaging is gaining more interest, despite being more challenging than brain imaging [7, 8, 9]. One of the main challenges at UHF body MRI is the presence of the spatially varying transverse magnetic component of the radiofrequency (RF) field (B_1^+) generated by the individual transmit elements and thus, resulting signal voids in the body. Several strategies have been developed to address this issue, such as the application of dedicated coils [10], dielectric pads [11, 12], or adiabatic pulses [13]. However, until now, no equivalent standard multi-transmit coil exists for body imaging; instead, most sites have developed their own coils over the past decade or have acquired prototype coils, which vary in coil design and number of Rx channels [10]. A standardized body coil would be highly beneficial for 7 T sites without RF engineering capabilities, as it would give these new sites a quick access to getting started with UHF body imaging. Also, it would enable comparability between different sites and allow multi-center studies. Furthermore, to achieve a potential extension of the existing 7 T CE label/FDA clearance for multi-transmit brain imaging to whole-body imaging, a standardized coil for body imaging would be desirable.

Another effective approach to solve the problem of signal voids in the body, which has been successfully applied, is parallel transmit (pTx), either static pTx or dynamic pTx [14, 15]. PTx is used in combination with multi-transmit coils, consisting of several independent elements with different B_1^+ transmit profiles. In static pTx, the individual Tx channels are fed by a common RF pulse shape that is weighted by channel dependent amplitude and phase. Several UHF groups showed the application of static pTx in the

human body, i.e. the prostate [9, 16], kidneys [17, 18], spine [19, 20], breast [21], heart [22] and hip [23, 24], where either a homogeneous B_1^+ was achieved or a high transmit efficiency (constructive interference between the individual B_1^+ transmit profiles of the elements of the coil). However, when optimizing the 3D field for intermediate-sized organs like the heart or larger organs such as the liver, static pTx is generally less effective, and local B_1^+ field dropouts may still occur at 7 T [25, 26, 27]. One solution is the time-interleaved acquisition of modes (TIAMO) method [28], which acquires multiple identical scans using two or more optimized shims. Each shim has B_1^+ dropouts at different positions. By combining these scans, a single image with a more homogeneous image intensity is obtained. The successful application of TIAMO has already been demonstrated for the kidneys [17], liver [29], as well as for a large pelvic region [30] and the abdomen [31, 32].

Another approach to optimize the B_1^+ fields of larger organs or regions is dynamic pTx. This method provides additional degrees of freedom by utilizing time-dependent complex weights, which are optimized alongside the applied excitation trajectory. For slice-selective dynamic pTx, Spokes pulses are commonly used, whereas for 3D excitation volumes, k_T-point pulses or SPINS pulses have been implemented [33, 34, 35]. These techniques have enabled homogeneous excitations of large organs in the human body, e.g. of the heart [22, 36] and of the liver [25, 37, 38]. Nevertheless, static pTx without B_1^+ dropouts for intermediate or large size organs or even body regions would be advantageous. It does not require modifications of the sequence (i.e. the excitation pulse and additional gradients) and is generally less sensitive to ΔB_0. Moreover, it allows for shorter transmission times and potentially shorter repetition times.

So far, primarily local Tx body coil arrays have been used, positioned on top and underneath the body, in contrast to the commonly used single or dual-channel whole-body RF transmit coils found in clinical systems at lower field strengths, which are typically located behind the bore liner. One reason for this is the higher power efficiency of local transmit coils, which require less RF power. This is a significant advantage, as most pTx systems are equipped with 8 amplifiers, each limited to 1 or 2 kW. Another reason is that local Rx coil arrays need to be placed close to the body to achieve high signal-to-noise ratio (SNR) values, allowing transceiver elements to serve for both, Tx and Rx, thus eliminating the need for a separate Tx array. Due to both of these factors, local Tx arrays have been more cost-effective so far.

With the availability of newer, cost-effective amplifier modules, high power has become more accessible, shifting the focus from power efficiency to specific absorption rate (SAR) efficiency (B_1^+ per maximum 10 g-averaged local SAR). Thus, a 32-channel RF transmit system with a total power output of 64 kW, featuring a remote body coil array, was recently introduced [31]. In this context, simulation studies have demonstrated that remote arrays placed behind the scanner boreliner achieve similar SAR efficiency to local arrays for smaller excitation regions, while offering a broader coverage for larger excitation regions. Increased homogeneity for complete 2D transversal or large 2D coronal slices is achieved in simulations using dynamic Spokes pulses [39, 40].

Additionally, transceiver arrays are typically larger and heavier than receive-only arrays, which makes them occupy more space in the scanner's typical 60 cm diameter bore. The increased distance to the body also offers advantages, such as providing more space for the elements and accommodating a larger number of transmit channels. Another advantage of remote whole-body arrays is the ability to combine local X-nuclei transmit arrays with the remote whole-body ^{1}H coil array [41]. However, the larger distance to the body also comes with disadvantages. One is a lower power efficiency, and another one is a reduced SNR performance due to the increased distance of the elements compared to local transceiver coils. However, the remote coil array has the advantage of being usable in combination with dedicated local Rx arrays, which are solely optimized for Rx performance.

This work is therefore divided into two parts. In the first part, the Tx and Rx performance of seven different existing local ^{1}H pTx coils for UHF body MRI from German sites and the remote 32-Tx-channel coil array are quantitatively evaluated through phantom measurements. Additionally, the performance of the remote array in combination with a dedicated, vendor-provided local 32-channel Rx array is assessed. For Tx performance, the power efficiency and the excitation coverage in head-foot (hf)-direction are evaluated. For Rx performance the SNR maps and acceleration capabilities in the central transversal slice are analyzed for all coils. This comparison contextualizes the remote array relative to the local body coils. The experimental data show that the remote array offers significant advantage and, when combined with the dedicated local Rx array, represent the state-of-the-art.
Thus, in the second part, the pTx capabilities of the 32-channel remote coil array are ex-

perimentally investigated using *in-vivo* measurements. The first *in-vivo* study examines the application of static and 3D dynamic k_T-point pTx pulses for the whole liver using the 32-Tx-channel whole-body remote array. Additionally, the impact of different Tx channel counts (8, 16 and 20) on the pTx capabilities is analyzed. The second *in-vivo* study extends the investigation of the application of static and 3D dynamic k_T-point pTx pulses to a larger excitation region, covering the whole abdomen.
Parts of this thesis have already been presented at various conferences, and sections have been submitted for publication as a research article in a scientific journal. These are detailed in the appendix.

2 Theory

This chapter introduces the concepts of nuclear magnetic resonance (NMR) and MRI. Furthermore, the advantages and challenges of UHF-MRI are discussed.

2.1 Nuclear magnetic resonance

This section provides an overview of the basic concepts of NMR, drawing from standard literature such as [42, 43, 44].

2.1.1 Nuclear spin and magnetic moment

Atoms consist of electrons and nucleons, with nucleons inherently possessing a quantized angular momentum known as nuclear spin. This spin was experimentally verified for the nucleus by Rabi in 1938. Since this work examines the hydrogen atom (^{1}H), the following theory only considers the ^{1}H nucleus, which possesses a finite nuclear spin I, leading to a magnetic moment $\vec{\mu}$

$$\hat{\vec{\mu}} = \gamma \hat{\vec{I}}, \tag{2.1}$$

where γ is the gyromagnetic ratio of the nucleus and depends on the Landé-factor g, the nuclear magneton μ_K and the reduced Planck constant $\hbar$:

$$\gamma = g\frac{\mu_K}{\hbar} \qquad \text{with} \qquad \mu_K = \frac{e\hbar}{2m_p} \tag{2.2}$$

with the proton rest mass m_p. The gyromagnetic ratio for the ^{1}H nucleus is determined as [45]

$$\gamma = 2\pi \cdot 42.577\,\mathrm{MHzT}^{-1} \tag{2.3}$$

In quantum mechanical framework, the nuclear spin operator $\hat{I}$ fulfills the commutator relations. Since it can be represented as state vector $|I, m\rangle$, it also fulfills the eigenvalue

equations

$$\left[\hat{I}_l, \hat{I}_m\right] = i\hbar\epsilon_{lmn}\hat{I}_n, \tag{2.4}$$

$$\left[\hat{I}_z, \hat{\vec{I}}^2\right] = 0, \tag{2.5}$$

$$\tag{2.6}$$

$$\hat{\vec{I}}^2|I,m\rangle = \hbar^2 I(I+1)|I,m\rangle, \tag{2.7}$$

$$\hat{I}_z = m\hbar|I,m\rangle. \tag{2.8}$$

Here, I is the spin quantum number with $I = \frac{1}{2}$ and m the magnetic spin quantum number $m \in \left[-\frac{1}{2}, +\frac{1}{2}\right]$.

2.1.2 Zeeman effect

The interaction of the magnetic moment $\vec{\mu}$ with an external static magnetic field $\vec{B}_0 = (0, 0, B_0)$ is described by the Hamiltonian operator

$$\hat{H} = -\vec{\mu} \cdot \vec{B}_0 = -\gamma\hbar B_0 \hat{I}_z \tag{2.9}$$

Therefore, the eigenvalues of this Hamiltonian are only multiplies of $(\gamma\hbar B_0)$ corresponding to the eigenvalues of $\hat{I}_z$ (equation 2.8). For the ^{1}H atom, the two allowed energy states are

$$E_{+\frac{1}{2}} = -\frac{1}{2}\gamma\hbar B_0, \tag{2.10}$$

$$E_{-\frac{1}{2}} = +\frac{1}{2}\gamma\hbar B_0. \tag{2.11}$$

$$\tag{2.12}$$

This degeneracy of the energy eigenstates is known as the Zeeman effect (figure 1) and the energy difference between these two states is

$$\Delta E = \gamma\hbar B_0 \tag{2.13}$$

To induce transitions between the two states the energy has to be absorbed or emitted by a photon with the energy $\Delta E = \hbar\omega_L$. This leads to the Larmor frequency

$$\omega_L = \gamma B_0. \tag{2.14}$$

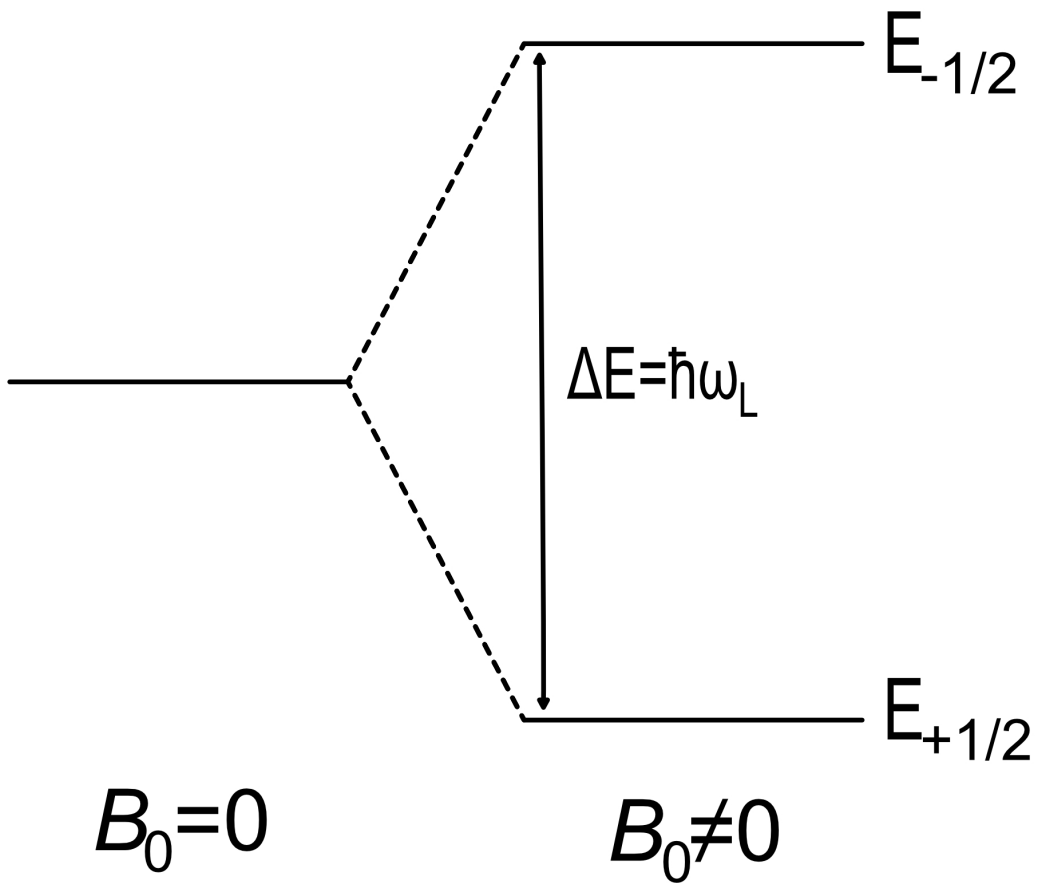

Figure 1: Splitting of the energy niveaus in a static magnetic field B_0. The Zeeman splitting results in 2 energy levels for the ^{1}H atom.

At a static magnetic field strength of 7 T this results in a Larmor frequency for the ^{1}H atom of $\omega_L \approx 298.04\,\mathrm{MHz}$.
Since ^{1}H atoms are fermions because they possess a spin of $\frac{1}{2}$, they follow the Fermi-Dirac statistics for their occupation numbers. At room temperature, where most of the *in-vivo* measurements are performed, the high temperature approximation can be applied for the Fermi-Dirac statistic. In this regime, the Fermi-Dirac distribution can be approximated by the Boltzmann distribution:

$$P\left(E_M\right) = \frac{e^{-E_m/k_B T}}{Z} \tag{2.15}$$

$$Z = \sum_m e^{-E_m/k_B T}, \tag{2.16}$$

with E_m the energy of each state as defined in equations 2.10 and 2.11, k_B the Boltzmann constant and T the temperature of the probe. The deviation between the energetically more favorable and the disfavorable state can be described by the polarization η, which is approximately

$$\eta \approx \frac{\gamma \hbar B_0}{2k_B T} \tag{2.17}$$

For a field strength of 7 T and a normal body temperature (≈293 K) a polarization of approximately 2.31×10^{-5} is achieved.

2.1.3 Macroscopic magnetization

In NMR imaging the signal derives from a macroscopic sample volume. In this context, instead of investigating individual spins, the macroscopic magnetization $\vec{M}$ of a spin ensemble is examined. This magnetization is expressed as the expectation value of the magnetic moments $\hat{\vec{\mu}}$ of N spins per volume V:

$$\vec{M} = \frac{1}{V} \sum_{i=1}^{N} \langle \hat{\vec{\mu}}_i \rangle = \sum_{i=1}^{N} \gamma \langle \hat{\vec{I}}_i \rangle \tag{2.18}$$

In thermal equilibrium ($t \to \infty$) only the z-component of the magnetization has a non-vanishing expectation value, resulting in a macroscopic magnetization ($\vec{M} = (0, 0, M_z)$ in z-direction:

$$M_z = \frac{N}{V} \frac{\gamma^2 \hbar^2 B_0}{4k_B T} \tag{2.19}$$

Thus, higher field strengths increase the measured signal. For ^{1}H imaging, M_z increases linearly with the static magnetic field B_0. Furthermore, the gyromagnetic ratio γ influences the measured signal quadratically, but protons possess the largest γ of all nuclei in the human body [46], making them ideal for imaging. Moreover, the proton density $\frac{N}{V}$ scales linearly, making a high proton density crucial for achieving higher signals.
In the following, this z-magnetization in thermal equilibrium will be denoted as M_0.

2.1.4 Equation of motion and Bloch equations

Since the spin ensemble is represented by a macroscopic sample volume, its behavior can be described using a semi-classical approach. In this framework, the equation of motion of the magnetization can be expressed using classical mechanics:

$$\frac{\partial \vec{M}(t)}{\partial t} = \gamma \vec{B}(t) \times \vec{M}(t) \tag{2.20}$$

If $\vec{M} \parallel \vec{B}_0$ the temporal deviations of $\vec{M}$ vanish. This leads to a finite transverse magnetization precessing around the static magnetic field $\vec{B}_0$ with the frequency γB_0. By introducing a rotating frame, denoted with $\prime$, which rotates with the angular velocity $\vec{\Omega}$ relative to the laboratory frame, equation 2.20 can be written as

$$\frac{\partial \vec{M}(t)}{\partial t} = \left(\frac{\partial \vec{M}(t)}{\partial t}\right)' + \vec{\Omega} \times \vec{M}(t) \tag{2.21}$$

$$\left(\frac{\partial \vec{M}(t)}{\partial t}\right)' = \gamma \vec{B}_{eff}(t) \times \vec{M}(t), \tag{2.22}$$

with $\vec{B}_{eff} = \vec{B}_0 - \frac{\vec{\Omega}}{\gamma}$. In the resonance case, where $\left|\vec{\Omega}\right| = \gamma \left|\vec{B}_0\right|$, $\left(\frac{\partial \vec{M}(t)}{\partial t}\right)'$ is zero and with that the magnetization is static in the rotating frame without any further field. However, this description neglects the interaction between spins and their environment. These interactions cause the magnetization to realign itself in equilibrium, returning to being parallel to the magnetic field B_0. This process is described by spin-lattice relaxation, characterized by the relaxation time T_1, which describes the decay of the transverse magnetization. The spin-spin relaxation time T_2 describes the dipole-dipole interactions between neighboring nuclei,leading to a loss of phase coherence in the transversal plane of the spin ensemble. To account for these relaxation processes, Bloch derived the Bloch equations, which are based on empirical observations. These equations describe the temporal evolution of the magnetization, incorporating both the spin-lattice and spin-spin relaxation processes:

$$\frac{\mathrm{d}M_x(t)}{\mathrm{d}t} = \gamma \left(\vec{M} \times \vec{B}\right)_x - \frac{M_x(t)}{T_2} \tag{2.23}$$

$$\frac{\mathrm{d}M_y(t)}{\mathrm{d}t} = \gamma \left(\vec{M} \times \vec{B}\right)_y - \frac{M_y(t)}{T_2} \tag{2.24}$$

$$\frac{\mathrm{d}M_z(t)}{\mathrm{d}t} = \gamma \left(\vec{M} \times \vec{B}\right)_z - \frac{M_z(t) - M_0}{T_1} \tag{2.25}$$

Defining the transverse and longitudinal compontents of the magnetization as

$$M_\perp = M_x + iM_y, M_\parallel = M_z, \tag{2.26}$$

the solution of the Bloch equations in the rotating frame and in the absence of an RF

field are

$$M_{\perp}(t) = M_{\perp}(0)e^{-t/T_2}, \tag{2.27}$$

$$M_{\parallel} = M_0 - \left(M_0 - M_{\parallel}(0)\right) e^{-t/T_1}. \tag{2.28}$$

In reality, besides the dipole-dipole interactions that cause dephasing of the spin ensemble, local inhomogeneities in the magnetic field also contribute to additional dephasing. This additional dephasing of the transverse magnetization results in a faster decay of the transverse magnetization and is described by the decay parameter $T_2^{\star}$, which is shorter than T_2.

2.1.5 RF excitation and NMR signal

To generate a NMR signal a time-varying RF field $\vec{B}_1(t)$ is applied, which is perpendicular to the static magnetic field $\vec{B}_0$:

$$\vec{B}_1(t) = \begin{pmatrix} B_1 \cos(w_{RF}t) \\ B_1 \sin(w_{RF}t) \\ 0 \end{pmatrix} \tag{2.29}$$

This leads to a magnetic field $\vec{B}(t) = \vec{B}_0 + \vec{B}_1(t)$ acting on the magnetization $\vec{M}$. If the duration of the applied RF field is short enough, relaxation effects can be neglected, meaning that the magnetization does not have enough time to relax significantly during the application of the RF field. In this case, the effects of the longitudinal and transverse relaxation are ignored and the Bloch equation (2.23), (2.24) and (2.25) are reduced to (2.20). Therefore, equation (2.20) transforms to

$$\frac{\partial \vec{M}(t)}{\partial t} = \gamma \vec{M} \times \begin{pmatrix} B_1 \cos(w_{RF}t) \\ B_1 \sin(w_{RF}t) \\ B_0 \end{pmatrix} \tag{2.30}$$

In the rotating frame equation (2.30) simplifies to equation (2.22) with $\vec{B_{eff}}$ in this case defined as:

$$\vec{B_{eff}} = \begin{pmatrix} B_1 \\ 0 \\ B_0 - \frac{w_{HF}}{\gamma} \end{pmatrix} \tag{2.31}$$

Thus, the magnetization rotates around the effective magnetic field $\vec{B}_{eff}$ with the direction and strength depending on the properties of the RF field. If the $\vec{B}_1$ field corresponds to the Larmor frequency of the ^{1}H atom the z'-component of $\vec{B_{eff}}$ vanishes and a stationary field in the rotating frame remains $\vec{B}_1 = (B_1, 0, 0)^\intercal$. The angle which the macroscopic magnetization is rotated around $\vec{B}_1$ is called the flip angle (FA) α and is defined as

$$\alpha = \int_0^{t_{RF}} \gamma B_1(t)\,\mathrm{d}t, \tag{2.32}$$

with t_{RF} the time of the RF field.
This RF pulse induces a signal in a nearby RF coil which is the free induction decay (FID) signal of NMR experiment depending on the relaxation time $T_2^\star$ and given by $S(t) \propto e^{-t/T_2^\star}$.

2.2 Magnetic resonance imaging

The basics of MRI will be described in this section. A more detailed introduction can be found in standard literature such as [43, 46, 47]. To be able to achieve a spatial resolution or excite only a certain slice additional linear gradient fields are applied, which are superimposed to the static magnetic field B_0. As the z-direction is defined as the direction of the static magnetic field B_0, the gradient fields can be defined as

$$\vec{G}_x = (0, 0, G_x \cdot x)^\intercal \tag{2.33}$$

$$\vec{G}_y = (0, 0, G_y \cdot y)^\intercal \tag{2.34}$$

$$\vec{G}_z = (0, 0, G_z \cdot z)^\intercal \tag{2.35}$$

$$\tag{2.36}$$

2.2.1 RF excitation

Similar to NMR, the magnetization is excited with a transmit coil. MRI employs two main types of excitation patterns, which depend on whether a 3D volume is excited non-selectively or a 2D slice or a 3D slab is excited selectively. These methods are described in the following in more detail.

2.2.1.1 Non-selective excitation

For a 3D volume a rectangular (rect) pulse with the duration t_{HF} is used. From equation (2.32) follows with a constant amplitude B_1 of the RF field

$$\alpha = \gamma B_1 t_{RF}, \tag{2.37}$$

where the frequency of the RF field matches the Larmor frequency of the static B_0 field. Since the whole volume contributes to the signal in non-selective excitation, the signal of the entire volume also needs to be acquired for artifact free images.

2.2.1.2 Selective excitation

In selective excitation the magnetization of a certain slice or slab is excited by applying an additional gradient field G_z. This changes the Larmor frequency of the spin ensemble in z-direction:

$$\omega(z) = \gamma(B_0 + G_z \cdot z) \tag{2.38}$$

Therefore, the center of the slice can be adjusted using G_z, while the slice thickness is determined by the bandwidth (BW) of the pulse.

$$\Delta z = \frac{\Delta\omega}{\gamma G_z}, \tag{2.39}$$

with the excited frequency band $\Delta\omega$ Furthermore, the slice position z_1 can be modified by a different frequency w_1 of the excitation pulse, which needs to match the Larmor frequency of the spin ensemble at position z_1 (figure 2).

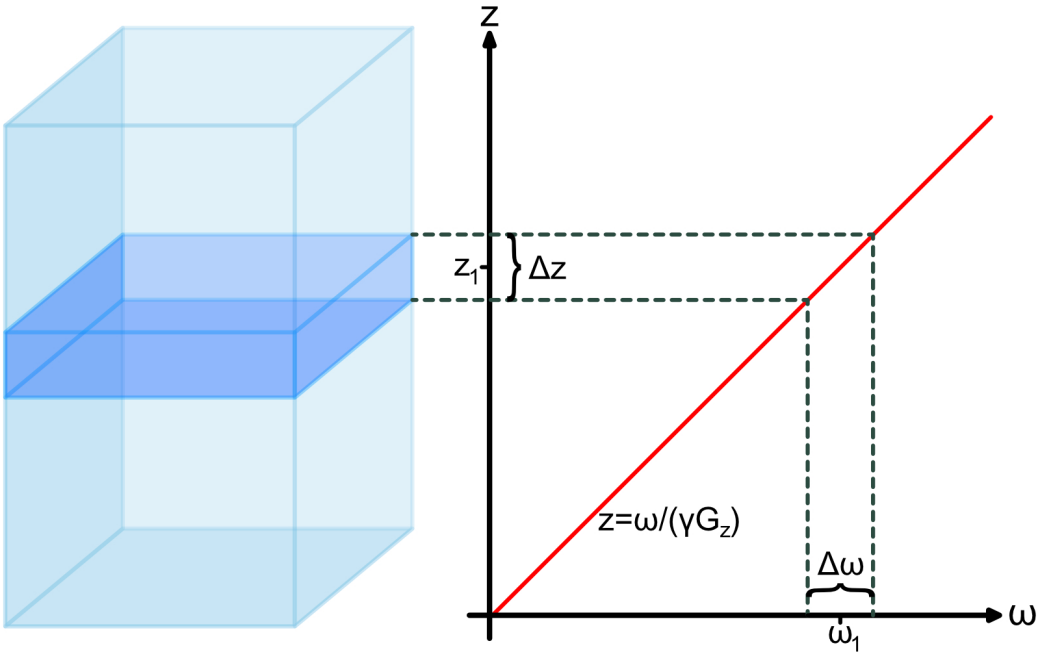

Figure 2: Excitation of a slice with a center z_1 and a width of Δz. This is achieved by applying a gradient G_z in z-direction and an RF pulse with a center frequency ω_1 and a bandwidth of $\Delta\omega$.

2.2.2 Spatial encoding

In order to spatially encode the measurement signal after excitation, gradient fields need to be applied during signal acquisition in two directions for 2D data acquisition (readout and phase encoding) or in all three directions (readout (RO), phase encoding (PE) and slab selection) for 3D acquisition. By applying a temporally constant gradient

$\vec{G}$ for a duration t the resulting Larmor frequency of the spin ensemble is then spatially dependent. For a given position vector $\vec{r}$ this results in

$$\omega(\vec{r}, t) = \gamma \left(B_0 + \vec{G}(t) \cdot \vec{r} \right). \tag{2.40}$$

In the following a non-interacting transverse magnetization is assumed in the rotating frame. After the application of the gradient the phase accumulation is described as

$$\phi(\vec{r}, t) = -\int_0^t \omega(\vec{r}, t')\,\mathrm{d}t' = -\gamma\vec{r}\int_0^t \vec{G}(t')\,\mathrm{d}t' = -2\pi\vec{r}\vec{k}(t), \tag{2.41}$$

with $\vec{k}$ the spatial frequency which spans the k-space

$$\vec{k}(t) = \frac{\gamma}{2\pi}\int_0^t \vec{G}(t')\,\mathrm{d}t', \tag{2.42}$$

The integral of the spatial magnetization distribution $M_\perp$ in a volume V gives the measurement signal

$$S(\vec{k}) \propto \int_V M_\perp(\vec{r}) e^{-i2\pi\vec{k}(t)\vec{r}}\,\mathrm{d}\vec{r} \tag{2.43}$$

If the measurement signal $M_\perp$ is known for all $\vec{k}$ the spatial magnetization distribution can be calculated via the inverse Fourier transform of equation (2.43)

$$M_\perp(\vec{r}) \propto \int_V S(\vec{k}) e^{i2\pi\vec{k}(t)\vec{r}}\,\mathrm{d}\vec{k}. \tag{2.44}$$

For frequency encoding a gradient is applied during data acquisition, which leads to a change of $\vec{k}$ because the time t is changed. For phase encoding a gradient is applied before signal acquisition, which also leads to a change of $\vec{k}$ because the gradient $\vec{G}$ is changed. However, to allow a constant t, N acquisitions need to be repeated to acquire N data points.

2.2.3 Discrete k-space sampling

In reality, only a discrete sampling of $\vec{k}$ will be acquired, where the Fourier transform is replaced by the fast Fourier transform (FFT) published by Cooley and Tukey in 1965 [48]. To fill the k-space discretely, the basic method is a cartesian readout. In general, the RO and PE direction can be chosen arbitrarily; for the purpose of simplicity, the RO is set here in the k_x-direction, which is acquired with frequency encoding and the PE-

direction in the k_y-direction and acquired with phase encoding. With that, after every RF pulse one k_x-line with N_x points is acquired (figure 3). For 3D, the slab selection direction is sampled with an additional phase encoding.
Several other sampling trajectories exist, like radial sampling (2D and 3D) or radial phase-encoding (RPE) (3D). The advantage of these methods are motion-robustness as well as the possibility to acquire in free-breathing, as a cartesian readout suffers from artifacts when motion is present. Their trajectories are also shown in figure 3.

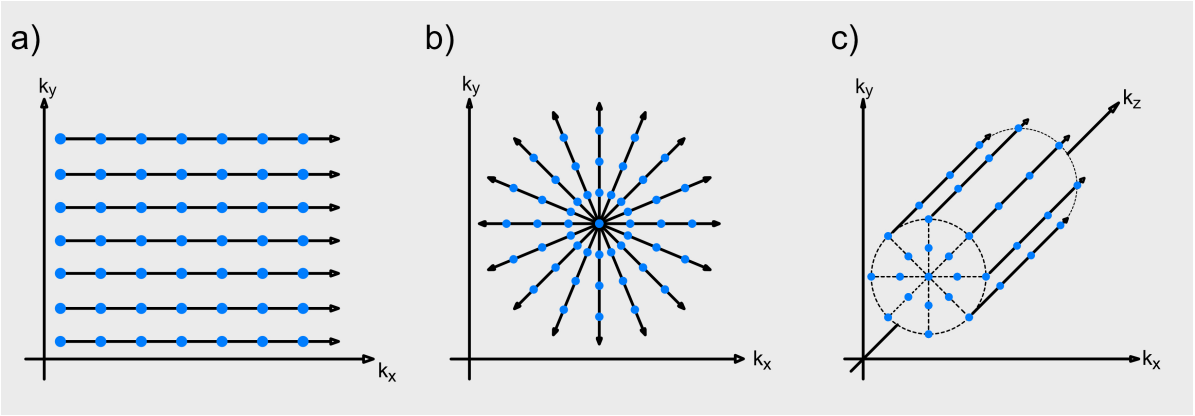

Figure 3: Schematic drawing of a discrete k-space sampling for a) 2D cartesian readout, b) 2D radial readout and c) 3D RPE readout.

To acquire an artifact free image with a cartesian readout the Nyquist criterion needs to be fulfilled, which states that the nominal spacial resolution Δx depends on the maximal value of k defined as k_{max} and the field of view (FoV) in image space on the distance between the sampling points in k-space Δk

$$\Delta x = \frac{1}{2k_{max}}, \tag{2.45}$$

$$FoV_i = \frac{1}{\Delta k_i}, \tag{2.46}$$

along direction $i = x, y, z$.

2.2.4 Excitation k-space for small tip angle excitation

Similar to the previously described acquisition k-space, the excitation k-space can be used for description of the excitation of the magnetization [49]. The Bloch equations

(2.23) (2.24) (2.25) in the rotating frame, neglecting T_1 and T_2 can be written as

$$\begin{pmatrix} \frac{\partial M_x}{\partial t} \\ \frac{\partial M_y}{\partial t} \\ \frac{\partial M_z}{\partial t} \end{pmatrix} = \gamma \begin{pmatrix} 0 & \vec{G}(t) \cdot \vec{r} & -B_{1,y}(t) \\ -\vec{G} \cdot \vec{r} & 0 & B_{1,x}(t) \\ B_{1,y}(t) & -B_{1,x}(t) & 0 \end{pmatrix} \begin{pmatrix} M_x \\ M_y \\ M_z \end{pmatrix}, \tag{2.47}$$

with $\vec{G}(t)$ the applied gradient and B_1 the RF fields in x and y-direction, both functions of time. The small tip angle approximation [50, 51] assumes that the longitudinal magnetization is approximately equal to its equilibrium value

$$M_z \approx M_0, \tag{2.48}$$

if the magnetization $\vec{M}$ is rotated only by a small FA. Defining the applied RF field as

$$B_1^+ = B_{1,x} + iB_{1,y}, \tag{2.49}$$

and using $M_\perp$ (c.f. equation (2.26)), the first two components of equation (2.47) can be written as the single complex different equation

$$\frac{\partial M_\perp}{\partial t} = -i\gamma \vec{G}(t) \cdot \vec{r} M_\perp + i\gamma B_1^+ M_0. \tag{2.50}$$

If the system was initially in thermal equilibrium ($\vec{M} = (0, 0, M_0)^\intercal$, it can be solved at time T to determine the magnetization

$$M_\perp(\vec{r}) = i\gamma M_0 \int_0^T B_1^+(t) e^{-i\gamma \vec{r} \cdot \int_t^T \vec{G}(t')\,\mathrm{d}t'}\,\mathrm{d}t. \tag{2.51}$$

Here, the transverse magnetization is gives as a function of the applied RF fields as well as the gradient fields, which can be both time-varying. Also, the integration of the RF pulse is from time t to the time of the end of the RF pulse T.
Introducing a spatial frequency variable $\vec{k}_{exc}(t)$, which spans the excitation k-space and is defined as

$$\vec{k}_{exc}(t) = -\frac{\gamma}{2\pi} \int_t^T \vec{G}(t')\,\mathrm{d}t', \tag{2.52}$$

equation (2.51) can be rewritten as

$$M_\perp(\vec{r}) = i\gamma M_0 \int_0^T B_1^+(t) e^{i2\pi \vec{r} \cdot \vec{k}_{exc}(t)}\,\mathrm{d}t. \tag{2.53}$$

Note that the function $\vec{k}_{exc}(t)$ parametrically represents a trajectory through the spatial frequency space. The exponential factor can be rewritten to

$$M_{\perp}(\vec{r}) = i\gamma M_0 \int_0^T B_1^+(t) \int_K \delta^3(\vec{k}_{exc}(t) - \vec{k}_{exc}) e^{i2\pi\vec{r}\cdot\vec{k}_{exc}(t)} \,\mathrm{d}\vec{k}_{exc} \,\mathrm{d}t, \tag{2.54}$$

using the integral of a three-dimensional Dirac delta function δ^3. Interchanging the order of the integration leads to

$$M_{\perp}(\vec{r}) = i\gamma M_0 \int_K \left\{ \int_0^T B_1^+(t)\delta^3(\vec{k}_{exc}(t) - \vec{k}_{exc}) \,\mathrm{d}t \right\} e^{i2\pi\vec{r}\cdot\vec{k}_{exc}(t)} \,\mathrm{d}\vec{k}_{exc}. \tag{2.55}$$

The inner integral over time represents the three-dimensional trajectory weighted by B_1^+ and is defined as

$$\rho(\vec{k}_{exc}) = \int_0^T B_1^+(t)\delta^3\left(\vec{k}_{exc}(t) - \vec{k}_{exc}\right) \mathrm{d}t. \tag{2.56}$$

Normalizing the delta function using the relation $\frac{\partial\vec{k}_{exc}(t)}{\partial t} = \gamma\vec{G}(t)$ results in

$$\rho(\vec{k}_{exc}) = \int_0^T \frac{B_1^+(t)}{|\gamma\vec{G}(t)|} \left\{ \delta^3\left(\vec{k}_{exc}(t) - \vec{k}_{exc}\right) \left| \frac{\partial\vec{k}_{exc}(t)}{\partial t} \right| \right\} \mathrm{d}t. \tag{2.57}$$

Again, similar to spatial encoding, the resulting transverse magnetization is a Fourier transform of the weighted k-space trajectory

$$M_{\perp}(\vec{r}) = i\gamma M_0 \int_K \rho(\vec{k}_{exc}) e^{i2\pi\vec{r}\cdot\vec{k}_{exc}} \,\mathrm{d}\vec{k}_{exc}. \tag{2.58}$$

2.2.5 Signal-to-noise ratio

A receive coil, which can either be the same as the transmission coil or a dedicated receive coil, is used to detect the NMR signal. As the signal is inherently weak, noise induced into the signal reduces the quality of the resulting image. There are three primary sources of noise in MRI [7, 52, 53]. First, the resistance of the coil; second, dielectric and inductive losses in the sample; and third, electronic noise, such as that from the preamplifier. To asses image quality the acSNR can be determined.
For an MRI image acquired without additional filters, the SNR can be estimated using the signal intensities. Therefore, the mean pixel magnitudes $mean_{signal}$ of a certain region of interest (ROI) are devided by the standard deviation σ of the magnitudes

σ_{noise} in a ROI placed outside of the phantom in the noise. Since the noise distribution follows a RICIAN distribution at small SNR values and only approximates a GAUSSIAN distribution at higher SNR values [54], σ has to be corrected by a factor of 0.66 [55]. Using this correction, the SNR can be calculated as follows:

$$SNR = \frac{mean_{signal}}{\frac{\sigma_{noise}}{0.66}} \tag{2.59}$$

2.2.6 Parallel imaging

Parallel imaging can be employed to reduce the acquisition time. This technique requires specialized hardware, namely phased arrays, which consist of multiple independent receiver channels [56]. These phased arrays are standard in nearly all modern clinical MRI scanners. Each array element has a spatial sensitivity profile $S_i^-(\vec{r})$, with the highest sensitivity to the magnetization in its close surroundings, which decreases with increasing distance. Following equation (2.43), the signal of the i-th receive element can be described as

$$S_i(\vec{k}) = \int_V S_i^-(\vec{r}) M_\perp(\vec{r}) e^{-i2\pi\vec{k}(t)\vec{r}}\,\mathrm{d}\vec{r} \tag{2.60}$$

In parallel imaging, the k-space can be undersampled by skipping phase encoding lines at regular intervals during acquisition. This increases the spacing between adjacent k-space lines, effectively reducing the FoV. As a result, object replicas appear at regular intervals in the reduced FoV image, with the number of duplicates corresponding to the acceleration factor. This artifact, known as aliasing, is illustrated in figure 4. With phased arrays, k-space can be undersampled while still enabling the reconstruction of an artifact-free image.

The degree to which an acquisition can be undersampled depends on the array's capabilities. The undersampling factor, also referred to as the acceleration factor R, is a key parameter in this context.The degree to which an acquisition can be undersampled is dependent on the array.

Parallel imaging techniques are classified into two categories based on how the missing phase encoding lines are reconstructed. In the first approach, the missing lines are reconstructed in k-space, with the most commonly used method being generalized autocalibrating partially parallel acquisitions (GRAPPA) [58]. In the second approach, the aliased pixels are separated in image space, as in the case of sensitivity encoding (SENSE) [59].

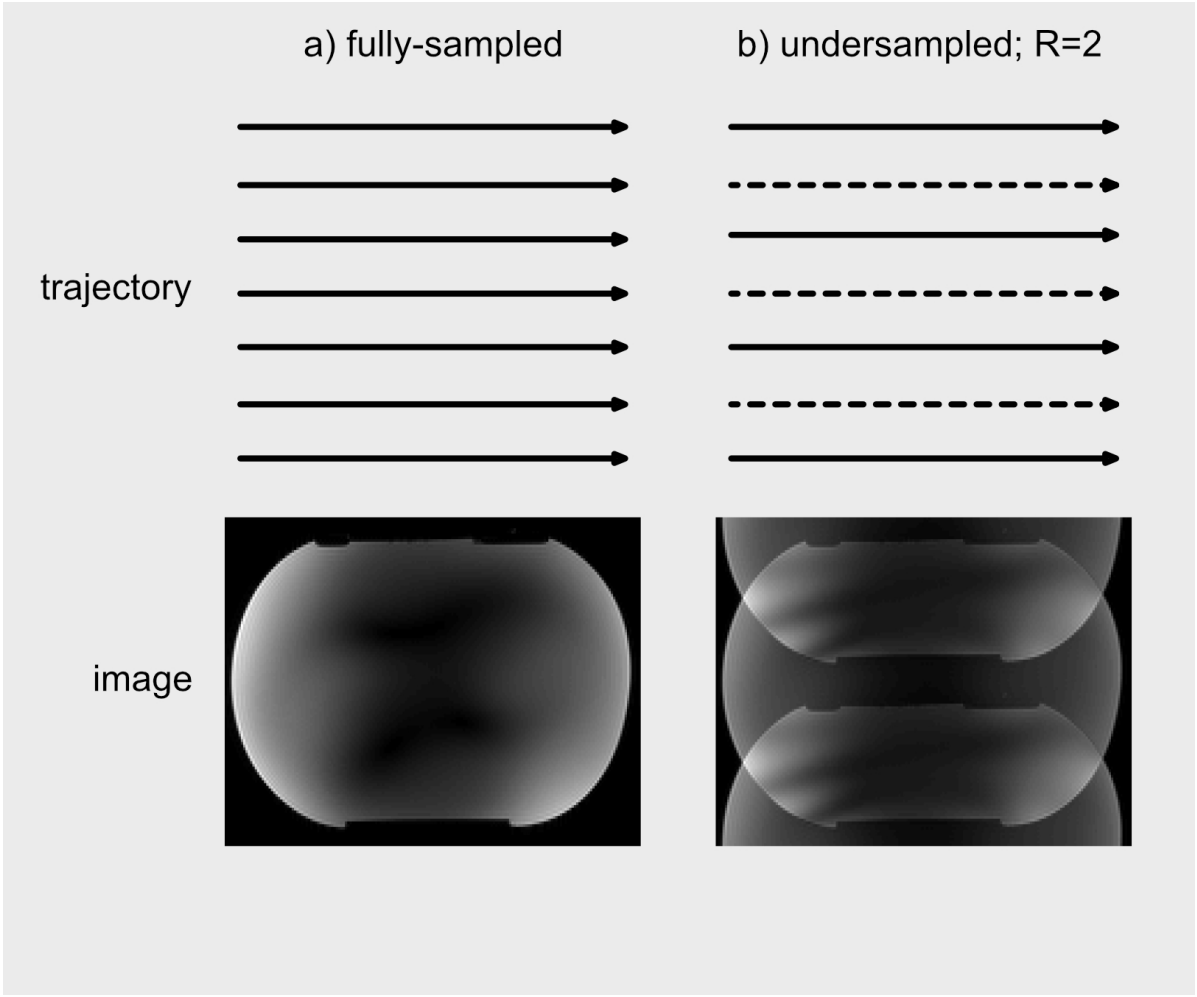

Figure 4: Image acquired with cartesian readout and a) fully sampled k-space, b) undersampled k-space with an acceleration factor of R=2 [57].

2.2.7 RF exposure in MRI

As described in section 2.1.5, RF pulses are employed to generate a NMR signal. Consequently, oscillating electric fields are produced during imaging, leading to energy deposition in tissue.

Even a slight increase in tissue temperature by just a few degrees can cause tissue damage in the human body. This extent of this temperature increase is influenced by the body's thermoregulation abilities, which can vary based on factors such as the overall health of the individual. Therefore, the International Electrotechnical Commission (IEC) has established safety guidelines for the *in-vivo* use of MRI device. These guidelines specify the maximum allowable temperature limits for RF exposure, ensuring that the subject

is not at risk of harm during the procedure (table 1) [60].

Table 1: Temperature limits and temperature elevation limits given by the IEC for a save use of the MRI device [60]. The normal mode is used for most clinical MRI examinations and considered safe for the majority of patients. During the first level mode the RF exposure may cause physiological stress. It is therefore necessary to have active medical supervision. No specific limits are given for the 2nd level controlled mode. This mode may only be used with an approval of the ethics review committee.

Operating Mode	Maximal body core temperature in $°C$	Maximal body core temperature elevation in $°C$
Normal	38	0.7
1st Level	38.5	1.3
2nd Level	>38.5	>1.3

However, to this date, it is not possible to directly measure tissue temperature through *in-vivo* MRI examinations except through invasive methods. Consequently, the tissue temperature is not directly monitored during MRI measurements. Instead, the SAR, which describes the absorbed power per unit mass, is continuously monitored during an MRI scan to ensure patient safety. The limits for SAR are set by the IEC and outlined in table 2. The SAR is calculated using the following equation:

$$SAR(\vec{r}) = \frac{1}{2V} \int_V \frac{\sigma_c(\vec{r})}{\rho_m(\vec{r})} \left| \vec{E}(\vec{r}) \right|^2 \mathrm{d}V, \tag{2.61}$$

with V the volume, σ_c the electrical conductivity and ρ_m the mass density. The measurement is aborted to ensure patient safety, if the 10 s or 6 min limit is exceeded.
As

$$\left| \vec{E}(\vec{r}) \right|^2 \propto \left| \vec{B_1^+}(\vec{r}) \right|^2 \propto \alpha^2, \tag{2.62}$$

doubling the FA for the same pulse duration and RF pulse shape will cause a fourfold increase in SAR.

Table 2: SAR limits given by the IEC for a save use of the MRI device [60]. They are given as SAR limits for larger body regions (whole body, partial body or head) and local SAR limits depending on the array type. Furthermore, they are separated into normal and 1st and 2nd level controlled mode. The SAR limits apply to a time averaging over 6 min.

Operating Mode	Volume Transmit Coils			Local Transmit Coils		
	Whole body	Partial body	Head	Head	Trunk	Extremities
Normal	2	2-10	3.2	10	10	20
1st Level	4	4-10	3.2	20	20	40
2nd Level	>4	> 4-10	>3.2	>20	>20	>40

2.3 Ultra-high field MRI

MRI systems used in clinical routine typically operate at field strengths of 1.5 T or 3 T. In 2017, the new 7 T MRI system from Siemens Healthineers (Erlangen, Germany) received clinical approval from the U.S. Food and Drug Administration (FDA). Experimental devices operating at field strengths of 9.4 T, 10.5 T, and 11.7 T have been developed and are currently used for research purposes. A 14 T system is currently under development pushing the field strengths even higher. When referring to UHF-MRI, field strengths of 7 T and higher are meant [7]. The following section explains the advantages, challenges and solutions associated with these field strengths.

2.3.1 Advantages

The main advantage of UHF-MRI is the increase of the NMR signal as it is directly proportional to the static magnetic field (c.f. equation (2.19)). The SNR improves with increasing field strength, as the measurement noise is dominated by the sample-noise in most *in-vivo* measurements [7]. However, recent simulative work showed, that the SNR is not increasing linearly with B_0 as for lower field strengths but with a power factor B_0^x with $x \approx 2.1$ in the center of the head and with $x \approx 1.2$ near the surface [61]. Recent experimental studies have observed an increase in SNR by a factor of $x \approx 1.65$ over the whole brain when comparing 3 T, 7 T and 9.4 T in the head [62]. For the center of a spherical phantom, a SNR increase by a factor of $x \approx 1.94$ was found when comparing 3 T, 7 T, 9.4 T and 11.7 T [63].
With an approximately 4-fold higher average SNR at 7 T compared to 3 T, it becomes possible to enhance spatial or temporal resolution [5, 64] or to reduce acquisition time.

A more clinically relevant parameter is often the contrast-to-noise ratio (CNR), which measures the contrast between the tissue of interest (S_2) and the surrounding tissue (S_1). It is defined as:

$$CNR = \frac{S_2 - S_1}{\sigma_{noise}}, \tag{2.63}$$

with σ_{noise} the standard deviation noise of the image. The CNR increases for susceptibility weighted imaging (SWI), blood-oxygen-level-dependent (BOLD) imaging and functional magnetic resonance imaging (fMRI) with increasing field strength [65].
With the increase of the T_1 relaxation time magnetic resonance angiography (MRA) at 7 T has an advantage over MRA at 3 T due to an improved background suppression [65]. Furthermore, both magnetic resonance spectroscopy (MRS) and chemical exchange saturation transfer (CEST) imaging benefit from higher field strengths. In addition to the increased SNR, the chemical shift also scales with field strength, leading to higher spectral resolution. This allows for better separation of metabolite peaks and improved detection of different molecular compounds [7, 66].

2.3.2 Challenges

2.3.2.1 Static magnetic field

With modern *in-vivo* MRI systems a static magnetic field B_0 homogeneity of approximately 1 ppm (parts per million) over the FoV can be achieved in the absence of a phantom or a subject.[67] This corresponds to a variation of the Larmor frequency $\Delta\omega_L$ of approximately 64 Hz at 1.5 T and approximately 298 Hz at 7 T. To account for the larger variations, more precise MRI hardware is required for higher field strengths. Additionally, when a phantom or subject is inserted into the scanner, variation in tissue properties cause local B_0 changes, i.e. the magnetic susceptibility difference between air and tissue is approximately 10 ppm, which significantly disturb the B_0 homogeneity around air–tissue interfaces [68]. Modern MRI scanner come with first, second and partial third order shim coils to correct for ΔB_0 inhomogeneities. However, they are not able to correct all of these inhomogeneities [69]. These B_0 inhomogeneities cause an additional phase accumulation of the transverse magnetization and can be included into equation (2.53). The transverse magnetization is then given as [70, 71]

$$M_\perp(\vec{r}) = i\gamma M_0 \int_0^T B_1^+(t) e^{i\gamma \Delta B_0(\vec{r})(t-T)} e^{i2\pi \vec{r}\cdot\vec{k}(t)} \,\mathrm{d}t. \tag{2.64}$$

2.3.2.2 RF field

Following equation (2.14) increasing the static magnetic field B_0 leads to an increase of the Larmor frequency and consequently a reduction of the wavelength λ. Figure 5 shows the different wavelengths of the RF field at different static magnetic field strength's B_0. The RF wavelength at 7 T becomes similar to the size of the human head and smaller

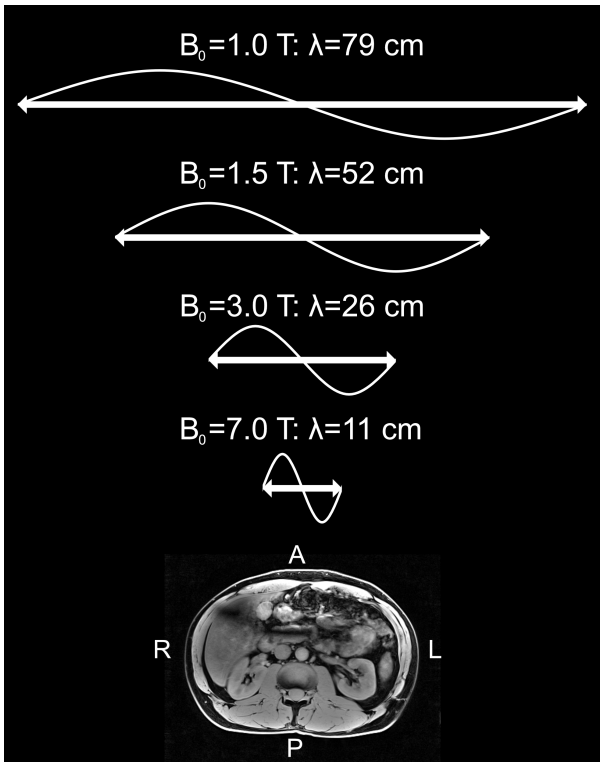

Figure 5: RF wavelength in tissue for different field strengths. For size comparison a *in-vivo* transversal MRI image is shown on the bottom.

than the human body [7]. With that, spatial variations of the $B_1^+(\vec{r},t)$ field lead to FA variations or even dropouts, which influence the signal intensity and the contrast of the acquired image. Furthermore, this leads to spatial variations of the E field. This heterogeneous E field can result in locally varying SAR. At 7 T all Tx coils and arrays are limited by the local SAR limits given in table 2.

2.3.3 Parallel transmit

Several methods have been developed to address these aforementioned RF inhomogeneities, like the use of dedicated coils [10] and dielectric pads [11, 12]. Another possibility, which has been successfully applied is pTx. Similar to parallel imaging, multiple

independent channels i are needed for transmission, which have a spatially varying sensitivity profile $S_i^+(\vec{r})$ also called transmit sensitivity (figure 6). Consequently, the spatial and temporal components of $B_1^+(\vec{r},t)$ can be separated [72]:

$$B_{1,i}^+(\vec{r},t) = p_i(t)S_i^+(\vec{r}), \tag{2.65}$$

with $p_i(t)$ the RF pulse played through the i-th channel.

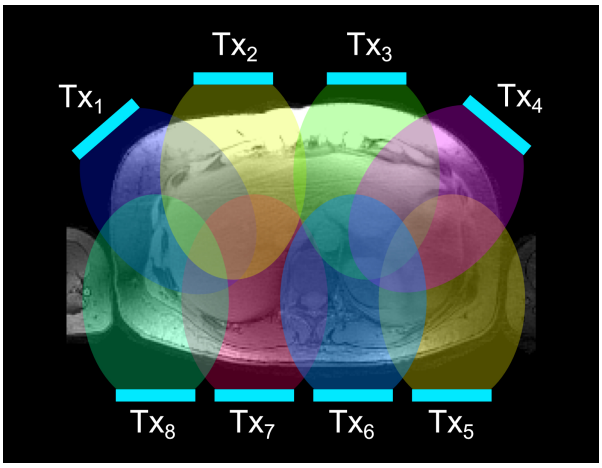

Figure 6: Example transmit sensitivity maps for 8 Tx channels.

The transverse magnetization $M_{i,\perp}$ (c.f. equation (2.64)) for one element can be written as:

$$M_{i,\perp}(\vec{r}) = i\gamma M_0 S_i^+(\vec{r}) \int_0^T p_i(t) e^{\gamma \Delta B_0(\vec{r})(t-T)} e^{i2\pi\vec{r}\cdot\vec{k}_{exc}(t)}\,\mathrm{d}t, \tag{2.66}$$

In the small tip angle regime, the magnetization of each individual element can be superimposed. Consequently, the total magnetization of an array consisting of N elements is:

$$M_\perp(\vec{r}) = i\gamma M_0 \sum_{i=1}^{N} S_i^+(\vec{r}) \int_0^T p_i(t) e^{\gamma \Delta B_0(\vec{r})(t-T)} e^{i2\pi\vec{r}\cdot\vec{k}_{exc}(t)}\,\mathrm{d}t \tag{2.67}$$

An iterative pulse design method, called the spatial domain method, can be achieved by discretizing time to N_t samples and space to N_s samples. With that, equation (2.67) can be written as [73]

$$\vec{M} = A_{full}\vec{b}_{full}, \tag{2.68}$$

where $\vec{M}$ is the vector of spatial samples of the total excitation pattern with length N_s, the system matrix A_{full} containing the sensitivity pattern of the array elements, the excitation path in k-space and the static field inhomogeneity distribution with size

$N_s \times N_t$ and $\vec{b_{full}}$ the vector of RF pulse samples with length N_t. A RF pulse can be designed by solving a minimization problem, if a desired magnetization pattern $\vec{M_{des}}$ at the spatial locations $\vec{r_i}$ is given [36, 73]:

$$\hat{\vec{b}}_{full} = \arg\min_{\vec{b}_{full}} \left\{ \left\| A_{full}\vec{b}_{full} - \vec{M_{des}} \right\|_W^2 + R(\vec{b}_{full}) \right\}, \tag{2.69}$$

with W a diagonal matrix containing spatial error weighting to ignore regions outside of a ROI and a Tikhonov regularization term to control the integrated RF power defined as

$$R(\vec{b}_{full}) = \lambda ||\vec{b}_{full}||^2, \tag{2.70}$$

with λ a regularization parameter to trade-off between RF power and achieving the desired magnetization pattern. This minimization problem can be solved iteratively. Thus, using the spatial domain method, an arbitrary RF pulse shape - unique to each Tx channel - can be designed to generate the desired transverse magnetization.

2.3.3.1 Static pTx

In static pTx the same RF pulse shape $p(t)$ is applied to all Tx channels and weighted by a Tx-channel-dependent and time-independent amplitude and phase term $w_i = a_i e^{i\phi_i}$, where a_n is the amplitude and ϕ_n the channel dependent phase (figure 7a)) [7, 72]:

$$B_1^+(\vec{r}, t) = p(t) \sum_{i=1}^{N} w_i S_i^+(\vec{r}) \tag{2.71}$$

The superposition of the B_1^+ fields, and consequently the FA, is optimized within a target ROI by determining the shim weights for each channel. If both, magnitude and phases are variables during optimization the process is referred to as magnitude and phase shimming. On the other hand, if the magnitudes are fixed for all channels ($a_i = a$) and only the phases are varied, this is called phase shimming. The coefficient of variation (CV) can be maximized, which is inherently normalized by the mean value of $|A_{full}b_{full}|$ within the ROI, to quantify the spatial homogeneity of the excitation [36]. The CV is defined as

$$CV = \frac{std(|A_{full}b_{full}|)}{mean(|A_{full}b_{full}|)}, \tag{2.72}$$

and is calculated in the ROI.

2.3.3.2 Dynamic pTx - k_T-point pTx pulses

Static pTx is fundamentally limited by the degrees of freedom provided through the constructive and destructive superposition of the B_1^+ fields of a finite number of transmit channels with different weights [72]. In contrast, dynamic pTx allows the superposition of the B_1^+ fields to vary throughout a RF pulse on a very short timescale. The main goal of dynamic pTx is to ensure the desired FA pattern (i.e. homogeneous) within the ROI by the end of the RF pulse (figure 7 b)). Additionally, the RF transmission can occur at different excitation k-space locations by applying additional gradients (c.f. equation 2.52).

One type of dynamic pTx pulses are the so-called k_T-point pTx pulses [34]. These k_T-points provide spatially uniform excitation in an extended volume with tailored non-selective RF pulses. Hereby, the pulse shape remains identical across all Tx channels, but the weights are adjusted during the RF pulse. k_T-points pulses consists of a train of N rectangular subpulses with different weights and with gradients applied only in the intervals between these subpulses. As a result, RF power is only applied at distinct positions when stationary in excitation k-space, hence the name k_T-points. Both, the weighting of each individual subpulse and the gradients to travel to the excitation k-space locations are optimized to achieve a homogeneous FA distribution.

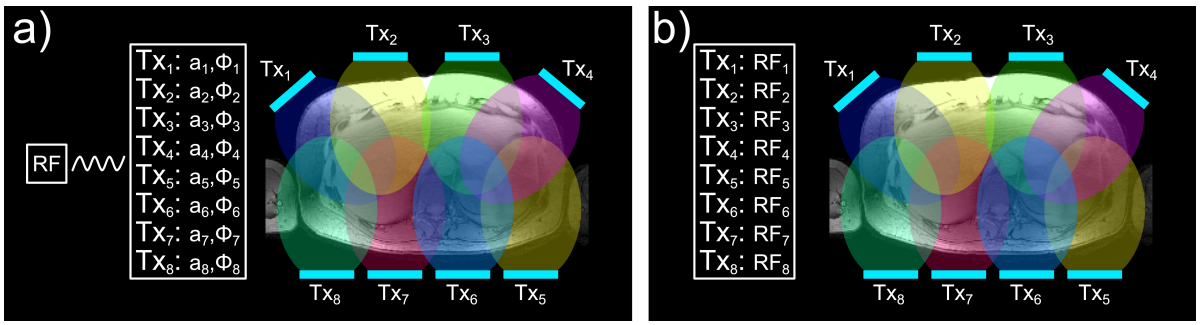

Figure 7: a) For static pTx all Tx channels share the same RF pulse shape. To optimize the FA distribution the magnitude a_i and phase ϕ_i of each channel i is modulated. b) On each transmit channel i an individual RF pulse is applied for dynamic pTx.

3 Methods

This chapter explains the experimental setups including the pTx systems, the used RF coils and the phantom used for the studies. Furthermore, the conducted measurements and the evaluation of the data are described.

3.1 Hardware

3.1.1 MRI scanner

All measurements were performed on a 7 T MRI system (MAGNETOM 7T, Siemens Healthcare, Erlangen, Germany), which is equipped with a AS095DS gradient coil. The gradient coil produces a maximal magnetic gradient amplitude of $38\,\mathrm{mT\,m^{-1}}$ achieving a maximal slewrate of $200\,\mathrm{mT\,m^{-1}\,ms^{-1}}$. The nominal FoV is 50 cm in all directions.

Figure 8: Photograph of the 7 T MRI system, located at the German Cancer Research Center (DKFZ) in Heidelberg, Germany.

3.1.2 pTx systems

3.1.2.1 Siemens pTx system

The Siemens pTx system "Step 2.3" enables 8 different Tx channels with 1 kW power per channel (figure 9). It can be driven in full pTx meaning that the RF pulse of each channel can be individually controlled and adapted.

Figure 9: Photograph of the Siemens pTx system "Step 2.3".

3.1.2.2 MRexcite pTx system

The MRexcite pTx system is an add-on pTx system that operates using the Siemens combined mode [31]. It includes a modulator system, power amplifiers and a SAR supervision unit (figure 10a)). The system utilizes four input signals from the Siemens combined mode for synchronization: the transmit or receive state, the unblank trigger bit for the Tx amplifiers, a trigger bit to set the modulators, and the RF signal from the exciter, which is split up and modulated on the modulators. The only modification to the vendor's Tx and Rx paths is the addition of additional RF switches. These switches allows toggling between transmission and reception with local coil arrays and a remote whole-body array. The MRexcite system enables full pTx with 32 channels, each

amplifier capable of delivering nominal 2 kW of power, resulting in a total RF power of 64 kW. Additionally it supports an RF pulse sampling rate of 100 kHz. The interface of the safety supervision is depicted in figure 10b). This system uses a per channel RF power constraint instead of a virtual observation point (VOP) based constraint, limiting the power per channel in the 10 s average to 6.6 W and in the 6 min average to 3.3 W. The rationale behind this constraint is that the implemented safety supervision takes only the forward RF power into account [74, 75]. A power-based safety supervision is technically easier to implement in terms of hardware and software for 32 channels than a SAR supervision based on VOP [76, 77], as only half of the data (only the magnitude and not the phase of the signal) is supervised, and the data can be further compressed by averaging of the magnitudes of each channel over a short time period. However, this approach is more conservative, permitting less RF power compared to a full phase-based supervision.

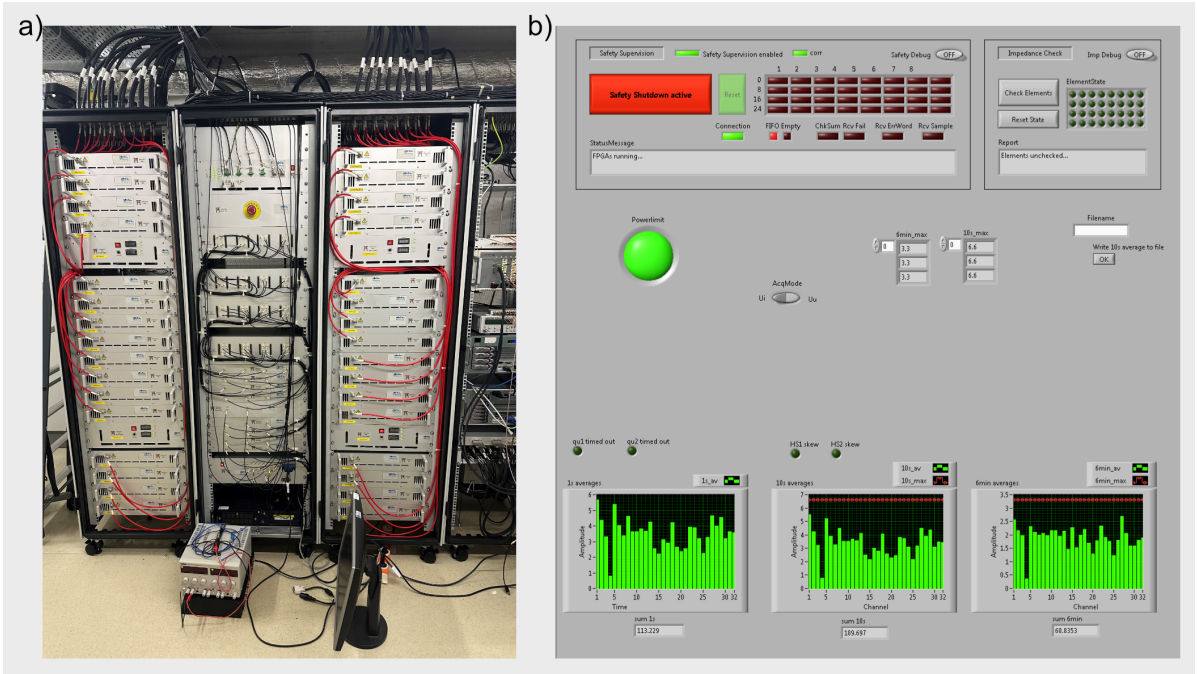

Figure 10: a) Photograph of the MRexcite system including the amplifiers and modulators. b) Safety supervision interface for the power supervision. It displays the power per channel averaged over 1 s, 10 s, and 6 min intervals. SAR is controlled by a power limit measured at the directional couplers. If any of these averages exceed their respective limits, the power output of the RF amplifiers is immediately shut off to ensure safety. The green circular button shows if the system is within the power limits. Furthermore, the safety shutdown can be manually done by pressing the red rectangular button on the top.

The interface to enable the MRexcite system, to switch between reception with local Rx coils or the remote body coil and to use different shims is shown in figure 11a). The format of an example shim file is shown in figure 11b).

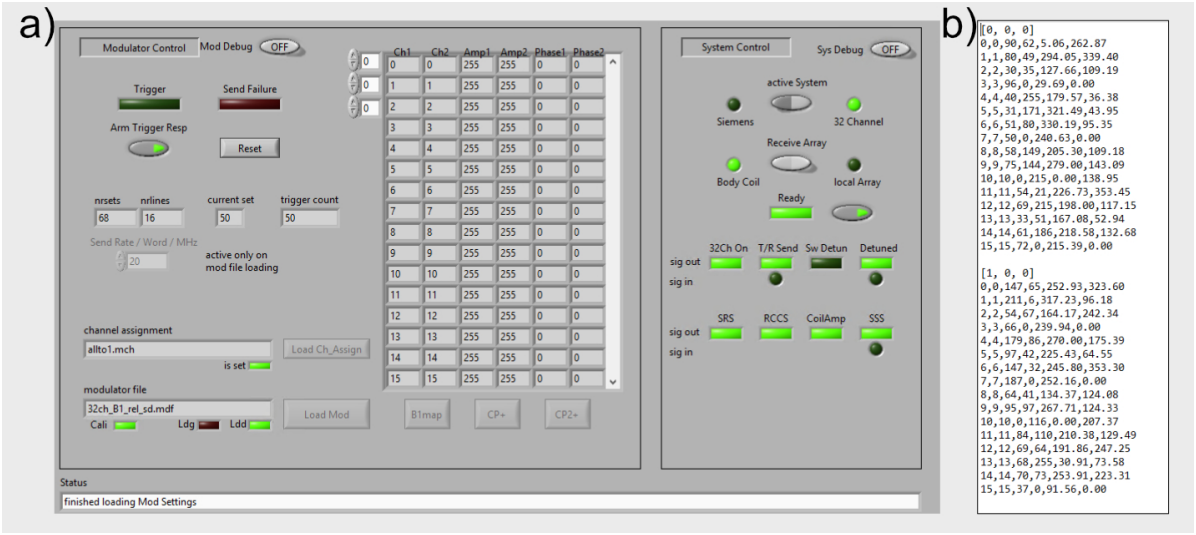

Figure 11: a) Photograph of the interface to use the MRexcite system including the selection of a modulator file to set the shims, the switches to toggle between the Siemens system and the MRexcite system and to toggle between the reception with a local Rx array or the remote array and the preview of the shimfile. b) Example modulator file to set the shims. The first line gives the shim number. Afterwards, each row consist of the element numbers i and $i+16$, the amplitude of the RF pulse with values ranging between 0 and 255, and the phase of the RF pulse with values ranging between 0° and 259°. Then the second shim, which has the same structure as the first one. By sending a trigger bit, the modulator switches to the next shim. If no shim is left, it will start from the beginning.

3.1.3 RF coil arrays

This section introduces the coils used in this thesis. A total of seven local Tx/Rx coils were utilized. Additionally, a remote coil was employed for both Tx and Rx and in combination with dedicated local Rx arrays. For an overview, all coils are summarized in table 3.

3.1.3.1 Local pTx coil arrays

The first local array (C2) is a custom-built array from German Cancer Research Center (DKFZ), Heidelberg, Germany [78] based on the coil design published by [79, 80]. This

Table 3: Coil arrays used in this work.

#	Coil type	# Tx/Rx elements	Site
C1	Remote	32/32	DKFZ, Heidelberg
C2	Local	8/8	DKFZ, Heidelberg
C3	Local	8/16	FAU, Erlangen
C4	Local	8/8	ELH, Essen
C5	Local	8/32	ELH, Essen
C6	Local	8/16	PTB, Berlin
C7	Local	8/16	PTB, Berlin
C8	Remote Tx/ Local Rx	32/32	DKFZ, Heidelberg

array consists of 8 micro strip-line meander elements which are used for both Tx and Rx. It features a flexible anterior part with 4 elements and a rigid flat posterior part with 4 elements (figure 12).

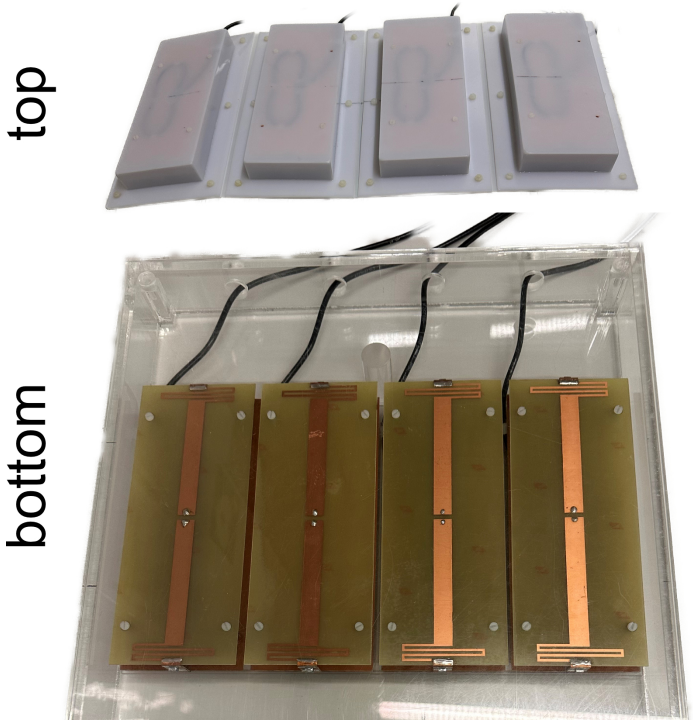

Figure 12: 8-channel TxRx body array from the DKFZ.

The second local array (C3) is a commercial array from RAPID Biomedical, Rimpar, Germany used at the Friedrich-Alexander-Universität (FAU), Erlangen, Germany and features 8 Tx and 16 Rx channels [81]. This array consists of a flexible anterior part

and a rigid posterior part (figure 13). Each part includes a central circular coil element designed to be positioned directly above the ROI. 7 additional trapezoidal-shaped loop elements surround the central element and are arranged to form a heptagonal shape. For transmit, 2 loop elements are switched together with a fixed hardware shim.

Figure 13: 8 Tx channel and 16 Rx channel body array from Rapid Biomedical.

The third array (C4), which is custom-built, originates from the Erwin L. Hahn Institute (ELH) Institute, Essen, Germany [79, 80]. Like the first array, it has 8 Tx and 8 Rx meander-type elements. The anterior part is flexible and contains 4 elements, while the posterior part is rigid but slightly curved to improve placement of the outermost elements towards the abdomen (figure 14) [82]. Furthermore, the cables connecting the switch to the elements were replaced with new shorter cables to minimize attenuation of the cables (C4*).

Figure 14: 8-channel TxRx body array from the ELH with curved posterior part.

The fourth local array (C5), another custom design (ELH, Essen, Germany), includes 8 micro strip-line meander elements as Tx and Rx elements. Additionally, it incorporates 24 Rx loop elements positioned between the meander elements and the casing of the array, closer to the subject [83]. These loops are arranged interleaved in the B_0 field direction, with 3 loop elements per meander element. As a result, this array contains a total of 8 Tx elements and 32 Rx elements (figure 15).

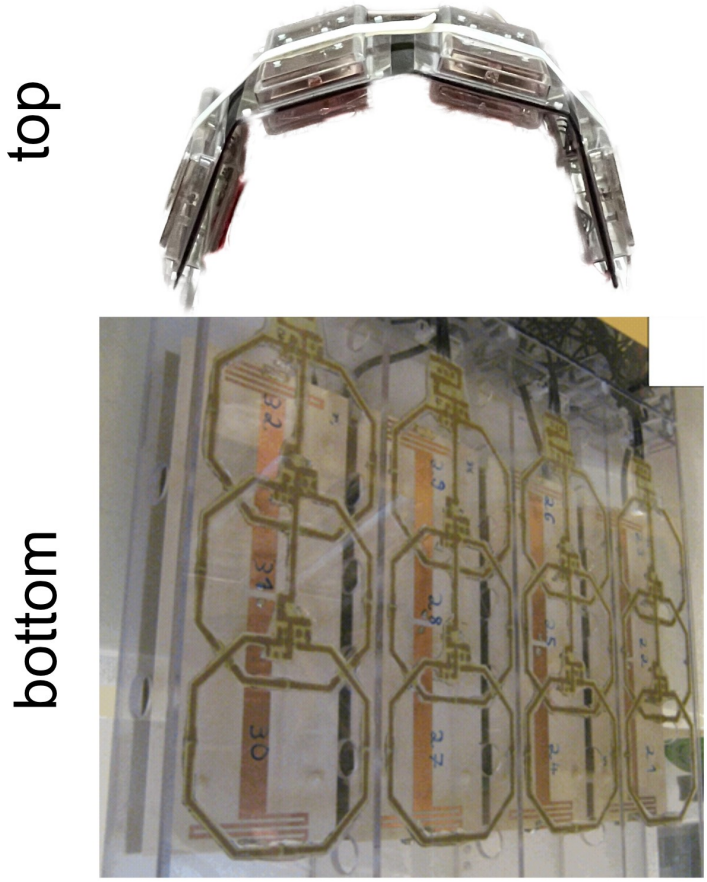

Figure 15: 8 Tx channel and 32 Rx channel body array from the ELH.

The fifth local array (C6) is a commercial 32-element body array (MRI.TOOLS, Berlin, Germany) [84]. It includes 8 dipole elements, each paired with 3 loop elements. For Tx the dipole and its loop elements are combined using a hardware-fixed phase configuration. Consequently, the array has 8 individual Tx elements and 32 Rx elements (figure 16).

Figure 16: 8 Tx channel and 32 Rx channel body array from MRI.TOOLS [85].

The sixth local array, which is custom-built (Physikalisch-Technische Bundesanstalt Berlin (PTB), Berlin, Germany), is a duplicate of the coil elements from CMRR, Minnesota, USA [86] with a modified coil housing [87] (C7). Unlike the previous three arrays, it consists of 8 dipole elements paired with 8 loop elements, where each loop element is combined with one dipole element to form one block. For Tx, the array allows transmission using either the dipole elements or the loop elements, whereas for Rx all 16 elements are used. As a result, this array contains 8 individual Tx elements and 16 Rx elements (figure 17).

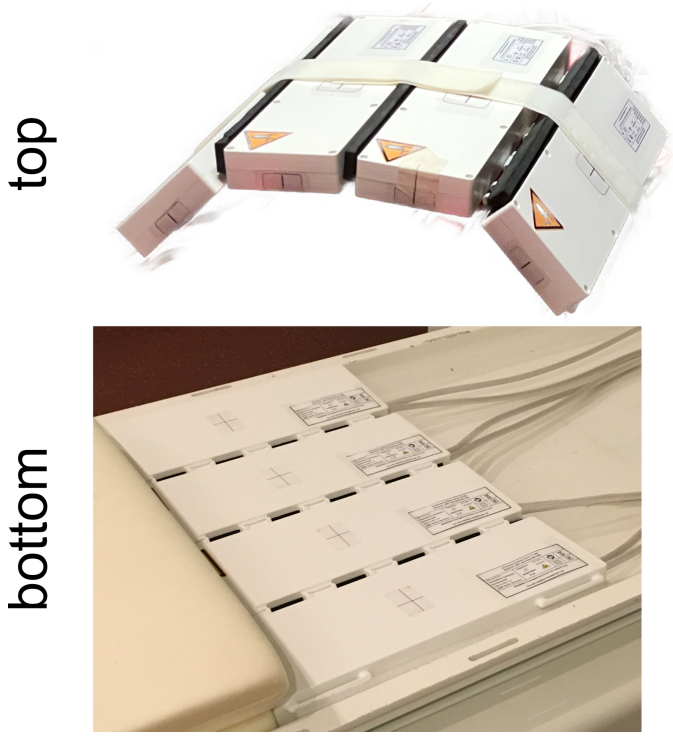

Figure 17: 8 Tx channel and 16 Rx channel body array from PTB.

3.1.3.2 Remote whole-body pTx coil array

The remote whole-body coil array (C1) is mounted on a dedicated frame and integrated between the gradient coil and the bore liner, where it is fixed to the bore liner similar to a conventional body coil at lower field strength (figure 18) [31]. This array consists of 32 micro strip-line meander elements, which can be used for Tx and Rx. The elements are arranged in three rings. The inner ring includes 12 elements, while each of the two outer rings include 10 elements. The inner ring is arranged in an interleaved fashion with the two outer rings.

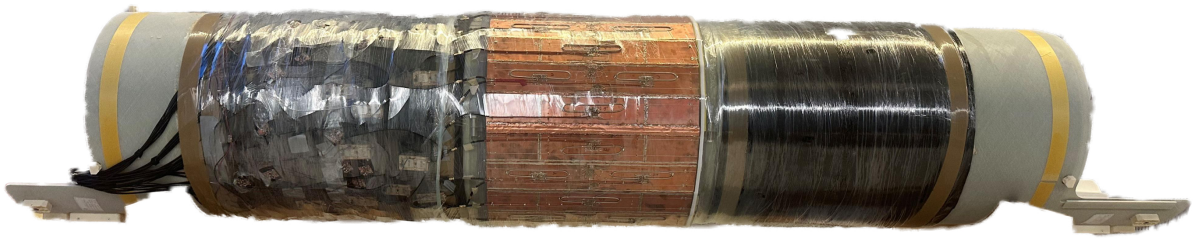

Figure 18: a) 32 Tx channel and 32 Rx channel remote whole-body coil array from the DKFZ, mounted on the scanner bore liner. The Tx/Rx switches are visible on the left side and fixed on the bore liner.

3.1.3.3 Dedicated Rx coil

The remote whole-body pTx coil array enables the use of dedicated Rx coil arrays specifically designed for reception.
The first dedicated local Rx array is a custom-built 16-channel posterior array (ELH Institute, Essen, Germany) [88]. The array is a rigid design with overlapping octagonal loops to geometrically decouple the element with the nearest neighbors (figure 19). It can be placed under the phantom or subject.

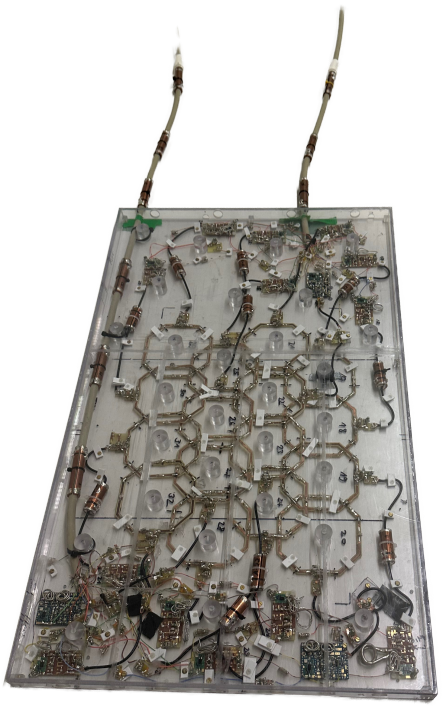

Figure 19: Rigid 16-channel Rx array used as a posterior array.

The second local Rx array is a commercial product (RAPID Biomedical, Rimpar, Germany). It also features 16 channels with overlapping loop elements placed into a rigid coil housing (figure 20). While primarily intended for the use as a posterior array, its compact design allows it to be used as an anterior array as well, particularly in the absence of a dedicated anterior array. Therefore, both local rigid arrays can be used together to create a 32-channel Rx array, which can be used in combination with the remote whole-body pTx coil array.

Figure 20: Rigid 16-channel Rx array, which can be used as a posterior and anterior array.

The third local Rx array is a also commercial product from RAPID Biomedical. It also features 16 channels with overlapping loop elements. However, they are placed into a flexible housing (figure 21). It is intended to be used as an anterior array in combination with the posterior local Rx array from RAPID to create a 32-channel Rx array, which can be used in combination with the remote whole-body pTx coil array. However, until now, it has no clearance for *in-vivo* imaging.

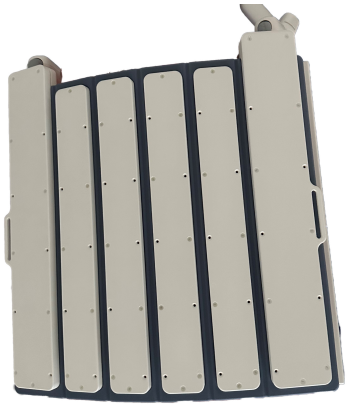

Figure 21: Flexible 16-channel Rx array, which is used as an anterior array.

3.1.4 Phantom

In this thesis one homogeneous body phantom was used for MRI measurements, which gives a comparable loading of the RF coil to that of the human body (figure 22). The phantom, constructed of acrylic glass, is filled with 49 % polyvinylpyrrolidone (PVP), 1.8 % sodium chloride and 49.2 % water to mimic the dielectric properties of tissue of the human body. It is cylindrically shaped with an oval base area and is approximately 52 cm long. The base area has a maximum height of 23 cm and a maximum width of 35 cm. The phantom was filled in 2015 and the dielectric parameters are given as $\epsilon_r = 36$ and $\sigma_c = 0.45\frac{S}{m}$.

Figure 22: Image of the body phantom.

3.2 RF pulse optimization

In the following, the RF pulse optimization methods used in this work are described. For all methods, the FA is optimized within a certain preselected ROI, while the region outside the ROI is neglected.

3.2.1 Static pTx

Both of the following shimming optimizations are usable with phase only shimming, as well as with magnitude and phase shimming. An example pulse train for an example phase only shim and magnitude and phase shim is shown in figure 23.

3.2.1.1 Homogeneity

A homogeneity shim is applied if a uniform FA distribution within the ROI is needed [18]. Therefore, a minimization problem is solved, which minimizes the CV (c.f. equation (2.72)) within the ROI. The optimization is carried out with 8 sets of pseudo-random starting phases and equal magnitudes to avoid local minima with automatic selection of the shim with the lowest CV value.

3.2.1.2 Efficiency

In contrast to a homogeneity shim, an efficiency shim is applied if the goal is to aim at minimizing the RF power required for a given average flip angle or achieving the highest FA possible in the ROI for the same total RF power [18]. However, this can lead to large FA variations in the ROI. To optimize the RF pulse, the transmit efficiency [84] defined as

$$\eta = \frac{\left|\sum_{ch}^{N} B_{1,ch}^{+} b_{ch}\right|}{\sum_{ch}^{N} \left|B_{1,ch}^{+}\right|} \tag{3.1}$$

is maximized in the ROI.[22] Similar to the homogeneous shim, the optimization is carried out with eight sets of pseudo-random starting phases and equal magnitudes to avoid local minima and the best solution is selected automatically.

3.2.2 Dynamic pTx with k_T-points

k_T-point pulses were optimized in the small tip angle approximation [49] using the interleaved greedy and local optimization methods [89, 90] to homogeneously excite the

ROI with a nominal 10° FA solving equation (2.69) [22]. An example pulse train for two k_T-points is shown in figure 23.

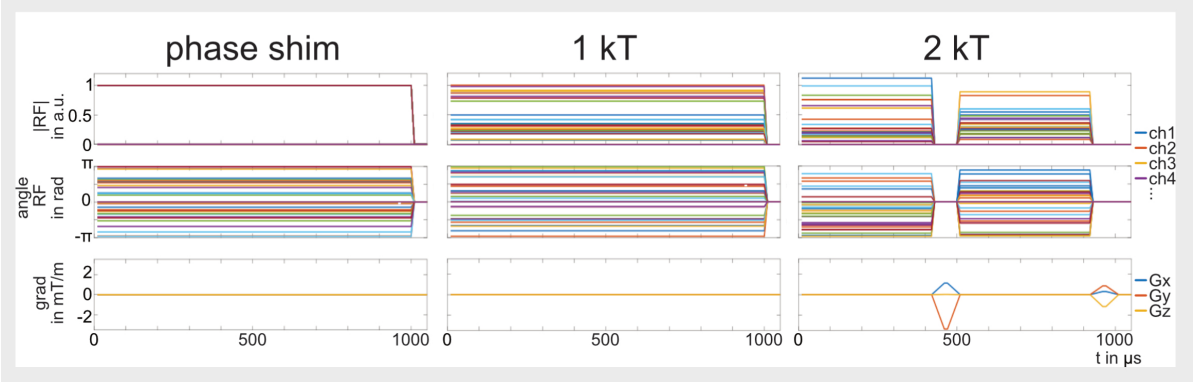

Figure 23: Example pulse diagram for phase shim, magnitude and phase shim (one k_T-point) and dynamic pTx using two k_T-points. The top line shows the magnitude of the applied RF pulse of each channel. The second row, the corresponding phases of the RF pulse and the third row the applied gradients.

3.3 B_1^+ mapping

The pulse optimization methods using pTx, as described in section 3.2, rely on prior knowledge of the transmit sensitivity $S_i^+(\vec{r})$ off the individual elements i which is obtained through B_1^+ mapping. The following section explains the different methods used for B_1^+ mapping.

3.3.1 Relative channel-wise B_1^+ mapping

The relative B_1^+ mapping approach of a coil with N_{Tx} Tx channels and N_{Rx} Rx channels involves the acquisition of fast $N_{Tx} + 2$ low FA gradient recalled echo (GRE) images [91]. The first measurement is acquired with all channels being active with equal magnitudes and phase 0 to monitor the used shim file. The second measurement is acquired with all channels inactive and is used for noise decorrelation of the Rx channels during reconstruction of the images. Measurements three to $N_{ch} + 2$ are acquired with only one channel transmitting at a time, while all other channels remained inactive. During all acquisitions reception is always performed with all channels active [91]. The second measurement is used for noise decorrelation of the Rx channels during reconstruction of the images. The magnitude of the images acquired with only one Tx channel active can be expressed as

$$|I_{i,j}(\vec{r})| = \lambda \rho_0(\vec{r}) |S_j^-(\vec{r})| \cdot |S_i^+(\vec{r})|, \tag{3.2}$$

with λ a scalar, $\rho_0(\vec{r})$ the proton density at position $\vec{r}$, $|S_j^-(\vec{r})|$ the complex receive sensitivity of element j and $|S_i^+(\vec{r})|$ the complex transmit sensitivity of element i. Assuming that the sum of magnitudes (SOM) of all transmit profiles is approximately equal to the SOM of all receive channels ($\sum_i^{N_{Tx}} |S_i^+(\vec{r})| \approx \sum_j^{N_{Rx}} |S_j^-(\vec{r})|$), which was empirically observed in experiments and simulations [91], the signal intensity of the magnitude images can be expressed as:

$$\sum_i^{N_{Tx}} |\tilde{S}_i^+(\vec{r})| \approx \frac{\sqrt{\sum_i^{N_{Tx}} \sum_j^{N_{Rx}} |I_{i,j}(\vec{r})|}}{\sqrt{\lambda \rho_0(\vec{r})}}, \tag{3.3}$$

with $\tilde{S}_i^+$ the biased transmit sensitivity of channel i. The relative signal intensity of the images of each transmit channel i is given by:

$$R_i(\vec{r}) = \frac{\sum_j^{N_{Rx}} |I_{i,j}(\vec{r})|}{\sum_j^{N_{Rx}} \sum_i^{N_{Tx}} |I_{i,j}(\vec{r})|} \tag{3.4}$$

The channel-wise relative B_1^+ magnitude maps are calculated by weighting $\sum_i^{N_{Tx}} |S_i^+(\vec{r})|$

with $R_i(\vec{r})$ [91]:

$$|\tilde{S}_i^+(\vec{r})| \approx R_i(\vec{r}) \cdot \sum_i^{N_{Tx}} |S_i^+(\vec{r})| \approx \frac{\sum_j^{N_{Rx}} |I_{i,j}(\vec{r})|}{\sqrt{\lambda \rho_0(\vec{r}) \sum_i^{N_{Tx}} \sum_j^{N_{Rx}} |I_{i,j}(\vec{r})|}}. \tag{3.5}$$

The relative channel-wise B_1^+ phase maps ϕ_i of transmit channel i are calculated relative to a fixed transmit channel k:

$$\phi_i(\vec{r}) = arg\left(\sum_j^{N_{Rx}} I_{k,j}^{\star} \cdot I_{i,j}\right), \tag{3.6}$$

with arg the phase of the complex value. Thus, the relative channel-wise B_1^+ (B1R) maps are defined as:

$$\tilde{S}_i^+(\vec{r}) = |\tilde{S}_i^+(\vec{r})| \cdot e^{i\phi_i(\vec{r})} \tag{3.7}$$

B1R maps are sufficient for static pTx and k_T-point pTx pulses, since they don't rely on absolute channel-wise maps. However, this mapping approach has a drawback, due to bias introduced by the approximation $\sum_i^{N_{Tx}} |S_i^+(\vec{r})| \approx \sum_j^{N_{Rx}} |S_j^-(\vec{r})|$ approximation. Additionally, the B1R maps are biased by T_1 weighting and proton density weighting.

3.3.2 Absolute B_1^+ mapping

Absolute B_1^+ maps are essential for evaluating the resulting FA distribution across different shims, coil arrays, or for scaling B1R maps to an absolute FA. These absolute B_1^+ maps provide the B_1^+ at each spatial location $\vec{r}$ when an RF pulse with a defined voltage is applied. The values are typically expressed in units of $\frac{\mu T}{V}$ or $\frac{\mu T}{\sqrt{kW}}$, allowing for standardized comparisons or calibration of the B1R maps. Several techniques exist for absolute B_1^+ mapping, such as the actual flip angle imaging (AFI) technique [92], the saturated TurboFLASH (satTFL) method or the dual refocusing echo acquisition mode (DREAM) method [93]. However, these methods have limitations, particularly reduced accuracy for FA values below 20°. Increasing the FA to improve the sensitivity is limited by SAR constraints [94]. Therefore, a method based on the magnetic resonance fingerprinting (MRF) framework, known as B1-MRF, is utilized, which achieves high accuracy across a large dynamic range, especially at low FA [95].

Absolute B_1^+ maps can be acquired individually of each channel. However, since this is a lengthy approach and suffers from low SNR due to transmitting only with one

Tx channel per time, two methods exist achieve absolute channel-wise B_1^+ maps faster, which are explained in the following.

3.3.2.1 Hybrid absolute channel-wise B_1^+ mapping approach

For the hybrid absolute channel-wise B_1^+ mapping approach N_{Tx} channel-wise low FA GRE images are acquired while transmitting only with one element at a time and receiving always with all elements. Additionally, an absolute B_1^+ map $B_{1,abs}^+(\vec{r})$, with a specific shim with weights $w_{shim} = (w_1, w_2, ..., w_{N_{Tx}})^T$ is acquired. These two measurements are combined to achieve absolute channel-wise B_1^+ magnitude maps through following equation [96]:

$$|S_i^+(\vec{r})| = |B_{1,abs}^+(\vec{r})|_{shim} \cdot \frac{|I_i(\vec{r})|}{|\sum_i^{N_{Tx}} I_i(\vec{r}) \cdot w_{i,shim}|}, \tag{3.8}$$

with I_i the complex signal of the low FA GRE image acquired while transmitting only with element i. Therefore, the same shimming vector used for the acquisition of the absolute B_1^+ map is retrospectively applied to the channel-wise complex signal of the GRE images. The relative channel-wise phase maps ϕ_i of transmit channel i are calculated similar to the relative B_1^+ mapping approach. This approach eliminates the bias introduced by the relative B_1^+ mapping approach. However, it requires a sufficiently high FA across the entire body, as FA dropouts in the absolute B_1^+ map will be propagated to the channel-wise B_1^+ maps. Thus, often two or more absolute B_1^+ maps with complementary FA dropouts are acquired and combined [97].

3.3.2.2 Biased absolute channel-wise B_1^+ mapping approach

The biased absolute channel-wise B_1^+ mapping approach combines the relative B_1^+ mapping approach with an absolute B_1^+ map. Therefore, the B1R are calibrated in one point or a small region $\vec{x}$ with the corresponding FA from the absolute B_1^+ map. Thus, the magnitude of the resulting absolute channel-wise B_1^+ maps is calculated by:

$$|\tilde{S}_{i,abs}^+(\vec{r})| = \left. \frac{|B_{1,abs}^+(\vec{r})|_{shim}}{|\sum_i^{N_{Tx}} \tilde{S}_i^+(\vec{r}) \cdot w_i|} \right|_{\vec{x}} \cdot \tilde{S}_i^+(\vec{r}) \tag{3.9}$$

The shimming vector used for the acquisition of the absolute B_1^+ map is also applied retrospectively to the B1R maps. This approach has the advantage of not requiring a sufficiently high FA throughout the entire body. However, the bias present in the relative channel-wise B_1^+ mapping is propagated to the absolute channel-wise B_1^+ maps.

3.4 SNR maps for phased arrays

In contrast to the calculation of SNR for a single coil (c.f. section 2.2.6), SNR calculation for phased arrays differs due to different noise levels across different Rx channels. The method to calculate SNR maps for phases arrays at UHF is briefly outlined below [98].

The noise covariance matrix is derived from noise-only measurements, acquired without an RF pulse, to enable noise scaling and optimal array combination. Using the singular value decomposition function in MATLAB, a de-correlation matrix is computed from the noise covariance matrix. This de-correlation matrix is then applied to "pre-whiten" the noise of the Rx channels of the GRE acquisition. Each Rx channel-wise GRE image is multiplied by the complex conjugate transpose of the de-correlation matrix, yielding de-correlated GRE images for each Rx channel (see figure 24a)).
After de-correlation, the Rx channels are combined using the ESPiRIT approach [99], producing SNR maps in standardized SNR units. As a result, SNR maps obtained for different coils or shims have the same noise level, making them directly comparable (see figure 24b) top row). However, these SNR maps are still biased by B_1^+ inhomogeneities as illustrated in figure 24b) second row. To correct for these B_1^+ variations, the SNR maps of each shim are divided by the sine of the corresponding absolute FA map, yielding FA-corrected SNR maps for each shim or coil (see figure 24b) bottom row).
Despite the B_1^+ correction, FA dropouts remain uncorrected. To address this dropouts, SNR maps are acquired for different shims with complementary FA dropouts. The SNR maps of different shims are then combined using the following equation [97]:

$$SNR_{combined} = \frac{SNR_{Cp+} \cdot (FA_{Cp+})^2 + SNR_{Cp2+} \cdot (FA_{Cp2+})^2 + SNR_{eff} \cdot (FA_{eff})^2}{(FA_{Cp+})^2 + (FA_{Cp2+})^2 + (FA_{eff})^2}, \tag{3.10}$$

with SNR the FA corrected SNR maps and FA the corresponding absolute FA maps. This combination results in the final FA corrected SNR map of each coil, ensuring a more accurate comparison across different coils (figure 24 c)).

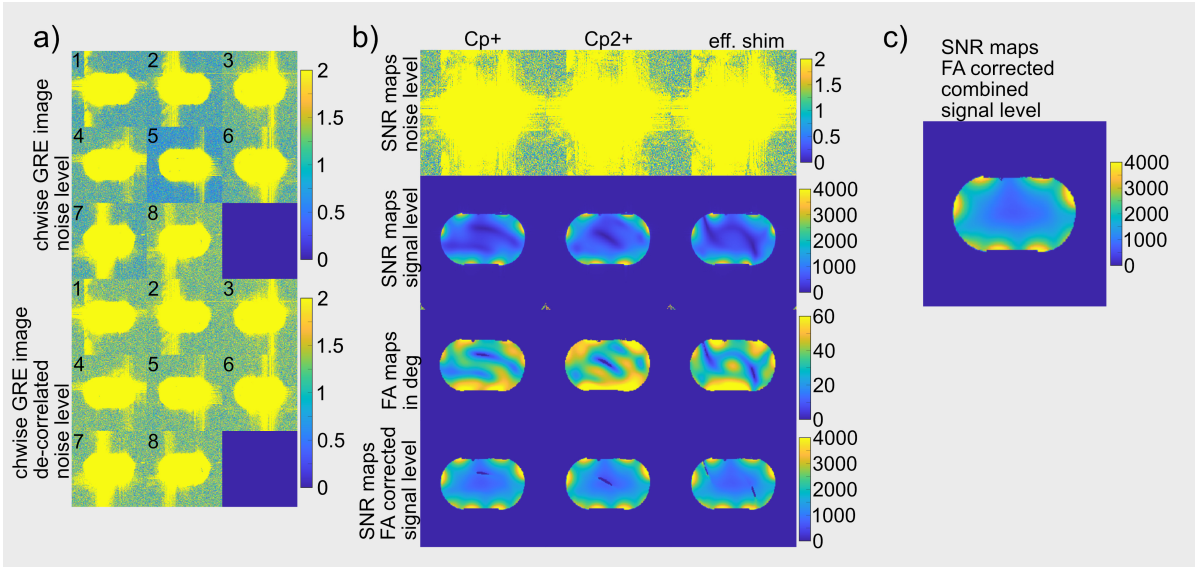

Figure 24: SNR calculation procedure for the 8Tx8Rx array from Heidelberg.
a) Rx channel-wise GRE images (top) and de-correlated channel-wise GRE images (bottom). b) SNR maps and FA maps for all three shims. c) Final SNR map, which is FA corrected and combined from the SNR maps acquired with the Cp+ mode, Cp2+ mode and the efficiency shim.

3.5 G-factor maps

Parallel imaging reconstructions lead to spatially varying noise amplification, which is quantified by the g-factor. The pseudo multiple replica method enables the estimation of the g-factor using a noise-only pre-scan and a single GRE acquisition. This method is described in the following section [100].

The pseudo multiple replica method assumes, that repeatedly acquired k-space data differs only in its noise content, while the signal component remains unchanged. By adding synthetic complex noise—properly scaled and correlated between coil array elements—directly to k-space, the characteristic spatial variance of noise emerges only after image reconstruction. The linearity of the reconstruction process ensures that Gaussian-distributed white noise in the received NMR signal is transformed into Gaussian noise in the image domain.
The scaling and correlation of noise is determined from a noise-only scan, where an image is acquired without an RF pulse allowing for the calculation of the noise covariance matrix. To ensure an accurate representation of noise characteristics, this scan must be performed using the same measurement setup as the GRE acquisition.

This method enables the generation of an arbitrary number of noise replicas. The g-factor map is determined by computing the standard deviation of the accelerated reconstruction of the replicas σ_{R_x} for a given acceleration factor R_x and the standard deviation of the unaccelerated reconstruction of the replicas σ_{R_1} [59]:

$$g(i,j) = \frac{\sigma_{R_x}(i,j)}{\sigma_{R_1}(i,j)\sqrt{R_x}}, \tag{3.11}$$

with i, j the pixel position.

3.6 Pulse sequences and image reconstruction

In this section, the utilized pulse sequences are explained and the purpose for which they are used for. Furthermore, the reconstruction of the 3D sequences is briefly explained.

3.6.1 Absolute $B_1{}^+$ mapping

To evaluate the resulting FA distribution across different shims or coil arrays, it is essential to accurately map this distribution (c.f. section 3.3.2). Therefore, a sequence based on the MRF framework, known as B1-MRF, is used [95]. This sequence achieves the FA distribution of a single slice with 2x2 mm^2 resolution in 41 s and due to its radial acquisition can be acquired in free-breathing. The absolute FA distribution obtained from B1-MRF in *degrees* is converted to μT using the following equation: The B_1^+ distribution normalized with the input power ($\frac{\mu T}{\sqrt{kW}}$) can be calculated from the obtained FA distribution using the following equation [47]:

$$|B_1^+| = 11.7\mu T \cdot \frac{FA_{absolute}}{FA_{nominal}} \cdot \frac{1}{\sqrt{N_{ch} \cdot \frac{U^2_{transmitter}}{50\Omega} \cdot 10^{-3}}}, \tag{3.12}$$

with 11.7 µT the $|B_1^+|$ necessary to achieve a 180° pulse with a 1 ms long rectangular excitation pulse, $FA_{absolute}$ the actual FA distribution measured with the B1-MRF, $FA_{nominal}$ the nominal FA set in the sequence protocol, N_{ch} the number of Tx channels and $U_{transmitter}$ the transmitter reference voltage.

3.6.2 2D relative $B_1{}^+$ mapping

B1R maps need to be acquired for pulse optimization (c.f. section 3.3.1). Thus, for the MRexcite system, a default Siemens GRE sequence was adapted using the Siemens integrated developement environment for applications (IDEA). By compiling the sequences within IDEA, executable sequence files are generated, which can be used on the scanner. A trigger bit (oscbit 1) was added before each measurement to switch between different pulses in the modulator file. Additionally, for measurement two, the sequence was modified to not transmit an RF pulse, since setting amplitude zero in the modulator file suppresses the pulse with −40 dB but does not disable the RF pulse. Additionally, a modulator file to set the shims on the modulators was created, which follows the approach by van de Moortele [91].

3.6.3 3D relative $B_1{}^+$ mapping

A GRE with an RPE acquisition scheme (GRE-RPE) was used as a basis of the 3D relative B_1^+ mapping sequence, which allows free-breathing acquisition and the possibility to resolve the respiration [101, 102]. As described in section 2.2.3 this has the advantage of motion-robustness. Hereby, the RO direction is acquired in cartesian fashion and the two PE directions are sampled on a radial grid. After each RO line the position of the next line is rotated by a golden-angle increment of 11.24° [103]. Combining this GRE-RPE sequence with the relative B_1^+ mapping approach described in section 3.3.1 achieves estimated 3D relative B_1^+ maps of all channels [84].
Thus, for the MRexcite system and similar to 2D relative B_1^+ mapping, a trigger bit (oscbit 1) was added before each measurement in the GRE-RPE sequence to switch between the different settings in the modulator file using IDEA. Additionally, for measurement two, the RF pulse was switched off.

3.6.4 3D k_T-points sequence

The GRE-RPE sequence was modified similarly to Aigner et al. [22] to o enable the application of optimized k_T-points *in-vivo* or in phantom experiments. Therefore, the rectangular RF pulse was replaced with an arbitrary RF pulse shape, defined in an external file. Since phase and magnitude shimming of each individual subpulse is managed via the modulator file, the external file contains a rectangular pulse waveform form with the appropriate number of k_T-points, all set to magnitude 1 and phase 0 for all channels. Additionally, an arbitrary gradient in all three dimensions is incorporated, synchronized with the RF pulse. The external file also defines the gradient waveforms, which consist of gradient blips applied between the RF subpulses (see figure 25). Furthermore, a trigger bit (oscbit 1) was inserted in the sequence before each RF subpulse to enable switching between different shims.

3.6.5 GRE-SNR sequence

The SNR was calculated using the Siemens default GRE sequence with a long repetition time to allow full T_1 recovery. This ensures that the signal depends solely on the receive sensitivity and sine(FA) eliminating any dependence on the T_1 of the phantom. Additionally a high FA was set to maximize the signal. More information about default sequences can be found in standard literature such as Bernstein et al [46].

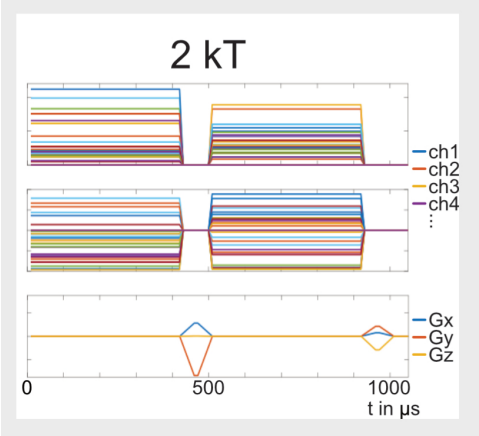

Figure 25: Example k_T-point pulse train for 2 k_T-points showing the magnitude and phase of the RF pulse of each channel. Additionally the gradient blips in x-, y-, and z-direction are shown.

3.6.6 Reconstruction of the GRE-RPE

The GRE-RPE sequence can be subdivided into different respiratory states due to its radial acquisition in both PE directions. The data of each respiratory state can be reconstructed using non-uniform fast Fourier transform (NUFFT) based on iterative SENSE [59, 102, 104]. The 3D relative B_1^+ maps were reconstructed over all respiratory phases as it was shown, that if the subjects performed shallow breathing during the measurement, the raw data could be reconstructed without respiratory binning [105]. These 3D relative B_1^+ maps were reconstructed on a separate workstation (8 cores with 2.3 GHz and 256 GB RAM) in ∼4 min.
The 3D k_T-points GRE-RPE sequence was also reconstructed averaging over all respiratory phases on a workstation with 16 cores with 2.3 GHz and 512 GB RAM in ∼50 min.

3.7 Measurements and data analysis

This section gives an overview of the measurements performed in this work and the corresponding evaluation methods of the data.

3.7.1 Transmitter voltage

The transmitter voltage was set to 350 V for the MRexcite system and 170 V per Tx channel for the Siements pTx system before each measurement.

3.7.2 Comparison of various pTx RF body arrays for 7 T body imaging

The comparison of the different pTx arrays was conducted using the 8x1 kW pTx Siemens system for all transceiver coils except for the remote body array where the MRexcite system was used. Seven transceiver RF arrays and one dedicated local Rx array from four different sites were evaluated (c.f. section 3.1.3): C1: 32Tx32Rx DKFZ, C2: 8Tx8Rx DKFZ, C3: 8Tx16Rx FAU, C4: 8Tx8Rx ELH, C4*: 8Tx8Rx ELH using new and shortened cables to connect the elements with the switch box, C5: 8Tx32Rx ELH, C6: 8Tx32Rx PTB, MRITools, C7 dipoles: 8Tx16Rx PTB using dipoles as transmit, C7 loops: 8Tx16Rx PTB using loops for transmit and C8: 32Tx32Rx DKFZ using the remote 32Tx array for transmit only and additionally the dedicated local Rx array for receive. The 8Tx8Rx array from ELH was measured before and after replacing the cables, which connect the elements of the array with the Tx/Rx switch box. C2, C4 and C5 used the same Tx/Rx switch box, while the other coils used their individual switch boxes to switch between Tx and Rx during the sequences.
All coils were centered on the identical phantom (c.f. section 3.1.4) that were subsequently placed in the isocenter of the scanner (see figure 26).
Afterwards second-order B_0 shimming was performed using the vendor provided B_0 shimming routine. Transverse 2D multislice B1R maps were acquired covering the entire phantom with 3 mm isotropic resolution. A circular ROI with a radius of 3 cm was drawn in the isocenter slice in the phantom center using MATLAB. Therefore, a ellipse was semi-automatically drawn around the phantom in the root sum of squares (rsos) B1R maps. The center of this ellipse marks the center point of the phantom. The circular ROI was then created using the center of the phantom as the center point of the circle with a radius of 3 cm.
Phase-only B_1^+ efficiency shimming was performed within the ROI while neglecting the

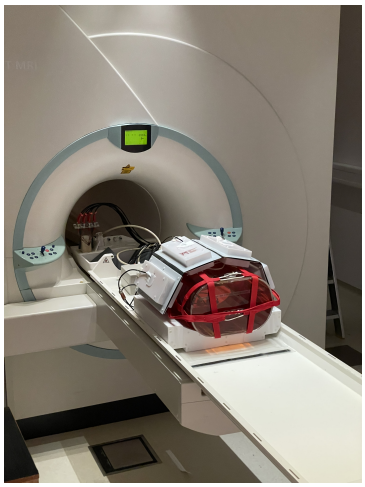

Figure 26: Example measurement setup used for the RF array comparison showing the 8Tx8Rx array from ELH. The posterior part and the phantom were aligned in left-right (lr)-direction and hf-direction using the alignment laser of the scanner. After both were aligned, the anterior part of the array was placed in the center of the alignment laser.

FA distribution outside of the ROI (c.f. section 3.2.1).
Absolute 2D B_1^+ maps were acquired in the isocenter using the 2D B1-MRF sequence using the i) CP+ mode, ii) CP2+ mode and iii) efficiency shim in the transverse orientation. Additionally, the GRE-SNR sequence was acquired in the transverse orientation with all three shims. Corresponding sequence parameters of this measurements are shown in table 4.

First, the maximum, mean and standard deviation B_1^+ values normalized with the input power and maximum and mean transmit efficiency value in the ROI are calculated for the efficiency shim for each coil.

Second, the field-of-excitation in the hf-direction was evaluated using two different approaches. For both approaches the SOM of the 3D B1R dataset along the Tx channels is calculated, which assumes 100% constructive interference of all channels. The first approach defines the excitation coverage as the region where the SOM value remains above 70% in the hf direction, relative to the maximum value at the transverse center slice (see figure 27). This excitation coverage is evaluated at five different positions, which are shown in figure 27b). The second approach also utilizes the B1R SOM across all channels but evaluates the excitation profile along the isocenter line scaled to the

maximum B_1^+ value. Therefore, the value at position $x = 0$ in hf-direction is multiplied with the maximum $B^+_{1,max} = B_{1,max,normalized} \cdot \sqrt{P}$, with $P = 64kW$ for the MRexcite system and $P = 16kW$ for the Siemens pTx system (2 kW per channel). In this case, the excitation coverage is defined as the range where the excitation profile exceeds 15 µT. As some coils were not placed perfectly in the center in hf-direction, the maximum value of the excitation profile is used.

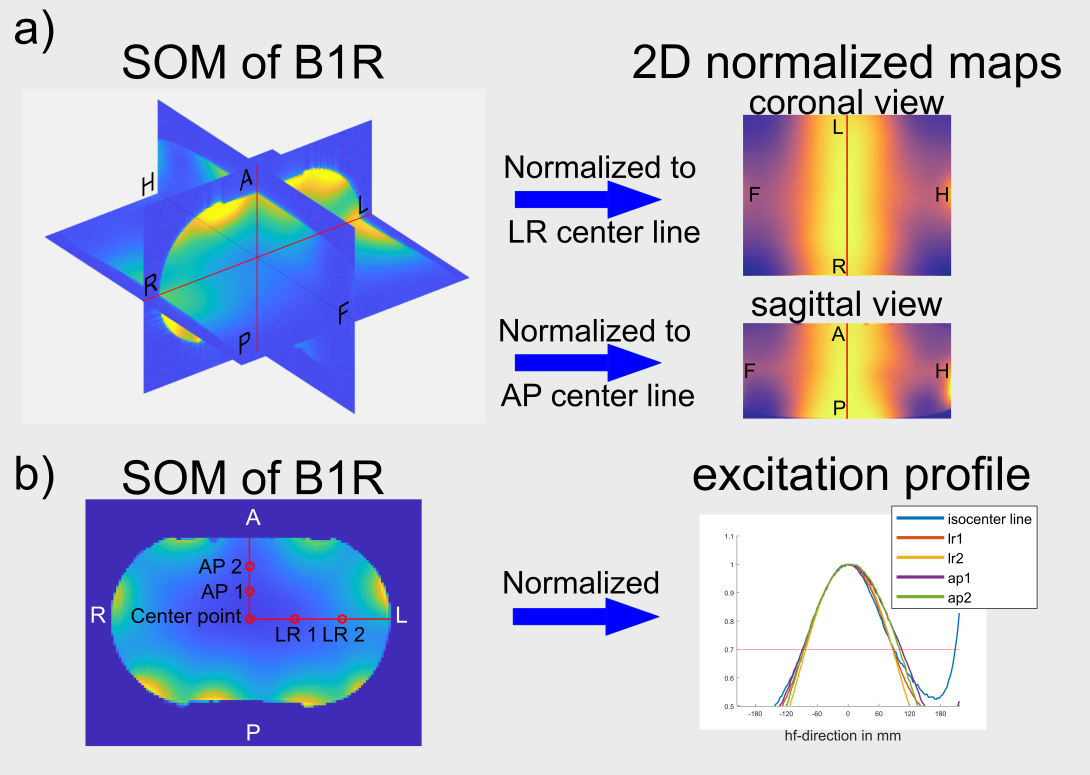

Figure 27: Procedure to evaluate the excitation profiles in hf-direction. a) For 2D sagittal and coronal slices normalized to the center line marked in red and b) excitation profile in hf-direction, marking the positions of the excitation width profiles with red circles in the transversal center SOM B1R slice. Each profile is normalized to the center line marked in red. In both, anterior-posterior (ap)-direction and left-right (lr)-direction, the positions are equidistantly distributed between the center and the edges of the phantom. This results in the closest point being approximately 3 cm away from the top surface of the phantom and approximately 6 cm away from the left side of the phantom edge.

Third, the SNR maps of all coils are calculated from the GRE-SNR sequence following

Kellman et al. [98] and as described in section 3.4: For each shim, the noise covariance matrix is calculated from the noise scan of the center slice of the B1R measurement. The Rx channels are de-correlated and combined using ESPIRiT [99] achieving the final SNR map for one shim in SNR units. To correct for B_1^+, the SNR maps for each shim were divided by the sine of the corresponding FA map acquired from the B1-MRF sequence. The different shims were combined following Brunheim et al. [97] to obtain a FA corrected combined SNR map for each coil.

Fourth, noise correlation matrices of all arrays are calculated from the noise covariance matrices using the MATLAB internal function. Mean noise correlation was calculated for all arrays using the off-diagonal entries of the matrix.

Fifth, g-factor maps are obtained up to acceleration of R=5 in anterior-posterior (ap)-direction and left-right (lr)-direction for all coils as described in section 3.5. Therefore, sensitivity maps are calculated from the GRE-SNR measurement with the CP+ mode using the approach from Walsh et al. [106] for each coil. From 1000 white noise matrices g-factor maps are calculated for each acceleration factor (R1-R5) in lr- and ap-direction using SENSE.

Table 4: Overview of the sequence parameters used for the coil comparison phantom measurements.

Sequence	TE in ms	TR in ms	TA in min	FoV read in mm	FoV phase	nom. FA	voxel size in mm^3	base resolution	slices	slice distance	BW in Hz/Px
B1R	2.9	860	13:47	384	75%	20	3x3x3	128	144*	0%	450
B1-MRF	2.35	4.7	0:40	512	100%	60	2x2x5	128	1	0%	590
GRE-SNR	2.81	2000	8:22	500	100%	60	2x2x5	250	1	0%	440

*MRexcite system: 128

3.7.3 Validation of the RF pulse optimization and the modified sequences

The RF pulse optimization method and the modified sequences are validated in the body phantom using the MRexcite system and the remote 32-channel whole-body array as Tx in combination with the two dedicated rigid local Rx arrays. Both rigid arrays have been used as the flexible array has not yet been approved for *in-vivo* measurements and the same local arrays should be used for phantom measurement and *in-vivo* measurements for this study.

Therefore 3D relative B_1^+ maps of the phantom were acquired using the 3D relative B_1^+ mapping sequence (section 3.6.3). After reconstruction of the maps, an ROI was manually drawn on the right half of the phantom mimicking the size and position of the liver on every fourth slice. Two and three k_T-points were optimized as explained in section 3.2.2. The optimized shims were applied in the phantom using the 3D k_T-points sequence to qualitatively compare the resulting FA predictions of the optimization and the signal magnitudes of the small FA acquisitions. The sequence parameters are shown in table 5.

Table 5: Sequence parameters for phantom measurement.

Sequence	TE in ms	TR in ms	TA in min	FoV in mm^3	RPE lines	total RF power of all channels in W		voxel size in mm^3	BW in Hz/Px
						zero-phase shim	k_T-points		
3D B1R	2.04	5.0	11:38	500x500x256	256	∼10		4x4x4	355
3D k_T-points GRE-RPE	1.84	3.82	4:18	500x500x250	1536	∼36	∼33	1.4x1.4x1.4	1015

3.7.4 *In-vivo* studies

Two *in-vivo* studies were conducted to investigate the application of static pTx and dynamic k_T-point pulses in body imaging with the MRexcite system and the remote 32-channel whole-body coil array. The first study focused on the liver excitation, while the second targeted an even larger excitation region namely the entire abdomen. Both are described in the following.

3.7.4.1 Investigation of homogeneous liver excitation using static and dynamic pTx

This section has been summarized in a research article that is currently under review in *NMR in Biomedicine*.

All measurements were performed with the MRexcite system and the remote 32-channel whole-body coil array in combination with the two local rigid 16-channel Rx arrays for reception. Five healthy volunteers (two male and three female, body mass index (BMI) range = 19.5 - 26.2 $\mathrm{kg\,m^{-2}}$) were scanned in head-first supine position. The subjects were placed such that the liver is in the isocenter of the coil and the scanner. Figure 28 shows the experimental setup.

Figure 28: Measurement setup with two local rigid 16-channel receive arrays. The Rx array from the ELH is placed in the patient table and the Rapid Rx array is placed on the subject.

Written informed consent according to to the institutional guidelines and approval from the local ethics committee was obtained before the scanning session.

Calibration measurements:
For each subject, the RF power of the pulses were adjusted to be within the power limits of the safety supervision (c.f. section 3.1.2). Second-order B_0 shimming was performed optimizing the liver region. 3D relative B_1^+ maps of the liver were obtained for all channels during free breathing with 4 mm isotropic resolution in 11:38 min. Please note the increased scan time compared to previous works [22, 84] due to the fourfold larger number of Tx channels. Further measurement parameters are shown in table 6. The subjects performed shallow breathing during this measurement, thus the raw data can be reconstructed without respiratory binning as described in section 3.6.6.

Pulse Optimization:
On the transversal root-sum-of-squares B_1^+ images an ROI was manually drawn on every fourth slice covering the whole liver. This ROI was used for pulse optimization, whereas the region outside of this ROI was disregarded during the optimization.

Channels with instabilities, which are visible through low overall B_1^+ values in the relative B_1^+ maps are neglected for pulse optimization. Based on the 3D relative B_1^+ maps and within the ROI, k_T-point RF pulses with up to six k_T-points were calculated to investigate the necessary number of k_T-points for a homogeneous liver excitation using 100 random starting phases with equal magnitude to come closer to the global minimum. Additionally a phase-only homogeneity shim was calculated. The total pulse duration was fixed to approximately 1 ms with a fixed blip duration of 80 µs. This leads to a decreased duration of the subpulse with increasing number of k_T-points. Thus, the subpulse duration for one k_T-point is 1 ms, two k_T-points is 420 µs, three k_T-points is 253 µs, four k_T-points is 170 µs, five k_T-points is 120 µs and six k_T-points is 87 µs.
The regularization parameter (c.f. equation 2.70) was iterated for each k_T-point between 10^{-10} and 10^3 to trade between total RF power and excitation fidelity (c.f. section 3.2.2). For the application *in-vivo* the regularization parameter was updated automatically every 50^{th} iteration [89].

Analysis:
The influence of the number of k_T-points on the excitation fidelity within the ROI using

the 32-channel array was investigated based on L-curves. These L-curves were generated for each of the six k_T-point pulses for each subject by plotting the root mean squared (RMS) RF voltage, which is defined as the vector or matrix norm of the RF shim weights versus the CV of the FA within the ROI. To allow for a direct comparison, the total pulse duration was fixed to 1 ms as stated above including the gradient blips.
The impact of the number of Tx channels on the resulting FA homogeneity was examined for the first three subjects by calculating additional L-curves for phase shimming and one to five k_T-point pulses with i) 8 Tx channels, ii) 16 Tx channels, iii) 20 Tx channels. Therefore, multiple elements within a block are combined using the complex sum, resulting in a new, merged "element." This combination of elements is shown in figure 29. The total available RF power was set to be identical for all four settings.

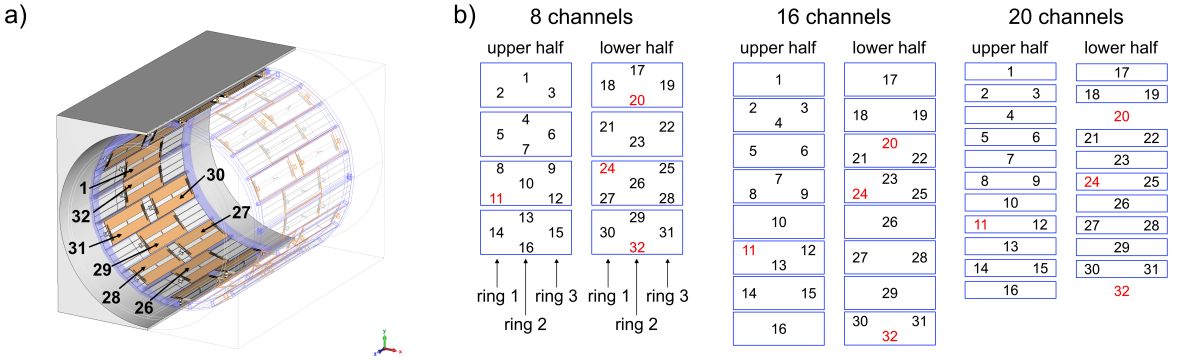

Figure 29: a) Schematic of the remote 32-Tx-channel array. The remote array is arranged into 3 rings, where the two outer rings consist of 10 elements and the inner ring of 12 elements. The array is split into two halves (element 1-16 and element 17-32) b) Combination of elements of the 32-channel remote array to achieve 8, 16 and 20 Tx channels are marked with a blue rectangular. Elements with instabilities are marked in red and are neglected for pulse optimization.

Validation:

The predicted FA distributions are qualitatively validated *in-vivo* using the free breathing 3D k_T-points sequence (Section 3.6.4) with one and two k_T-points in all subjects. Furthermore, a phase-only homogeneity shim and a zero-phase shim were obtained. To keep the total RF power constant for all measurements, the nominal FA of the sequence was adjusted for each acquisition. The sequence parameters are displayed in table 6.

Table 6: Sequence parameters for the *in-vivo* liver study.

Sequence	TE in ms	TR in ms	TA in min	FoV in mm^3	RPE lines	total RF power of all channels in W			voxel size in mm^3	BW in Hz/Px
						zero-phase shim	static pTx	k_T-points		
3D B1R	2.04	5.0	11:38	500x500x256	256	∼10			4x4x4	355
3D k_T-points GRE-RPE	1.84	3.82	4:18	500x500x250	1536	∼29	∼25	∼25	1.4x1.4x1.4	1015

3.7.4.2 Investigation of homogeneous abdomen excitation using static and dynamic pTx

This *in-vivo* study was performed in three subjects (one male and two female, BMI range = 21.9 - 25.1 $\mathrm{kg\,m^{-2}}$) using the MRexcite system with the remote 32-channel body coil array integrated into the scanner bore for both Tx and Rx. Written informed consent according to to the institutional guidelines and approval from the local ethics committee was obtained before the scanning session. The subjects were placed in head-first supine position in the scanner with the center of the abdomen placed in the isocenter in lr- and ap-direction and bottom part of the right liver lobe in hf-direction (see figure 30).

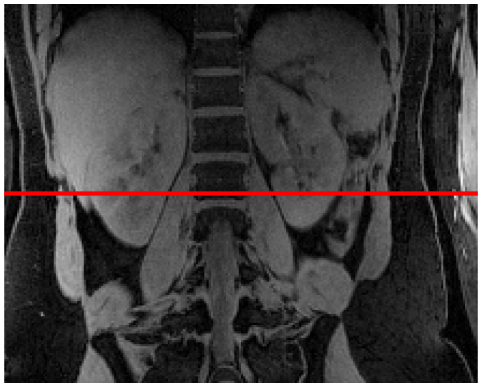

Figure 30: The subject is placed head-first supine position in the scanner with the bottom part of the right liver lobe placed in the center, marked with the red line.

After vendor-provided second order B_0 shimming of the abdomen, relative 3D B_1^+ maps were acquired in free breathing in 23:14 min with 4 mm isotropic resolution. As the subjects performed shallow breathing during this measurement (section 3.6.6), the raw data is reconstruction without respiratory binning. Afterwards, an ROI was manually drawn on every eighth transversal slice of the root-sum-of-squares B_1^+ images covering the whole abdomen. The parameters for the scan are listed in table 7.

Table 7: Sequence parameters for the *in-vivo* abdomen study.

Sequence	TE in ms	TR in ms	TA in min	FoV in mm^3	RPE lines	total RF power of all channels in W			voxel size in mm^3	BW in Hz/Px
						zero-phase shim	static pTx	k_T-points		
3D B1R	2.04	5.0	23:16	500x500x256	512	∼10			4x4x4	355
3D k_T-points GRE-RPE	1.84	3.82	4:18	500x500x250	1536	∼26	∼12	∼21	1.4x1.4x1.4	1015

Based on these relative B_1^+ maps, one to five k_T-point pTx pulses were optimized to homogeneously excite the region within the ROI while disregarding the region outside of this ROI. Using these RF pulses, the free breathing 3D k_T-points sequence (section 3.6.4) with up to four k_T-points was acquired in the first two subjects. Additionally, a zero-phase shim with magnitude 1 and phase 0 for all channels was obtained. All measurements were acquired at the allowed power limit given by the SAR supervision. To keep the total RF power constant for all measurements, the nominal FA of the sequence was adjusted for each acquisition. However, for one k_T-point, the total power could not be matched with the other acquisitions, as the per channel power limit would have exceeded the limits given by the SAR supervision. The sequence parameters are displayed in table 7.

4 Results

The results of the comparison of various existing body coils, the validation of the pulse optimization and the *in-vivo* measurements using the remote 32 Tx channel coil are shown in this chapter.

4.1 Comparison of various pTx RF body arrays for 7 T body imaging

In the following, the results of the comparison of seven pTx coil arrays for body imaging and one dedicated local Rx array are presented.

4.1.1 Tx performance

4.1.1.1 B_1^+ and transmit efficiency

Figure 31 shows the absolute B_1^+ efficiency maps reconstructed from the B1-MRF and the transmit efficiency maps for the optimized efficiency shim based on the isocenter slice of the reconstructed B1R maps for all coil configurations.
The corresponding mean, standard deviation and max B_1^+ values and transmit efficiency values within the ROI are shown in figure 32 and summarized in table 8. All local coils achieved close to 100% maximum transmit efficiency in the center ROI of the phantom. The mean efficiency ranged between 80% and 82%. The local coils yielded mean B_1^+ values in the ROI between $2.6\,\mu T/\sqrt{kW}$ and $4.3\,\mu T/\sqrt{kW}$, with C4* achieving the highest B_1^+ values. Maximum B_1^+ values in the ROI ranged between $2.9\,\mu T/\sqrt{kW}$ and $5.2\,\mu T/\sqrt{kW}$. Again, C4* achieved the highest B_1^+ values.
The 8Tx32Rx coil (C6) achieved the lowest mean and max B_1^+ values within the ROI with $2.4\,\mu T/\sqrt{kW}$ and $2.9\,\mu T/\sqrt{kW}$. The maximum B_1^+ is reduced by 34% in comparison to the 8Tx32Rx coil from ELH (C5) with the same number of Tx and Rx channels. Comparing the 8Tx8Rx array from ELH with the old and new cables (C4 and C4*) a 11% increase of the maximum B_1^+ value can be achieved with similar transmit efficiency for the array with new cables, showing the influence of the attenuation of the cables. Comparing the 8Tx32Rx array from ELH (C5) with the 8Tx8Rx array from DKFZ (C2), which has similar positions of the Tx elements in the posterior and anterior part but additional loop elements between the Tx elements and the phantom, similar transmit efficiency and B_1^+ values can be achieved within the ROI.
The 8Tx16Rx array from PTB (C7) showed 12% increase in maximum B_1^+ within the ROI using the dipoles for transmit compared to using the loops for transmit.

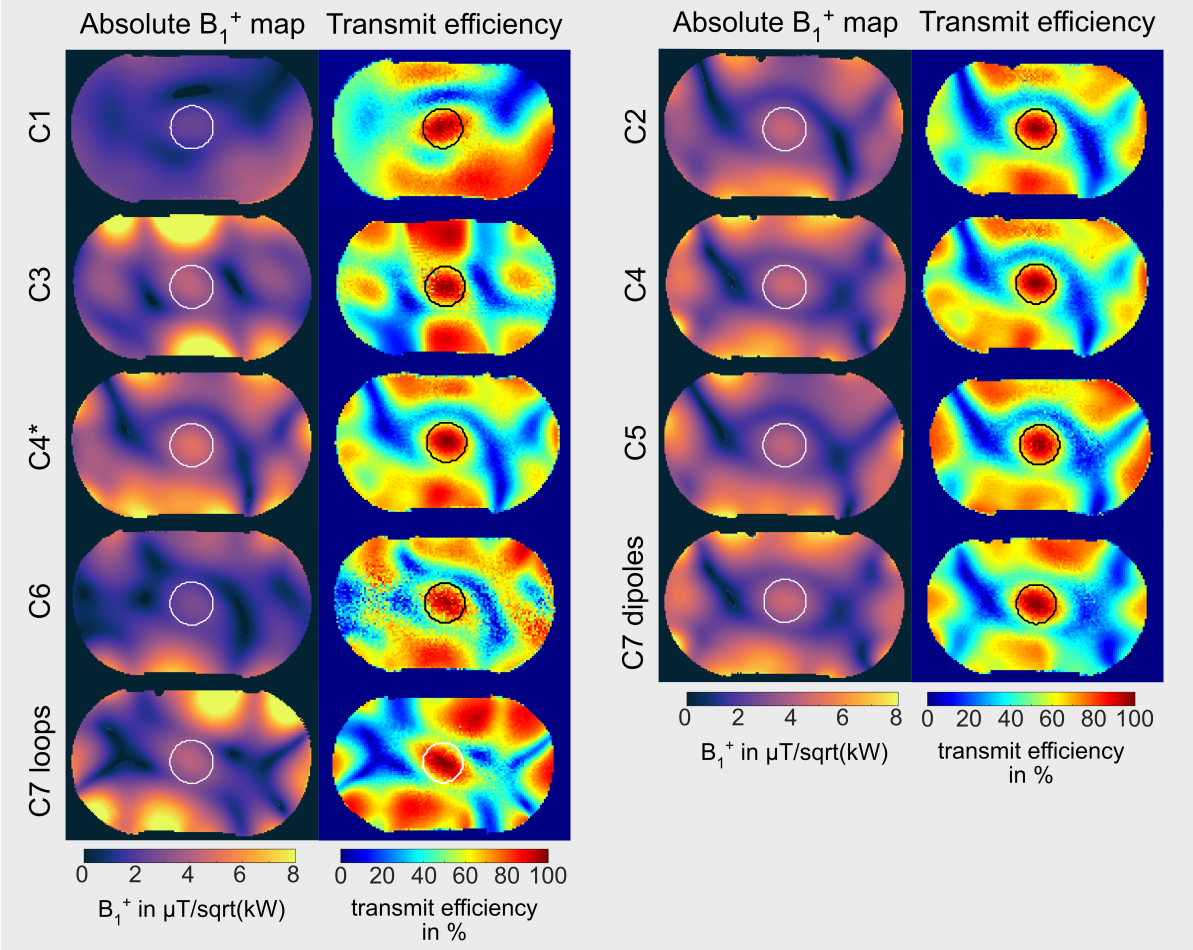

Figure 31: Absolute B_1^+ and transmit efficiency maps of an efficiency shim for all coil configurations. C1: 32Tx32Rx DKFZ, C2: 8Tx8Rx DKFZ, C3: 8Tx16Rx FAU, C4: 8Tx8Rx ELH, C4*: 8Tx8Rx ELH using the new cables connecting the elements with the switch box, C5: 8Tx32Rx ELH, C6: 8Tx32Rx PTB, MRITools, C7 dipoles: 8Tx16Rx PTB using dipoles as transmit, C7 loops: 8Tx16Rx PTB using loops for transmit.

Comparing the coil using dipoles for transmit (C7 dipoles: 8Tx16Rx coil from PTB) with the coils using 8 meander-type elements (C2, C4 and C4*), it achieved similar mean B_1^+ values within the ROI. Also the 8Tx16Rx array from FAU (C3), which uses loops for transmit obtained lower B_1^+ values within the ROI as C4/C4* using meander-type elements and C7 dipoles using dipoles elements for transmit.
The 32Tx32Rx array from DKFZ (C1, remote array) revealed lowest mean and max B_1^+ values of $2.1\,\mu T/\sqrt{kW}$ and $2.6\,\mu T/\sqrt{kW}$ since the elements are located furthest away

from the phantom. Also lowest transmit efficiency values (mean/max=76.8%/95.7%) are achieved because the B1R maps are noise contaminated.

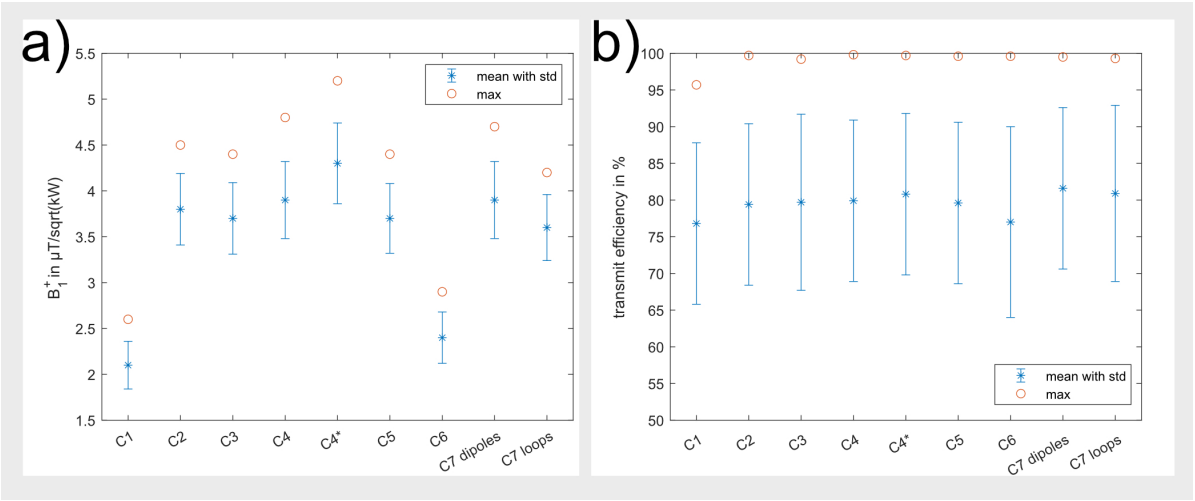

Figure 32: a) mean, std and max B_1^+ values and b) mean, std and max transmit efficiency values within the circular ROI in the center of the phantom for all coil configurations. C1: 32Tx32Rx DKFZ, C2: 8Tx8Rx DKFZ, C3: 8Tx16Rx FAU, C4: 8Tx8Rx ELH, C4*: 8Tx8Rx ELH using the new cables connecting the elements with the switch box, C5: 8Tx32Rx ELH, C6: 8Tx32Rx PTB, MRITools, C7 dipoles: 8Tx16Rx PTB using dipoles as transmit, C7 loops: 8Tx16Rx PTB using loops for transmit.

Table 8: B_1^+ and transmit efficiency.

Coil	mean B_1^+ in $\frac{\mu T}{\sqrt{kW}}$	max B_1^+ in $\frac{\mu T}{\sqrt{kW}}$	mean transmit efficiency in %	max transmit efficiency in %
C1	2.1 ± 0.3	2.6	77 ± 11	95.7
C2	3.8 ± 0.4	4.5	79 ± 11	99.7
C3	3.7 ± 0.4	4.4	80 ± 12	99.2
C4	3.9 ± 0.4	4.8	80 ± 11	99.8
C4*	4.3 ± 0.4	5.2	81 ± 11	99.7
C5	3.7 ± 0.4	4.4	80 ± 11	99.6
C6	2.4 ± 0.3	2.9	77 ± 13	99.6
C7 dipoles	3.9 ± 0.4	4.7	82 ± 11	99.5
C7 loops	3.6 ± 0.4	4.2	81 ± 12	99.3

Overall, the evaluation of the B_1^+ and transmit efficiency showed, that additional Rx

elements had no significant influence on Tx. Furthermore, dipoles achieved at least 7% higher maximum B_1^+ values than loops. Meander-type elements can achieve higher Tx performance than dipoles.

4.1.1.2 Field of excitation in hf-direction

The field of excitation in hf-direction is compared for two approaches:

1) Excitation coverage with the excitation profile normalized to 1 in the center:
Figure 33 presents the SOM of B1R in sagittal and coronal slices at the isocenter for all coil configurations, with the center normalized to 1. The corresponding profile plots at five different positions (see figure 27b)) across all coil configurations are depicted in figure 34, while table 9 summarizes the excitation coverage for each coil configuration.

The sagittal images revealed that for coils with Tx elements arranged in a single ring (C2, C4, C4*, C5, C7 dipoles, and C7 loops), the maximum excitation is achieved at the isocenter of the elements along the hf-direction, with a signal decrease towards the edges of the phantom. This trend is also reflected in the profile plots of the isocenter line. Among the local 8Tx8Rx coils with meander-type elements (C2, C4, C4*), excitation coverage remained similar, differing by only 8% at the isocenter position. C7 loops exhibited the lowest excitation coverage along the hf-direction at the isocenter position, showing a 29% reduction compared to C5. Notably, C5, which also employs 8 meander-type elements for Tx, achieved the highest excitation coverage among single-ring coils, achieving an increase between 7% and 15% compared to C2, C4 and C4*. Comparing C7 loops and C7 dipoles, the latter demonstrated a 7% improvement in excitation coverage at the isocenter position. However, coils utilizing meander-type elements (C2, C4, C4*, C5) exhibited between 12% and 33% higher excitation coverage compared to C7 dipoles. C3 and C6, both featuring multiple elements along the hf-direction, showed increased excitation coverage, which is evident in the sagittal images as well as in the isocenter line profiles. C1, the remote array, has no substantial variations in hf-direction (<15%) and, together with C6, achieved the largest excitation coverage among all coil configurations, effectively covering the entire FoV in the hf-direction.

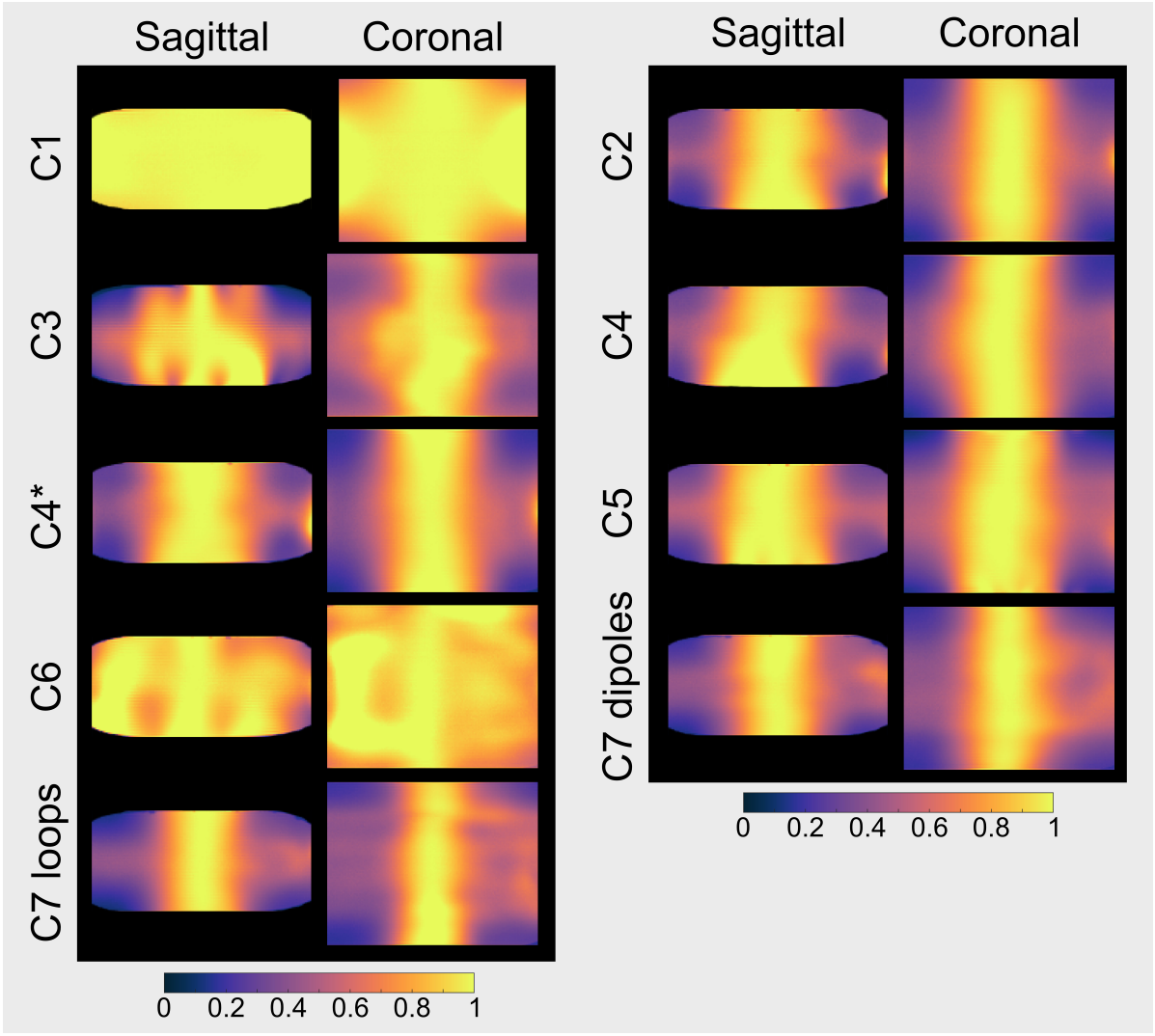

Figure 33: Sagittal and coronal normalized SOM B1R images normalized to 1 for all coil configurations. C1: 32Tx32Rx DKFZ, C2: 8Tx8Rx DKFZ, C3: 8Tx16Rx FAU, C4: 8Tx8Rx ELH, C4*: 8Tx8Rx ELH using the new cables connecting the elements with the switch box, C5: 8Tx32Rx ELH, C6: 8Tx32Rx PTB, MRITools, C7 dipoles: 8Tx16Rx PTB using dipoles as transmit, C7 loops: 8Tx16Rx PTB using loops for transmit.

Examining the hf excitation coverage at different positions along the ap direction, the sagittal images reveal that for single-ring coils (C2, C4, C4*, C5, C7 dipoles, and C7 loops), the excitation profile decreased towards the edges of the phantom, both at the head and foot sides, compared to the isocenter position. However, the excitation coverage at different ap positions (AP1 and AP2) remained within 10% of the coverage achieved at the isocenter position.

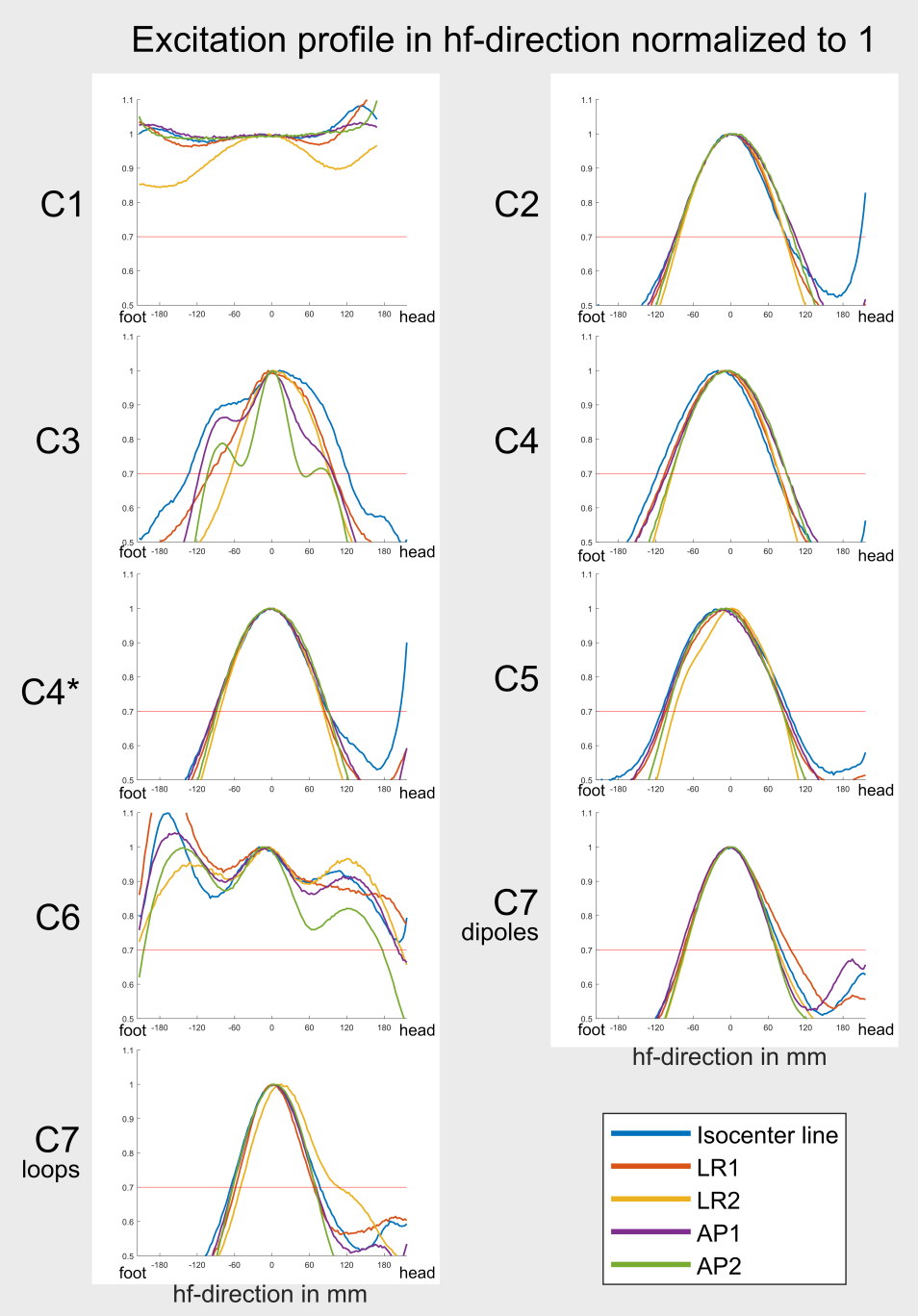

Figure 34: Hf-excitation profile for all coil configurations and for the five different positions (see figure 27b)). The horizontal red line marks the excitation coverage criterion, where the transmit signal drops by 30% in comparison to the center. C1: 32Tx32Rx DKFZ, C2: 8Tx8Rx DKFZ, C3: 8Tx16Rx FAU, C4: 8Tx8Rx ELH, C4*: 8Tx8Rx ELH using the new cables connecting the elements with the switch box, C5: 8Tx32Rx ELH, C6: 8Tx32Rx PTB, MRITools, C7 dipoles: 8Tx16Rx PTB using dipoles as transmit, C7 loops: 8Tx16Rx PTB using loops for transmit.

C3 and C6, which feature multiple elements in hf-direction showed a different pattern. For both coils, the variation of the excitation profile in hf-direction increased at positions closer to the elements (AP1, AP2). While the excitation coverage is reduced by 11% for C6 at position AP2 in comparison to the isocenter position, C3 showed a reduction of 41% at the same position, due to strong variations of the excitation profile between elements.
C1 again demonstrated minimal variation in excitation profile across AP1 and AP2, maintaining full coverage of the FoV in the hf-direction.

A similar trend is observed in the coronal images for coils with a single Tx element in the hf direction. The excitation profile peaked at the isocenter in hf-direction and decreased towards the sides of the phantom. At positions closer to the phantom's edges in the lr-direction, the excitation profile in hf-direction droped to lower values both at the head and foot sides of the phantom, compared to the isocenter position. However, the excitation coverage at different lr positions remained within 15% of the isocenter position for the single-ring coils (C2, C4, C4*, C5, C7 dipoles and C7 loops).
C6, with multiple Tx elements in the hf-direction, showed less than a 3% decrease in excitation coverage at different lr positions relative to the isocenter. However, C3 exhibited a 39% reduction at LR2 compared to the isocenter, due to its element arrangement. It has three Tx elements in the hf direction above the center in lr-direction but only a single element at positions closer to the left and right side of the phantom.
The excitation profile of C1 at position LR2 decreased by 10% towards the edges of the phantom, both at the head and foot sides compared to position $x = 0$. Despite this, excitation coverage remained unchanged at LR1 and LR2, ensuring full FoV coverage in the hf direction.

Overall, the remote 32-channel array (C1) has achieved the highest excitation coverage across the entire phantom. Among the local coils, C6 has provided the largest excitation coverage. In contrast, C7 loops has exhibited the lowest excitation coverage.

Table 9: Excitation coverage for all coil configurations and for all 5 positions in hf-direction normalized to 1.

Coil	Isocenter position in mm	LR1 in mm	LR2 in mm	AP1 in mm	AP2 in mm
C1	384*	384*	384*	384*	384*
C2	177	172.5	169.5	193.5	186
C3	256.5	198	159	214.5	150
C4	190.5	184.5	171	192	186
C4*	180	174	166.5	183	180
C5	204	189	174	195	186
C6	432*	432*	423	417	382.5
C7 dipoles	156	172.5	147	154.5	147
C7 loops	145.5	126	157.5	133.5	132

*: covering the full field of view in hf-direction

2) Excitation coverage for the isocenter line with the excitation profile normalized to maximum $B_{1,max}^{+}$ in μT:

In this approach, the achieved $B_{1,max}^{+}$ at the center and the maximum power of the pTx system are considered. Compared to approach 1, normalizing with $B_{1,max}^{+}$ offers the additional advantage of determining the maximum achievable B_1^+ along the hf-direction. This allowed for assessing the excitation coverage required to achieve a specific minimum B_1^+. The excitation profile along the isocenter line in the hf-direction for all coil configurations is shown in figure 35, and the corresponding excitation coverage values are provided in table 10.

C1, the remote array, exhibited minimal excitation profile variations (<11%) along the hf-direction, achieving a minimum B_1^+ of 23 µT, thereby surpassing the excitation criterion of 15 µT across the entire region. Additionally, the remote coil achieved the highest B_1^+ throughout the phantom. This performance is attributed to its 32 Tx elements, providing four times the total available power compared to local coils with only 8 elements. Despite having the highest excitation width among local coils in approach 1, C6, which features multiple Tx elements in the hf-direction, failed to achieve any excitation coverage in this approach. This is due to its low B_1^+ efficiency being 30% lower than that of other local coils, preventing it from reaching the required threshold of 15 µT. C3, another coil with multiple Tx elements in the hf-direction, obtained the largest excitation

coverage among local coils in this approach. This is a result of its combination of high B_1^+ efficiency and the second-largest excitation coverage in the previous approach. C6 loops achieved the lowest excitation coverage while achieving the necessary 10 µT, but it experiences a reduction of 35% to 53% compared to coils using meander-type elements. However, replacing the loop elements with dipoles in C7 dipoles improved excitation coverage by 41%.

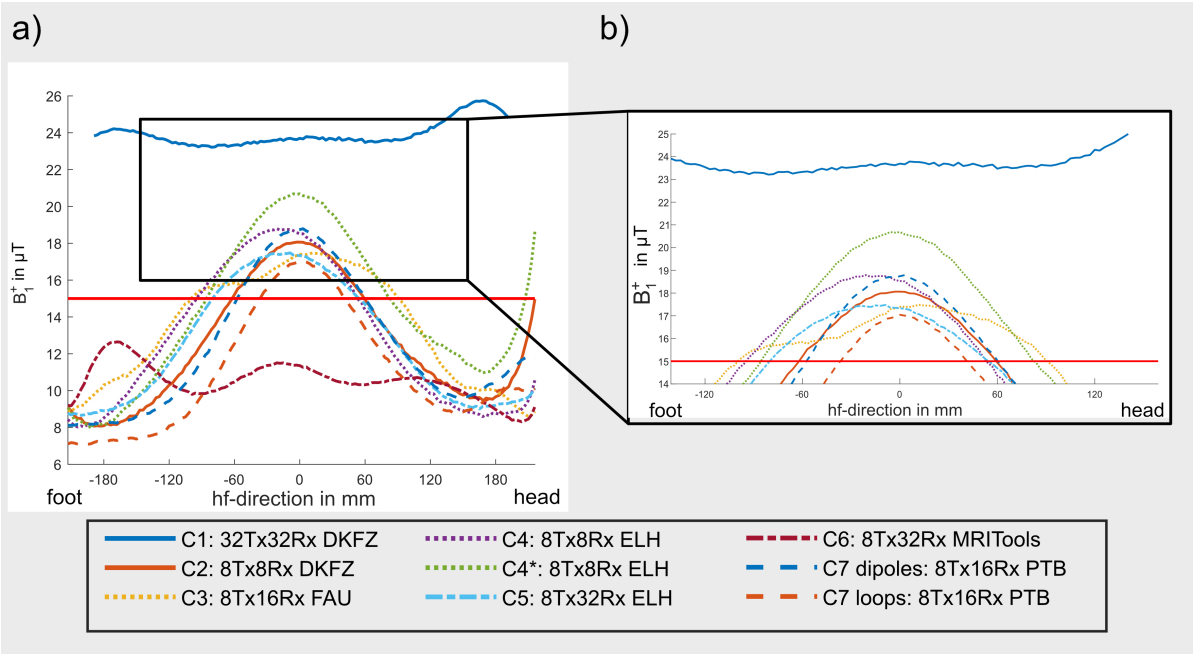

Figure 35: Hf-excitation profile for all coil configurations and for the isocenter line. The horizontal red line marks the excitation width criterion, where the transmit signal drops below 10 µT. a) showing all coil configurations and b) close up to see the differences of the local coils more in detail. C6 does not achieve 15 µT at any position.

Among the meander-type local coils (C2, C4, C4*, C5), C4* achieved the highest excitation coverage in this approach, outperforming the others by 14% to 39%.
In general, the local coils achieved higher B_1^+ values toward the head side compared to the foot side, with some coils even showing a further increase of the excitation profile near the phantom's edge on the head side. This effect arises from the influence of the cables connecting the elements to the Tx/Rx switch on the B_1^+ field.

Overall, the remote 32-channel array (C1) has achieved the largest hf-excitation cov-

erage, showing no substantial variations across the entire FoV. Despite having a 50% lower maximum B_1^+ efficiency, the remote array compensates with a 4- or 8-fold higher total available power compared to local coils, which operate with either 1 kW (older pTx systems) or 2 kW (newer pTx systems). As a result, C1 has obtained the highest maximum B_1^+ values.

Table 10: Excitation coverage in hf-direction normalized with $B_{1,max}^+$ for all coil configurations at the isocenter position.

	C1	C2	C3	C4	C4*	C5	C6	C7 dipoles	C7 loops
coverage in mm	384*	123	189	150	171	135	-	117	81

*: covering the full field of view in hf-direction

4.1.2 Rx performance

4.1.2.1 SNR

The SNR maps for all coil configurations are displayed in figure 36. To enable a more detailed analysis, SNR profiles are extracted along the lr-direction at three different positions: i) 2 cm below the top of the phantom surface, ii) at the center and iii) 2 cm above the bottom of the phantom surface. The locations of these positions are illustrated in figure 37. Figure 38 presents the SNR profiles for all coil configurations along the lr-direction at the phantom center.

Among the measured coil configurations, C8 achieved the highest SNR in the center, while C1 exhibited the lowest SNR. The lower SNR of C1 is expected, as it is a remote array with Rx elements positioned farther from the phantom, leading to reduced signal reception efficiency.

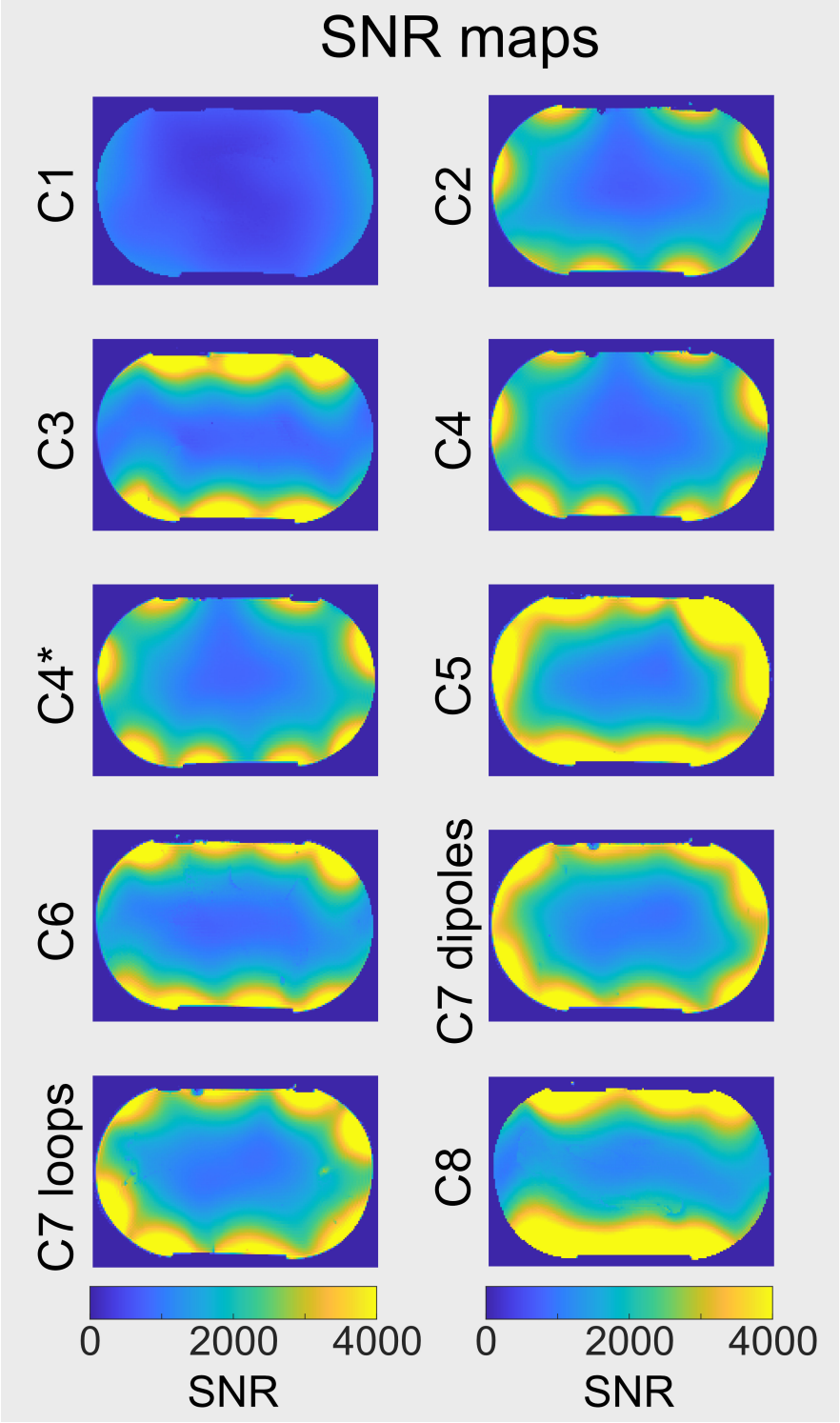

Figure 36: SNR maps for all coil configurations. C1: 32Tx32Rx DKFZ, C2: 8Tx8Rx DKFZ, C3: 8Tx16Rx FAU, C4: 8Tx8Rx ELH, C4*: 8Tx8Rx ELH using the new cables connecting the elements with the switch box, C5: 8Tx32Rx ELH, C6: 8Tx32Rx PTB, MRITools, C7 dipoles: 8Tx16Rx PTB using dipoles as transmit, C7 loops: 8Tx16Rx PTB using loops for transmit, C8: 32Tx32Rx with dedicated local Rx array.

Table 11: SNR values off all coil configurations achieved in the center.

	C1	C2	C3	C4	C4*	C5	C6	C7 dipoles	C7 loops	C8
SNR	334	706	806	802	816	1007	812	995	970	1160

All local Rx coils demonstrated higher SNR at the phantom center compared to the remote array (C1). The corresponding SNR values at the center position (x=0) are summarized in table 11.
C8 increased the SNR by 247% relative to the remote array (C1). The lowest SNR gain among the local coils is observed for configurations using 8 Rx elements (C2, C4, C4*), which resulted in SNR gains of 111%, 240%, and 244% relative to C1, respectively. Notably, C4* did not show a significant SNR increase compared to C4, indicating that the new cables have no impact on SNR.
C3, which features 16 Rx elements, performed similarly to the coils with 8 Rx elements. However, C7, which also enables 16 Rx elements, achieved an additional SNR gain of 22% to 41% at the center compared to the 8-channel configurations.
Increasing the number of local Rx elements from 8 to 32 (C5, C8) led to an additional SNR gain of 23% to 43% for C5 and 42% to 64% for C8. Despite also including 32 Rx elements, C6 achieved similar SNR values to the 8-channel configurations.

At the sides of the phantom, C5 achieved the highest SNR values. The figures also indicate, that the coils with Rx elements positioned not only on the top of the phantom but also on the left and right sides (C2, C4, C4*, C5, C7 dipoles, C7 loops), exhibited increased SNR at the the phantom sides compared to coils with elements located only on the top and bottom (C3, C6, C8). Furthermore, C4/C4*, with its upgraded coil housing, showed a 12% SNR increase compared to C2 at the sides of the phantom.

Figure 39 presents the SNR profiles for all coil configurations in the lr-direction at two positions: i) 2 cm below the top of the phantom and ii) 2 cm above the bottom of the phantom. The corresponding SNR values at the center (x = 0) are summarized in table 12.
All coils exhibited higher SNR values directly beneath or above the elements compared to positions in between them.
For position i), C3 achieved the highest SNR gain at the center, increasing SNR by 968%

Table 12: SNR values at the center position (x=0) 2 cm below/above the surface of the phantom.

	C1	C2	C3	C4	C4*	C5	C6	C7 dipoles	C7 loops	C8
SNR top	406	1009	4336	1130	1130	2695	2426	2622	2717	2661
SNR bottom	582	1900	3436	2056	2039	3270	2870	3005	3134	4602

compared to C1. The lowest SNR gain is observed for coils using 8 Rx elements, with an increase of 148% (C2) and 278% (C4, C4*) compared to C1. Increasing the number of Rx elements to 16 (C3, C7) resulted in a SNR gain of 132% (C7 dipoles) and 284% (C3) compared to 8 Rx element coils. Using 32 Rx elements (C5, C6, C8) instead of 8 Rx elements obtained an SNR increase of 115% (C6), 135% (C8) and 138% (C5).
For position ii), C8 obtained the highest SNR gain at the center, increasing SNR by 691% compared to C1. The lowest SNR gain at the center is observed for the 8 Rx element coils (C2, C4, C4*), with increases ranging from 226% to 253%. The updated coil housing in C4/C4* led to a 54% SNR increase on the left and right sides of the phantom compared to C2. Increasing to 16 Rx elements improved SNR by 67% (C3) and 46% (C7 dipoles) compared to 8 Rx elements. With 32 Rx elements, SNR gains relative to 8 Rx element coils of 40% (C6), 59% (C5) and 124%(C8) can be achieved.

Overall, the remote array in combination with the dedicated local Rx arrays has demonstrated superior SNR performance.

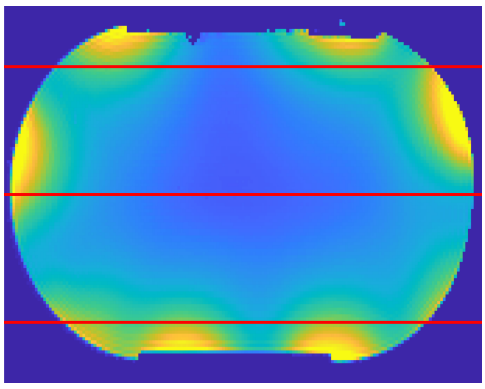

Figure 37: Positions of the SNR profile plots marked with a red line exemplarily shown on C2, the 8Tx8Rx array from DKFZ.

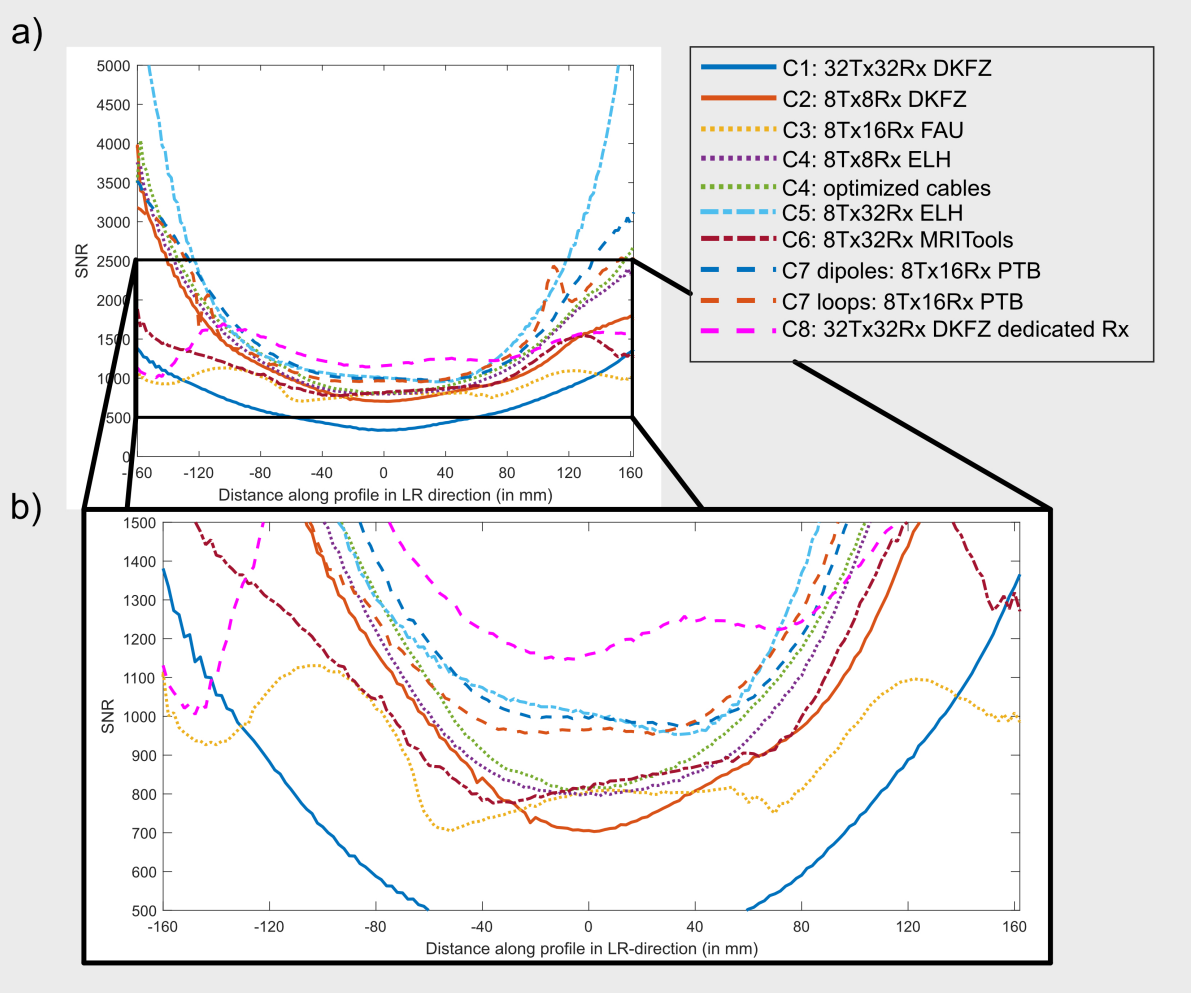

Figure 38: a) SNR profiles for all coil configurations along the center in lr-direction and b) a zoomed version.

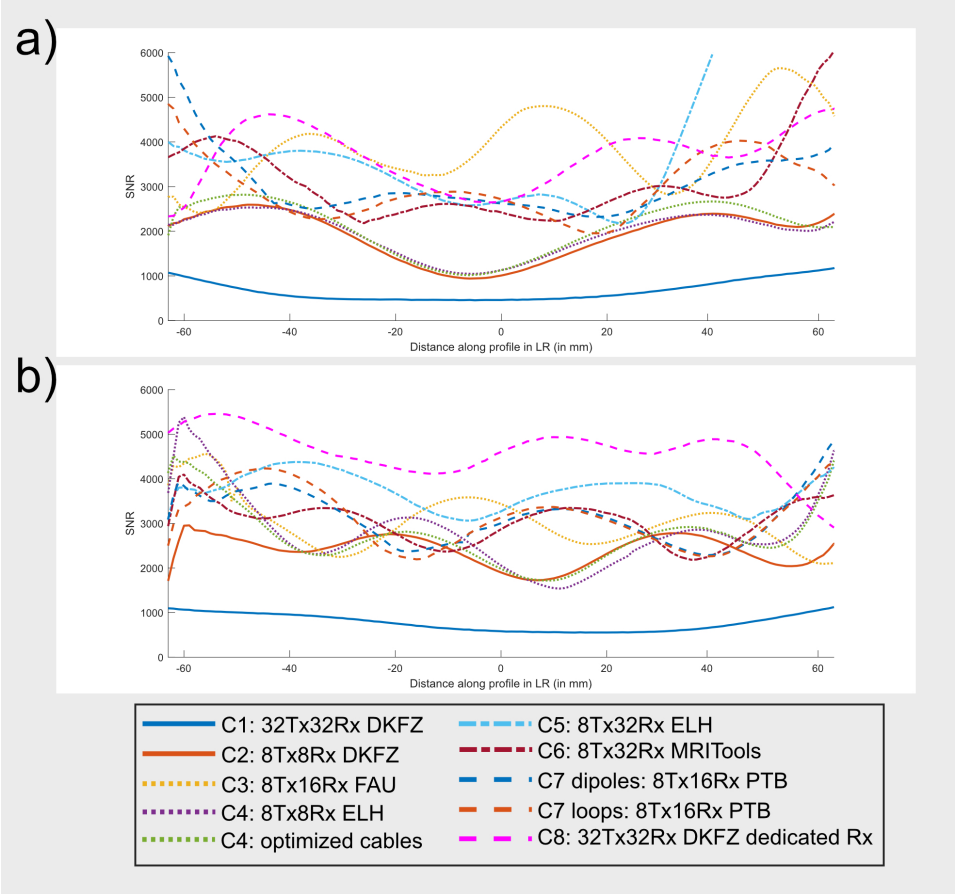

Figure 39: a) SNR profiles for all coil configurations along the top line, 2 cm under the top of the phantom in lr-direction and b) SNR profiles for all coil configurations along the bottom line, 2 cm above the bottom of the phantom in lr-direction.

4.1.2.2 Noise correlation matrices

Table 13 summarizes the mean and max noise correlation coefficients of the off-diagonal entries. For C7 the noise correlation is calculated from the B1R maps using the measurements acquired with the dipoles as transmit. Figure 40 displays the noise correlation matrices for all coils, representing the coupling between channels. All coils showed mean noise correlation coefficients of less than 0.17 (17% correlation), except C7, which achieved a correlation of 32% between the elements.

Table 13: Mean and max noise correlation values calculated from all off-diagonal matrix elements.

	C1	C2	C3	C4	C4*	C5	C6	C7	C8
mean	0.12	0.15	0.13	0.17	0.17	0.11	0.09	0.32	0.06
max	0.49	0.26	0.47	0.32	0.30	0.91	0.59	0.90	0.68

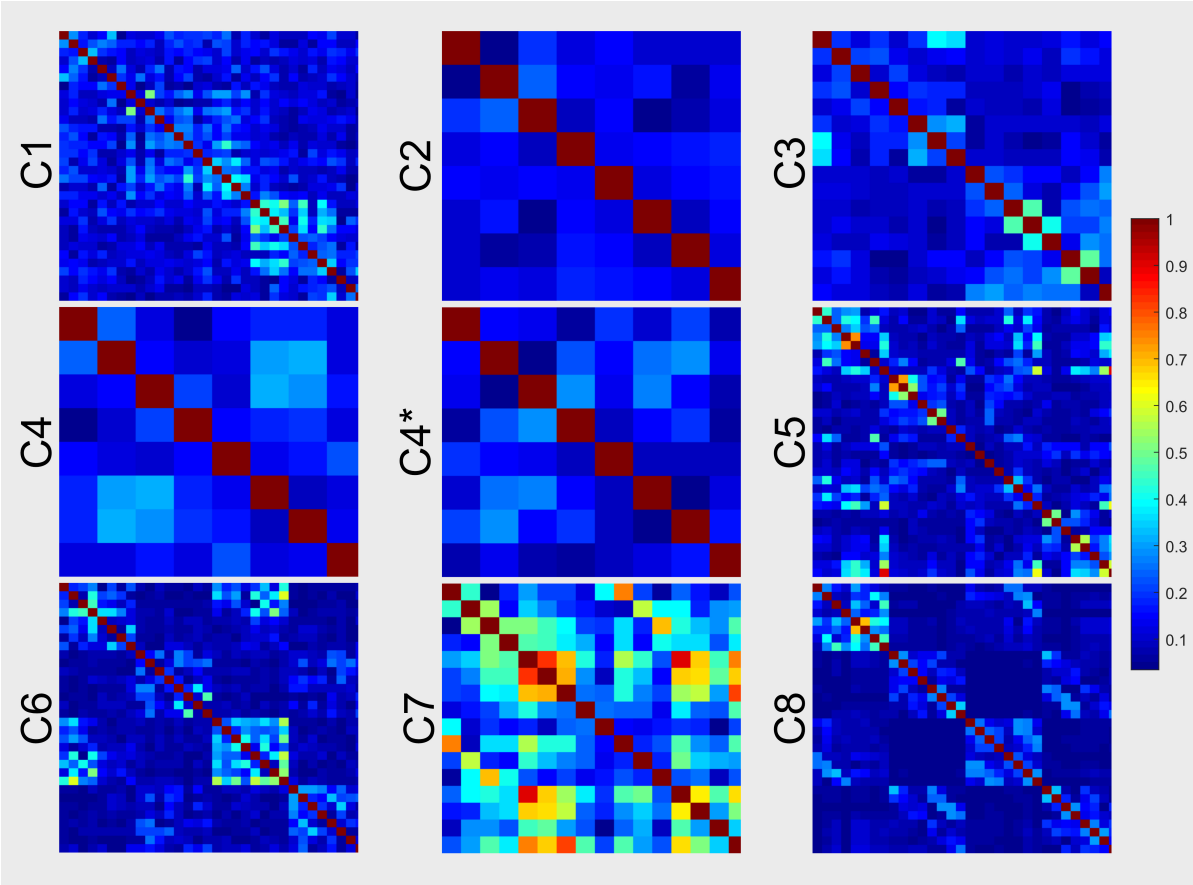

Figure 40: Noise correlation matrices for all coils. C1: 32Tx32Rx DKFZ, C2: 8Tx8Rx DKFZ, C3: 8Tx16Rx FAU, C4: 8Tx8Rx ELH, C4*: 8Tx8Rx ELH using the new cables connecting the elements with the switch box, C5: 8Tx32Rx ELH, C6: 8Tx32Rx PTB, MRITools, C7 dipoles: 8Tx16Rx PTB using dipoles as transmit, C7 loops: 8Tx16Rx PTB using loops for transmit, C8: 32Tx32Rx with dedicated local Rx array.

4.1.2.3 G-factor

Figure 41 presents the g-factor maps for all arrays, comparing acceleration factors from R=2 to R=5 with undersampling in either the ap- or lr-direction for the isocenter transversal slice. Corresponding mean and maximum g-factors are listed in table 14.
In general, all coils exhibited lower mean and maximum g-factors for higher acceleration factors in lr-direction than in ap-direction. On average, the maximum g-factors in ap-direction were 45% higher for R=3, 185% higher for R=4, and 312% higher for R=5 compared to lr-direction. For R=2, similar maximum g-factors are observed in both direction. Overall, the range of maximum g-factor values spanned from 1.14 to 19.61 in the ap-direction and from 1.09 to 7.57 in the lr-direction.

Lr-direction:
On average, coils with 8 Rx channels generally exhibited higher g-factor values than those with 16 or 32 Rx channels. For example, C2 achieved a maximum g-factor of 1.75 for R=3, while C7 (with 16 Rx channels) obtained a maximum g-factor of 1.15. However, C3, which also features 16 Rx channels, performed worse than 8-channel coils for acceleration factors up to R=3. For instance, C3 reached a maximum g-factor of 2.16 for R=3 in the lr-direction, whereas C4 achieved a maximum value of 1.67 for the same acceleration.
C7 with 16 Rx channels obtains lower g-factor values than C5 with 32 Rx channels for all acceleration factors in lr-direction. For example, C7 achieved a maximum g-factor of 1.15 for R=3, whereas C5 achieved a maximum g-factor of 1.75.
Despite featuring both 32 Rx channels, C6 achieved lower maximal g-factor values for all accelerations compared to C5.
The remote array (C1) performed similarly to the local 32-channel arrays for R=2 but is outperformed at higher acceleration factors. For instance, C1 reached a maximum g-factor value of 2.36 for R=4, whereas C6 achieved a maximum g-factor of 1.24.
The dedicated local 32-channel array (C8) reached higher maximum g-factor values for all acceleration factors than C7, despite having 16 more Rx elements, due to its elements being more distributed in the hf-direction.

Ap-direction:
Similar to acceleration in lr-direction, 8-channel coils exhibited higher g-factor values for accelerations in ap-direction compared to 16- or 32-channel coils. For example, C4* reached a maximum g-factor of 7.22 for R=4 in ap-direction, whereas C7 (16 Rx chan-

nels) achieved a maximum value of 2.32 for the same acceleration.
Comparing the g-factor maps for coils using 16 Rx channels, C7 achieved lower mean and maximum g-factor values in ap-direction for all acceleration factors compared to C3. For instance, C7 had a maximum g-factor of 2.04, while C3 achieved a value of 2.75 for R=3. Additionally, C7 performed similarly to the coils with 32 Rx channels in the ap-direction; for instance, at R=3, the mean/max g-factor was 1.16/2.04 for C7 and 1.14/1.95 for C5.
C5 achieved the lowest mean g-factor values for all acceleration factors in the ap-direction. C8, despite having 16 more Rx elements than C7, achieved higher g-factor values for all acceleration factors and higher g-factor values than C5/C6 (which also have 32 Rx elements), due to the greater distribution of its elements in the hf-direction.

Overall, a higher number of Rx elements enabled higher acceleration factors. Among all coil configurations, C6 consistently achieved the lowest mean and maximum g-factor values across all accelerations.

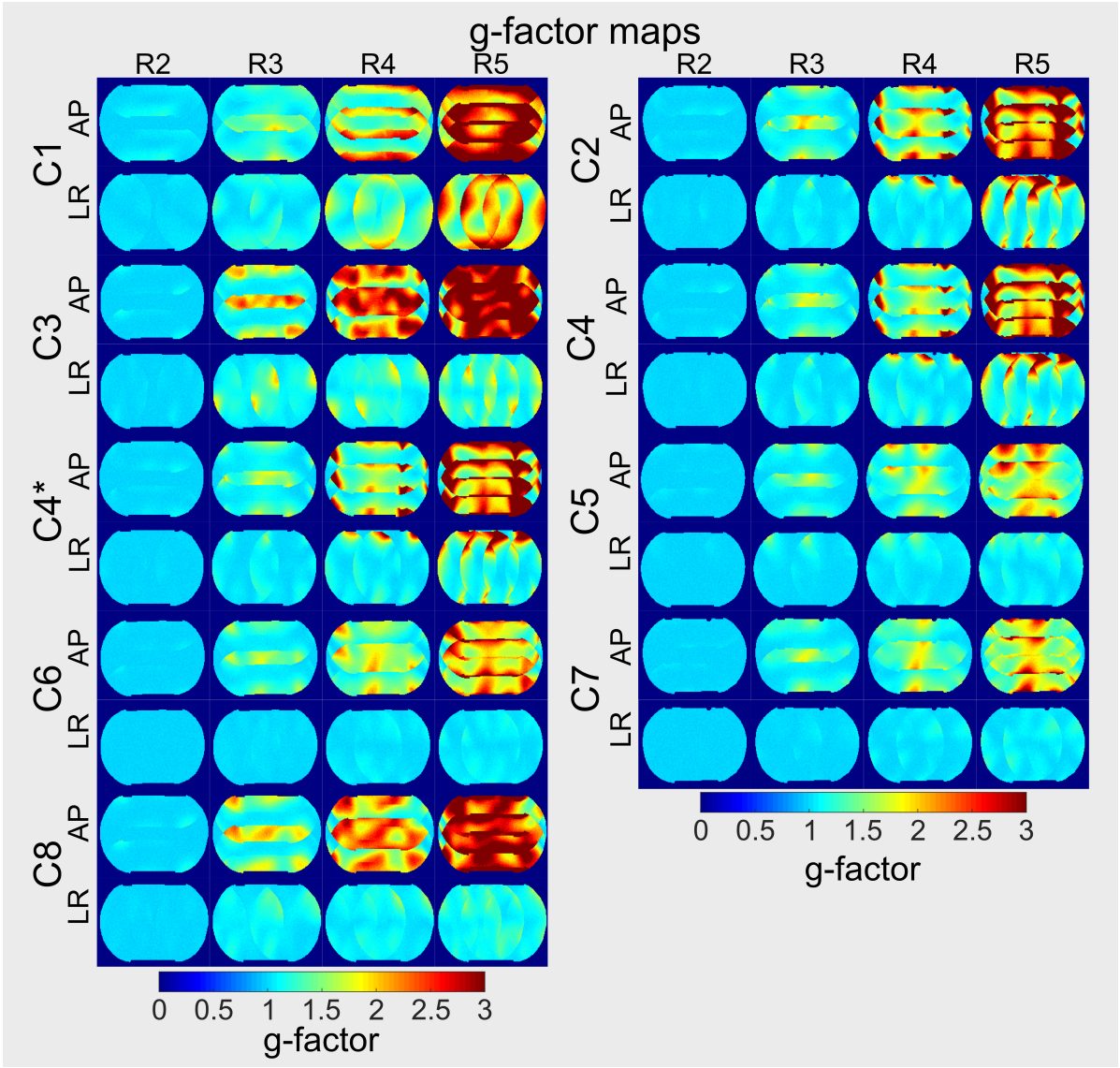

Figure 41: G-factor maps for acceleration between R=2 and R=5 for all coils using the undersampling patterns of 2D SENSE for acceleration in AP-direction (top row) and lr-direction (bottom row). C1: 32Tx32Rx DKFZ, C2: 8Tx8Rx DKFZ, C3: 8Tx16Rx FAU, C4: 8Tx8Rx ELH, C4*: 8Tx8Rx ELH using the new cables connecting the elements with the switch box, C5: 8Tx32Rx ELH, C6: 8Tx32Rx PTB, MRITools, C7 dipoles: 8Tx16Rx PTB using dipoles as transmit, C7 loops: 8Tx16Rx PTB using loops for transmit, C8: 32Tx32Rx with dedicated local Rx array.

Table 14: Mean and max g-factors for all coil configurations and acceleration factors of R=2 to R=5 in ap-direction and lr-direction. Lowest g-factors for each acceleration are marked with green, the highest g-factors with red.

	AP-direction (mean/max)				LR-direction (mean/max)			
	R=2	R=3	R=4	R=5	R=2	R=3	R=4	R=5
C1	1.04/1.31	1.23/2.22	1.65/3.77	3.22/8.45	1.02/1.14	1.12/1.48	1.37/2.36	1.95/4.01
C2	1.02/1.20	1.23/2.34	1.63/8.05	3.05/19.61	1.01/1.13	1.05/1.75	1.14/3.81	1.52/7.57
C3	1.01/1.28	1.41/2.75	2.18/3.75	3.26/15.28	1.01/1.13	1.19/2.16	1.22/2.04	1.30/2.38
C4	1.01/1.23	1.19/2.22	1.54/7.34	2.91/13.39	1.01/1.10	1.06/1.67	1.16/3.58	1.43/6.55
C4*	1.02/1.22	1.20/2.30	1.57/7.22	2.89/12.98	1.01/1.11	1.07/1.71	1.56/3.56	1.44/5.86
C5	1.01/1.14	1.14/1.95	1.32/2.46	1.68/3.56	1.00/1.11	1.05/1.75	1.07/1.70	1.10/1.92
C6	1.01/1.14	1.19/1.90	1.47/2.51	1.95/4.11	1.00/1.09	1.02/1.12	1.04/1.24	1.06/1.32
C7	1.01/1.12	1.16/2.04	1.33/2.32	1.69/3.74	1.00/1.09	1.01/1.15	1.04/1.32	1.08/1.40
C8	1.02/1.33	1.36/2.53	1.91/3.06	2.86/8.60	1.01/1.12	1.10/1.54	1.11/1.74	1.17/1.71

4.2 Validation of the RF pulse optimization method and the modified sequences

Phantom measurements are conducted to validate the k_T-point optimization method and the modified sequences. The measurements and corresponding sequence parameter are described in section 3.7.3.
The reconstructed relative B_1^+ magnitude maps of all 32 Tx-channels of the center slice, the respective ROI used for pulse optimization and the corresponding phases of all channels relative to channel one are shown in figure 42.

Figure 43 shows the predicted FA distribution using the zero-phase shim and two and three k_T-points and the corresponding acquired and reconstructed low FA acquisitions of the 3D k_T-point sequence for the center slice (receive profile not removed). The FA dropout within the ROI is clearly visible in the zero-phase shim in both prediction and measurement at the same position. Using two and three k_T-points the FA dropout within the ROI is removed and a homogeneous excitation can be achieved, visible in the predictions and corresponding GRE acquisitions. For zero-phase shim, a CV of 31.3% is achieved, which is improved to 3.5% using two k_T-points and 2.8% for three k_T-points. For both k_T-point optimizations a dropout can be found outside of the ROI in both, resulting FA predictions and the signal magnitudes of the low FA acquisitions at the same position, validating the predictions and thus, the optimization method. As the receive profile is not removed, residual signal intensity variation within the ROI in the GRE acquisitions still remained.

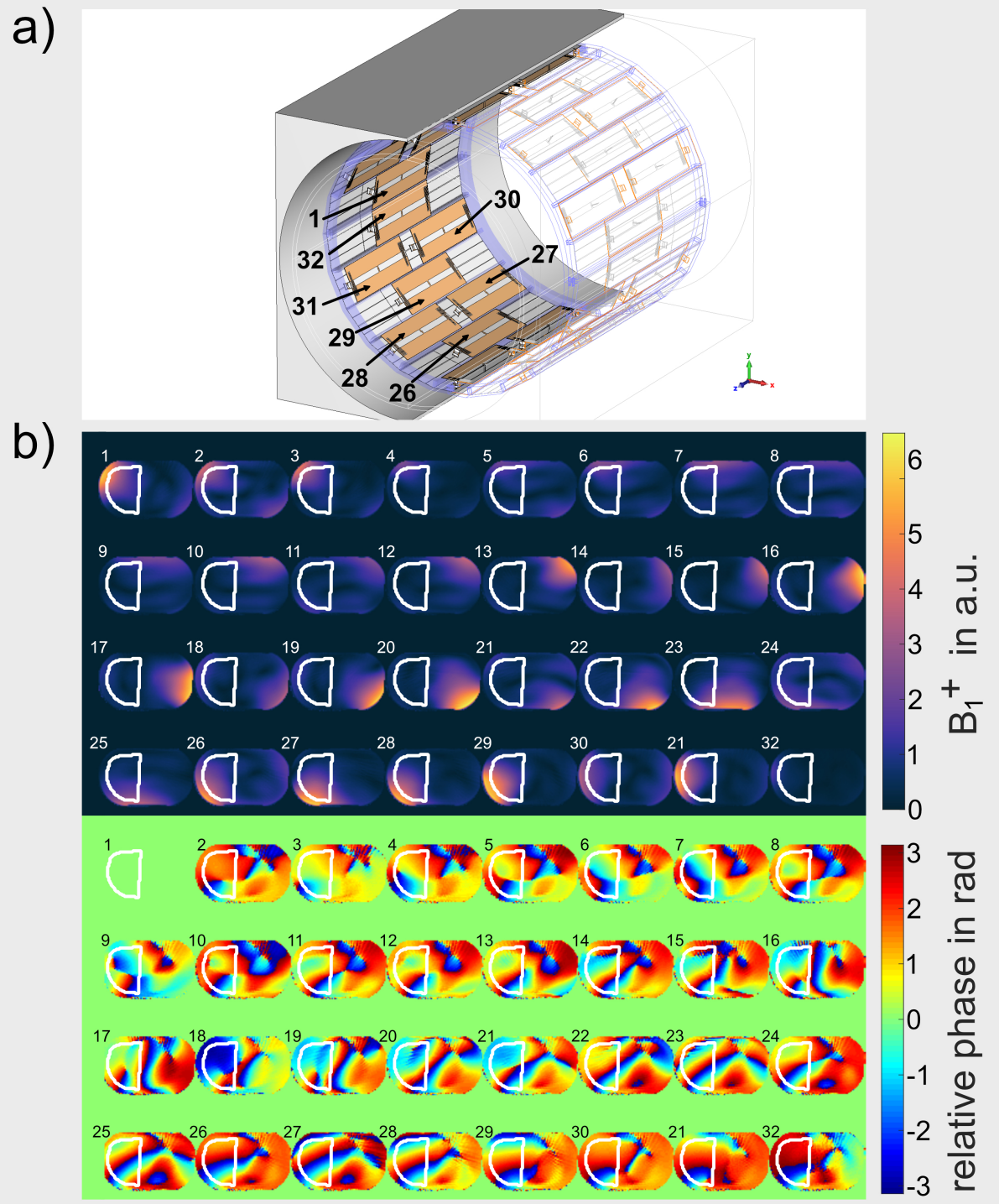

Figure 42: a) Explosion plot of the remote 32-channel whole body coil array to depict the channel locations. b) Relative B_1^+ magnitude (top) and phase maps (bottom) of Tx channels 1 to 32 with the respective ROI marked in white, which is used for pulse optimization. The maps are acquired of the center slice of the phantom.

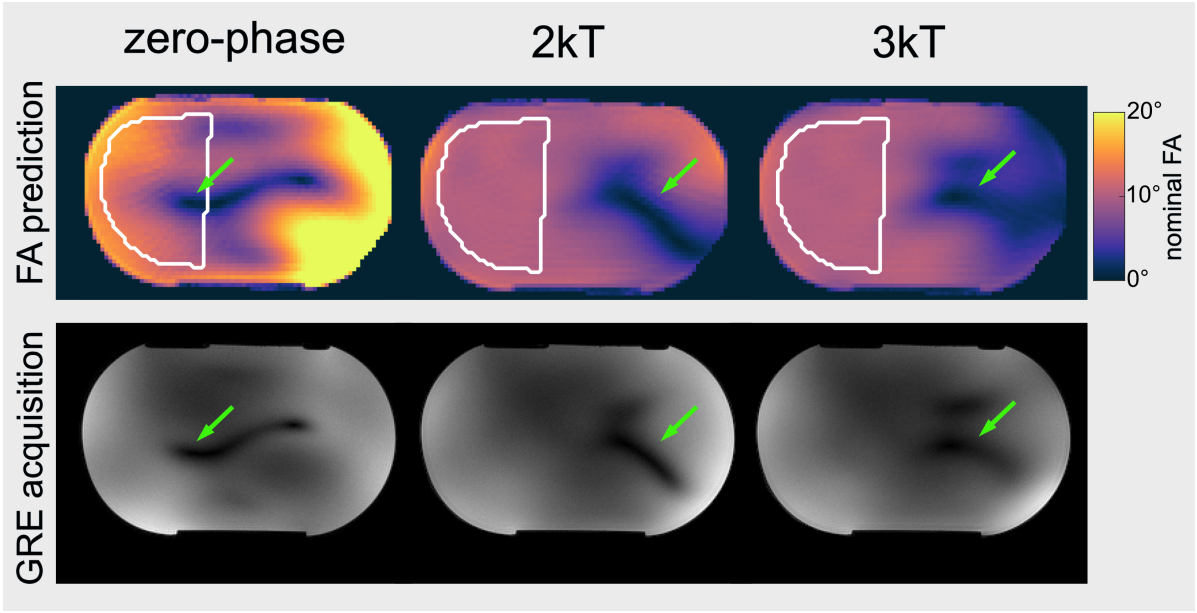

Figure 43: FA predictions and corresponding low FA 3D GRE acquisitions for zero-phase shim and two and three k_T-points. The FA dropouts are marked in both FA prediction and GRE acquisition with a green arrow.

4.3 *In-vivo* studies

4.3.1 Investigation of homogeneous liver excitation using static and dynamic pTx

The following section has been summarized in a research paper that is currently under revision in *NMR in Biomedicine*.

Figure 44 shows relative channel-wise B_1^+ magnitude and phase maps in combination with the respective ROI used for pulse optimization of one representative subject in an example transversal slice through the liver.

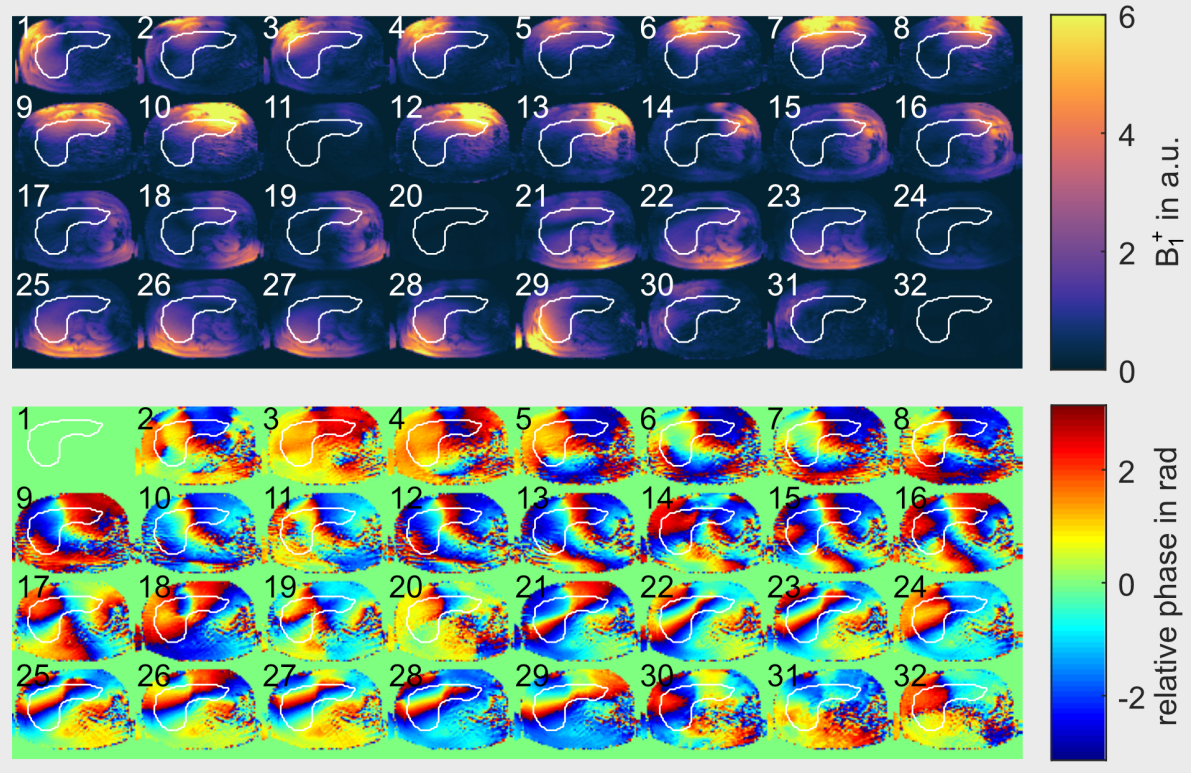

Figure 44: Relative channel-wise B_1^+ a) magnitude and b) phase maps of one representative subject in an example slice through the liver with the respective ROI marked in white, which is used for pulse optimization.

Residual motion artifacts of the RPE-GRE sequence are visible in the magnitude images (i.e. channel 10 in the center of the subject). The relative phases are well-defined across all channels within the ROI, and the noise level is low within this ROI. Instabilities of channels 11, 20, 24, and 32 can be seen in the magnitude maps as the signal intensity is very low (close to zero) compared to the other channels.

4.3.1.1 Analysis

Analysis with all channels:

L-curve plots obtained after phase shimming and with dynamic pTx pulses using up to six kT-points are shown in figure 45 for the five subjects and all Tx channels enabled. Phase shimming yielded CV values below 15% for four subjects, which indicates FA

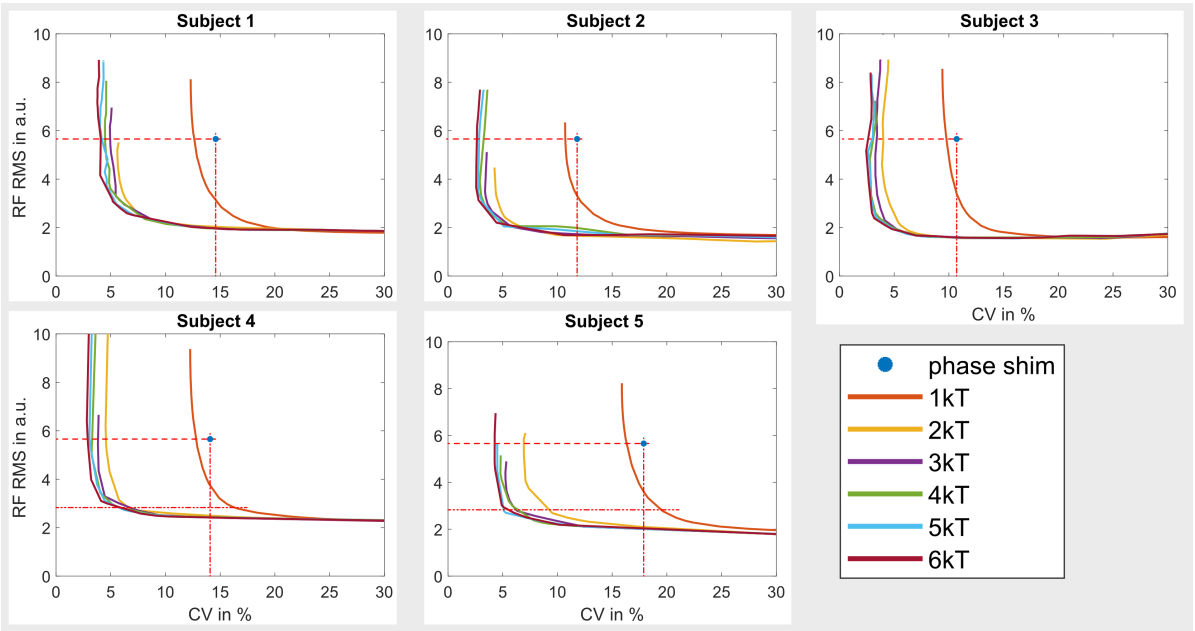

Figure 45: RMS RF voltage vs. FA CV for all subjects for one to 6 k_T-point pTx pulses. Horizontal dashed lines mark the same RF RMS voltage as for phase shimming and the vertical dotted line the same CV as for phase shimming. For Subject 4 and 5 the second horizontal dotted line marks half of the RF RMS voltage as for phase shimming.

distributions without dropouts within the ROI, as recently reported for the heart volume at 7 T [105] and as confirmed by figure 46a) for Subject 4. For Subject 5 with the largest body dimension in AP-direction, a CV value of 17.9% is achieved.

With one k_T-point (magnitude and phase shimming) and the same RF power as for phase shimming, the CV can be improved just by a factor of 1.1, and only a minor improvement is observed in the resulting B_1^+ predictions (figure 46a). Applying two k_T-points resulted in a reduction in CV by a factor ranging from 2.6 to 3.1 versus phase shimming and in FA prediction maps with only minor remaining FA variations in any subject for the same RF voltage RMS as for phase shimming. A further but less pronounced decrease in CV, which is also qualitatively visible in the FA predictions in figure

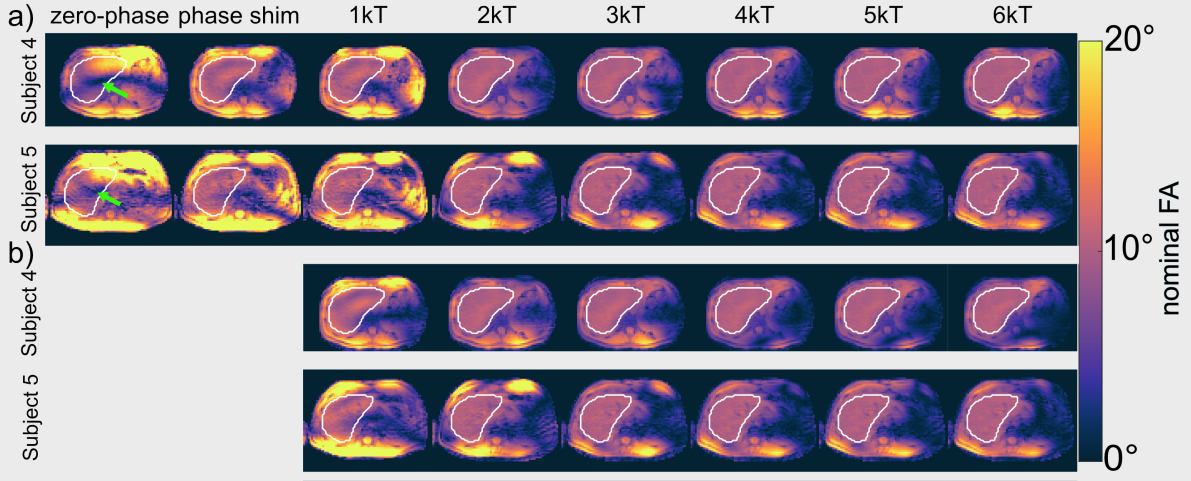

Figure 46: FA predictions for an example transversal slice through the liver for Subject 4 and 5 with a) the same RF voltage as phase shimming and b) half of the RMS voltage as for phase shimming using zero-phase, phase shim and one to six k_T-points. FA dropouts marked with a green arrow in the zero-phase shim.

46a), is obtained when the number of k_T-points is further increased while maintaining the same RF voltage RMS.

By comparing the different numbers of k_T-points with half of the RF voltage RMS as for phase shimming (lower horizontal dotted line in figure 45), the more optimal tradeoff between power and homogeneity, i.e. a value close to the corner of the L-curve, can be obtained. In this case, the CV for two k_T-points is reduced by a factor of 2.7 for Subject 4 and by a factor of 2.4 for Subject 5 in comparison to one k_T-point. Again, the homogeneity is only marginally increased by increasing the number of k_T-points, as is qualitatively visible in figure 46b).
As an alternative to reducing the CV, the RF voltage RMS can be reduced by a factor ranging from 1.5 to 1.8 by magnitude and phase shimming and by a factor ranging from 2.4 to 3.3 for two k_T-points vs. phase shimming for the same CV as for phase shimming. In this case, increasing the number of k_T-points did not reduce the RF voltage RMS further. For all five subjects, the choice of two to three k_T-points resulted in a good tradeoff between excitation fidelity and RF power (bend of the L-curve) as neither the CV nor the RF voltage RMS decreased significantly with a further increase in the number of k_T-points.

Analysis and comparison of 8, 16, 20 and 28 Tx channels:

Figure 47a) compares the L-curves obtained with 8, 16, 20 and all 28 Tx channels for three subjects with low (Subject 1: 19.5 kg m^{-2}), normal (Subject 3: 21.9 kg m^{-2}), and high (Subject 2: 26.2 kg m^{-2}) BMI.

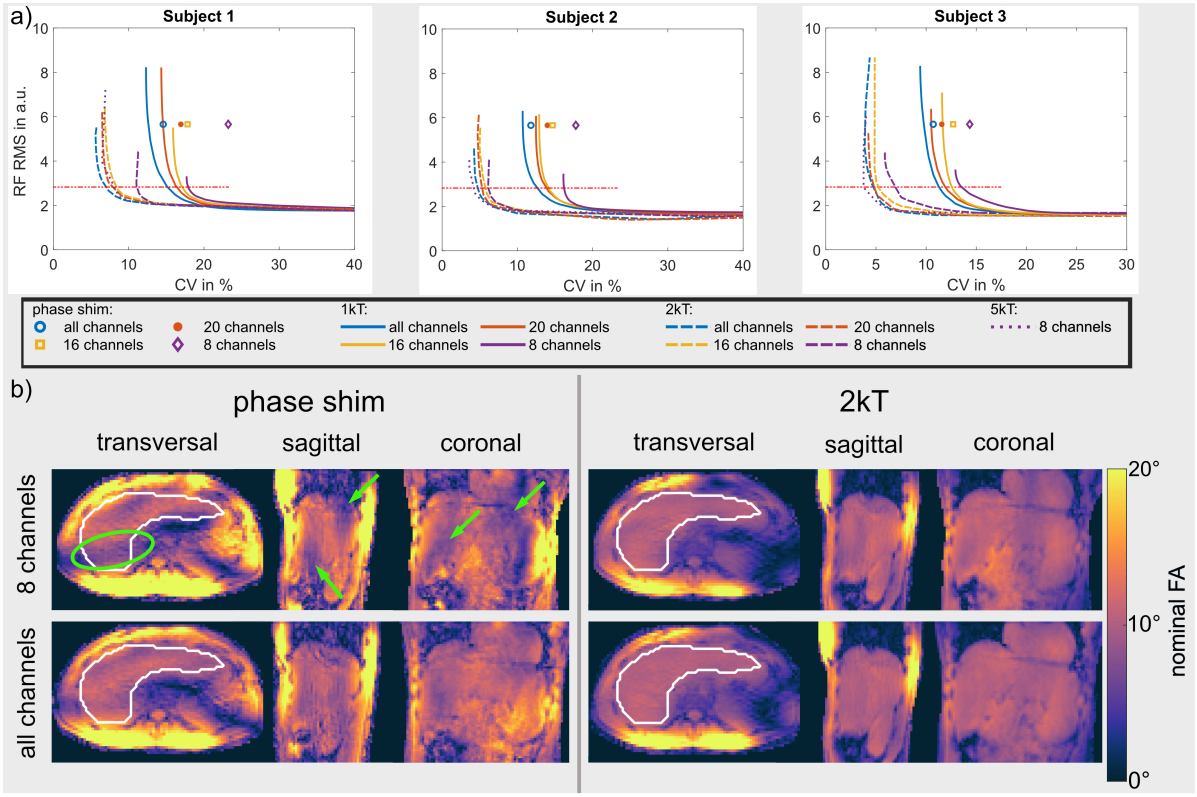

Figure 47: a) L-curves for Subjects 1, 2 and 3 for 8, 16 and 28 channels. The horizontal dotted line marks half of the RF voltage as for phase shimming. b) FA predictions for Subject 1 comparing 8 and all 28 available channels with phase shim and two k_T-points. Green arrows and circles mark FA dropouts and variations with 8 channels; these areas show improved homogeneity with 28 channels.

The figure shows that the CV decreased moderately as the number of channels increase using 16 Tx channels instead of 8 Tx channels. However, the extent of the improvement is dependent on the number of k_T-points used or if phase shimming is used. In this case, the CV can be reduced by a factor ranging from 1.13 to 1.3 for phase shimming across all subjects. For one k_T-point (two k_T-points) the CV can be reduced across all subjects by a factor ranging from 1.05 to 1.13 (1.06 to 1.30) for the same channel increase and for half of the RF RMS voltage as for phase shimming, which is the more optimal tradeoff

between power and homogeneity, i.e. a value close to the corner of the L-curve.
Increasing the number of Tx channels from 16 to 20, representing an 25% increase, the figure indicates that the CV continued to decrease, but the improvement is less pronounced than the reduction from 8 to 16 Tx channels. In the context of phase shimming, the CV is further reduced by a factor ranging from 1.01 to 1.06 across all subjects. For one k_T-point (two k_T-points) the CV can be additionally reduced across all subjects by a factor ranging from 1.01 to 1.06 (1.07 to 1.14) for 20 Tx channels in comparison to 16 Tx channels and for half the RF RMS voltage as used for phase shimming.
Furthermore, the figure illustrates that increasing the number of Tx channels by 75%, from 16 to 28 elements, results in a decrease in CV similar to the reduction observed when going from 8 to 16 channels. Using phase shimming, the CV can be reduced by a factor ranging from 1.18 to 1.24 across the three subjects and by a factor ranging from 1.12 to 1.16 (1.16 to 1.26) using one k_T-point (two k_T-points) and half of the RF RMS voltage as for phase shimming.
As expected, comparing 8 Tx channels to 28 Tx channels gave the largest improvement: The CV can be reduced by a factor ranging from 1.24 to 1.59 for phase shimming across all subjects and by a factor ranging from 1.19 to 1.33 for one k_T-point and 1.33 to 1.52 for two k_T-points using half of the RF RMS voltage as for phase shimming. Furthermore, phase shimming with 32 channels yielded lower CV values than one k_T-point for 8 and 16 channels.

The largest increase can be seen in Subject 1, where five k_T-points are necessary for 8 Tx channels to achieve similar CV values as two k_T-points with 16, 20 or all channels.

Figure 47b) shows the corresponding FA predictions achieved with phase shimming and two k_T-points using all Tx channels or 8 Tx channels. The improved homogeneity using all channels in comparison to 8 is qualitatively visible for both, phase shimming and two k_T-points. Furthermore, phase shimming with 8 Tx channels resulted in a CV of 23.2%, with an FA dropout observed in the ROI, which is highlighted by a green arrow/ellipse. This dropout is eliminated by using all Tx channels.

Experimental Validation:

Figure 48 shows the *in-vivo* GRE images of a representative transversal slice and two sagittal slices through the liver using all available channels for Subject 2. The signal magnitudes of these small FA acquisitions matched their corresponding predictions (re-

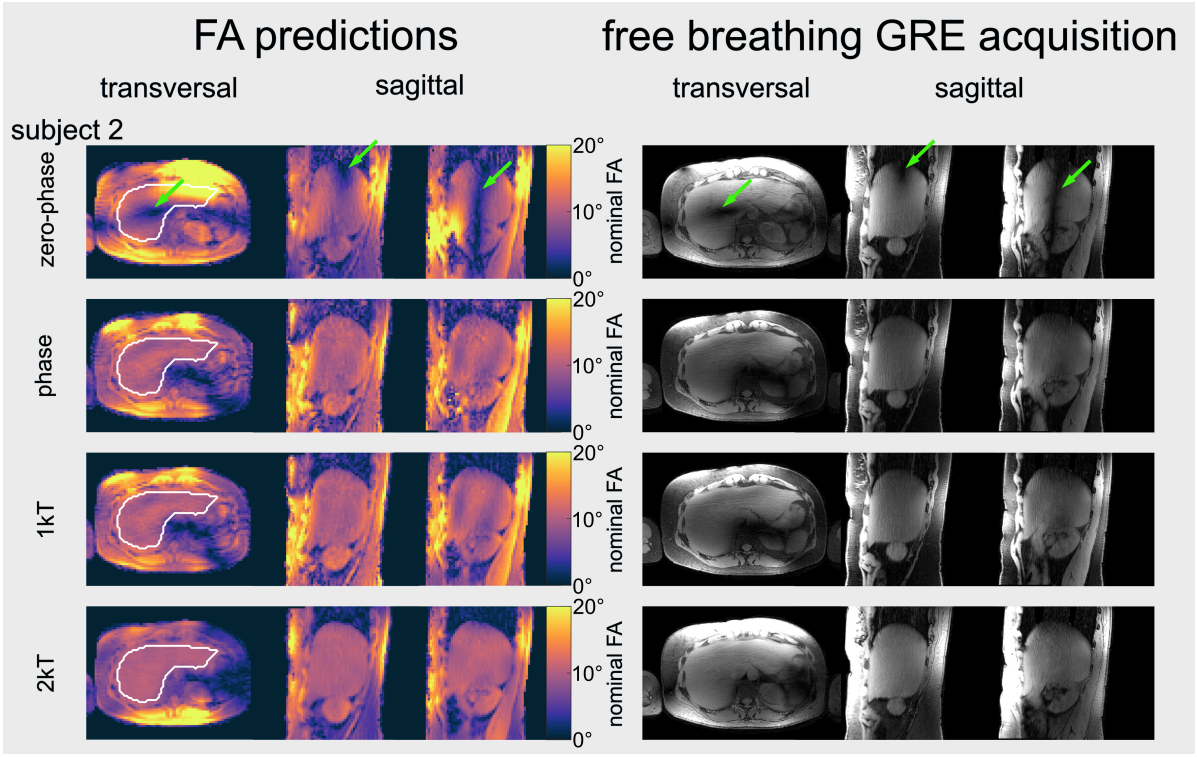

Figure 48: FA predictions and corresponding magnitude images of an example transversal slice and two example sagittal slices through the liver of Subject 2 for zero-phase shim, phase shim, and for one and two k_T-point-points. The FA dropout in the zero-phase shim is marked with a green arrow. The receive profile is not removed.

ceive profile not removed). This beccomes apparent by the same position of the FA dropouts in both predictions and GRE acquisitions. For the zero-phase shim, the FA dropouts are clearly visible within the ROI. These dropouts are removed using phase shimming or one k_T-point. However, FA variations are still visible. Therefore, the FA homogeneity can be improved further by using two k_T-points, as it becomes apparent in both the FA predictions and the corresponding GRE scans in the transversal orientation. Figure 49 shows the GRE images for the other subjects in transversal and sagittal orientation and with zero-phase shim, phase shim, and for one and two k_T-points. The FA dropouts in the zero-phase shim are marked with a red arrow. For all subjects no dropouts are left in the case of phase shimming and one k_T-point provided a minimal improvement in homogeneity compared to phase shimming. However, FA variations are still visible, which are removed using two k_T-points.

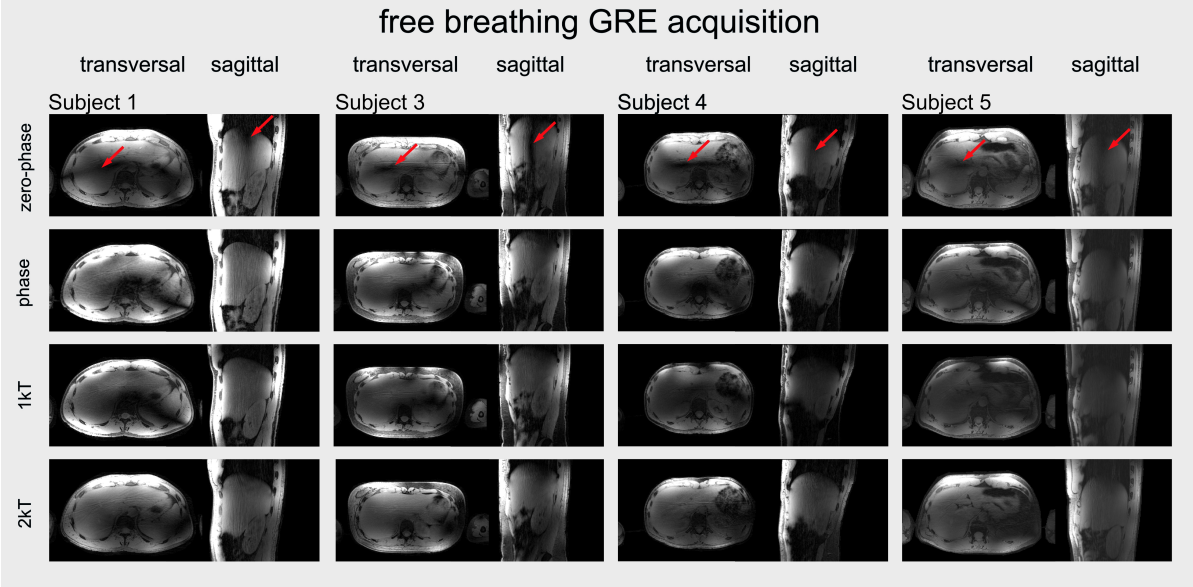

Figure 49: GRE acquisitions for transversal and sagittal orientations of Subjects 1, 3, 4 and 5 for zero-phase shim, phase shim, and one and two k_T-points. The FA dropout for the zero-phase shim is marked with a red arrow in all subjects. Note that the receive profile is not removed. Also, residual streak artifacts are visible that originate from the undersampling of the RPE.

Overall, the results demonstrated that using a remote 32 Tx channel whole-body coil array, sufficient FA homogeneity is achieved through phase shimming in all subjects. Additionally, employing two k_T-points provided a good tradeoff between power and FA homogeneity.

4.3.2 Investigation of homogeneous abdomen excitation using static and dynamic pTx

Figure 50 shows magnitude and phase of relative channel-wise B_1^+ maps in combination with the respective ROI used for pulse optimization of one representative subject in an example transversal slice through the abdomen.

Amplifiers of channels 19, 20, 25, 27 and 32 were not operational during the measurements, which can be seen in the magnitude images as the signal intensity is close to zero. It is visible in the phase maps, that higher noise levels are present within the ROI (i.e. channels 13 and 30). This becomes apparent by the five times lower signal magnitude in the abdomen for reference channel 1 in the regions opposite to the elements position

compared to the the signal magnitudes in the regions closer to the element location.

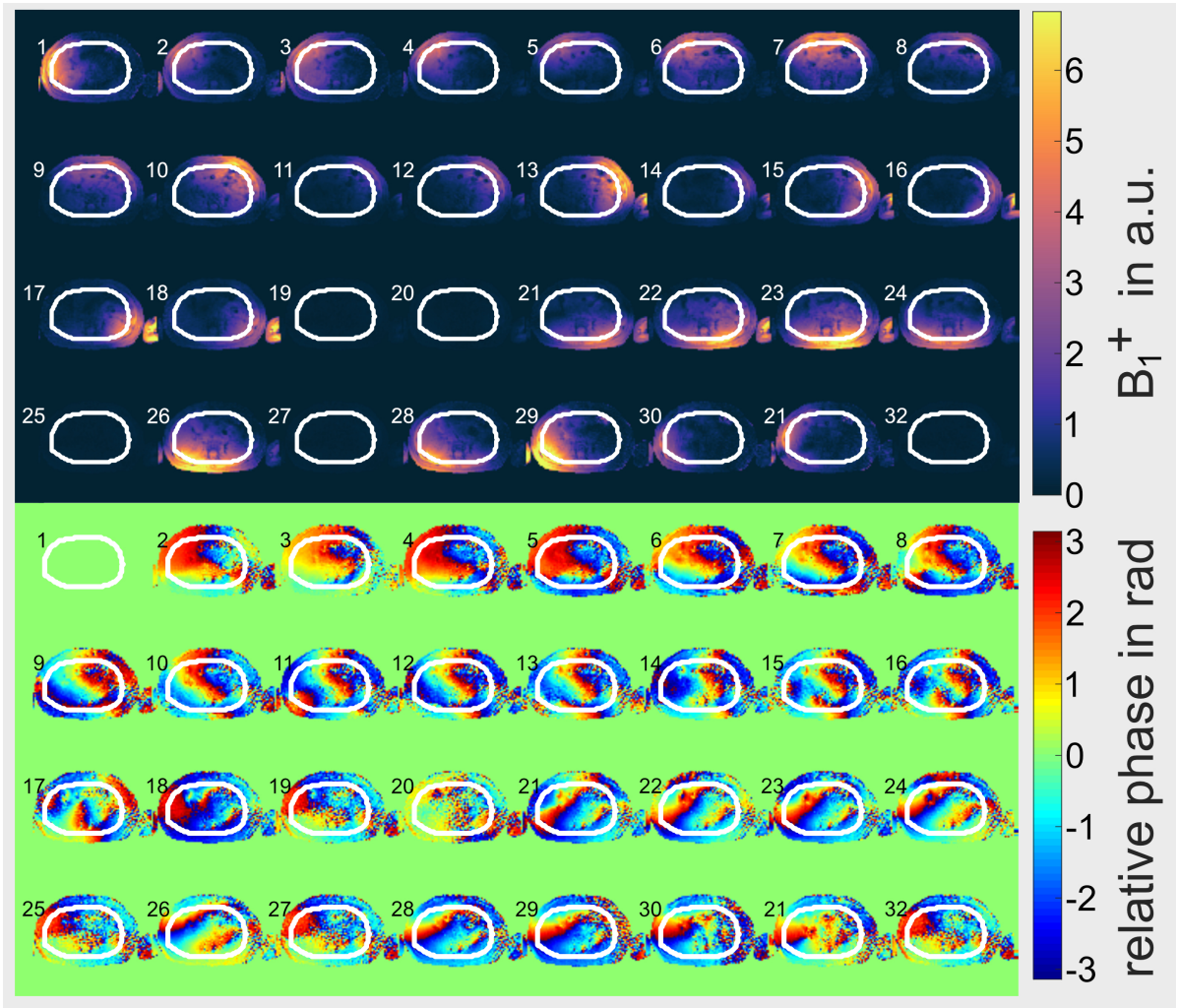

Figure 50: Relative channel-wise B_1^+ a) magnitude and b) phase maps of one representative subject (Subject 1) in an example slice through the abdomen with the respective ROI marked in white, which is used for pulse optimization.

Predicted FA maps of all subjects for zero-phase shim and one to five k_T-points for three example transversal slices throughout the entire FoV are shown in figure 51, 52 and 53. These FA predictions show, that applying only one k_T-point (i.e. phase/magnitude shimming) failed to homogeneously excite the whole abdomen as FA dropouts still remained within the ROI. With two k_T-points, no FA dropouts are observed in the ROI for all subjects. An acceptable visual homogeneity can be achieved for Subjects 1 and 2. For Subject 3, a larger FA variation as compared to Subject 1 or 2 can be seen in slice 52. Increasing the number of k_T-points further does not visibly increase the homo-

geneity. This can also be quantitatively seen by the CV, which is calculated in the ROI. For Subject 1/2/3, the CV can be reduced from 51.4%/48.4%/48.1% with zero-phase shim to 31.3%/32.8%/26.8% using two k_T-points. With a higher number of k_T-points the CV is only moderately improved for the three subjects to 30.8%/32.7%/26.4% for four k_T-points.

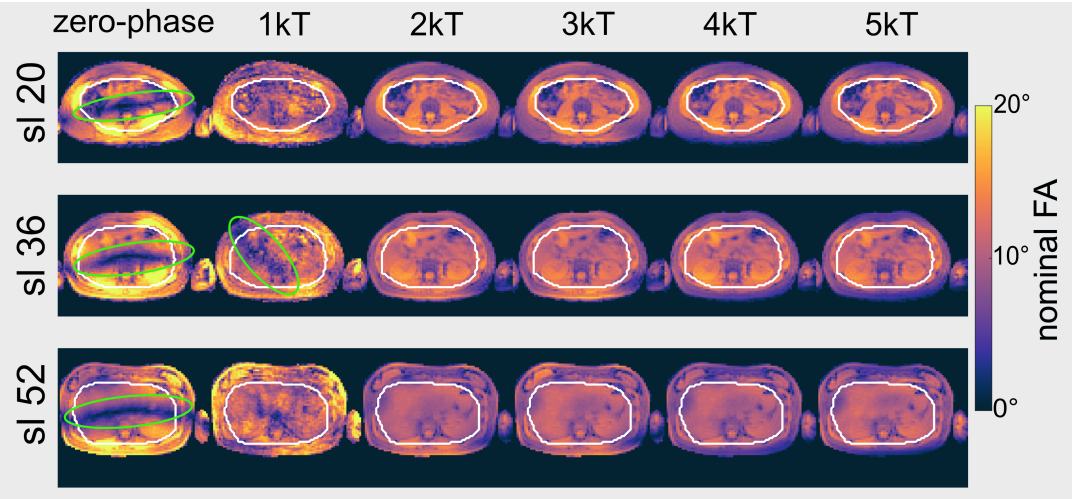

Figure 51: Predicted transversal FA maps for three example slices for Subject 1 using zero-phase shim and one to four k_T-points. FA dropouts for zero-phase shim are marked with a green ellipse.

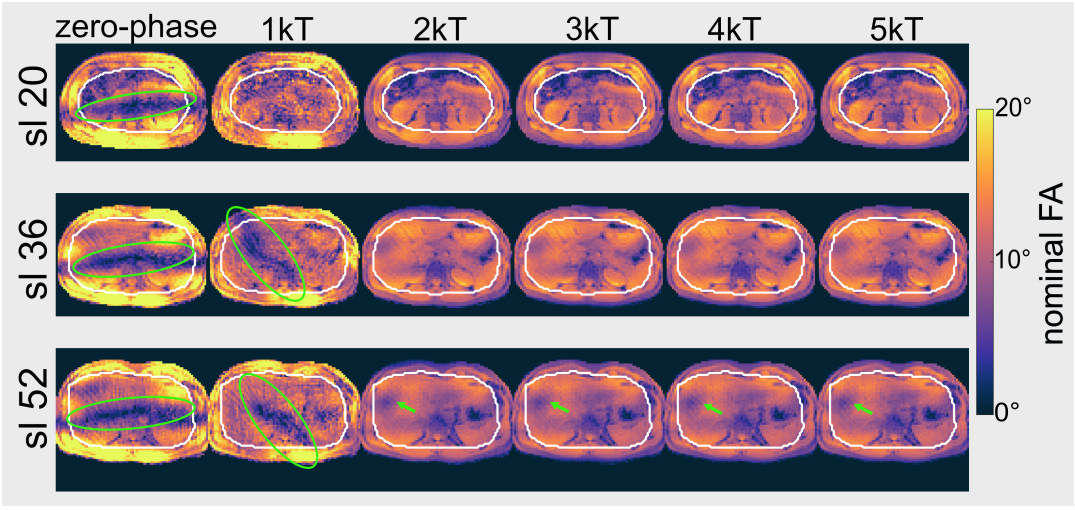

Figure 52: Predicted transversal FA maps for three example slices for Subject 2 using zero-phase shim and one to four k_T-points. FA dropouts for zero-phase shim and one k_T-point are marked with a green ellipse. Larger FA variation in slice 52 are marked with a green arrow.

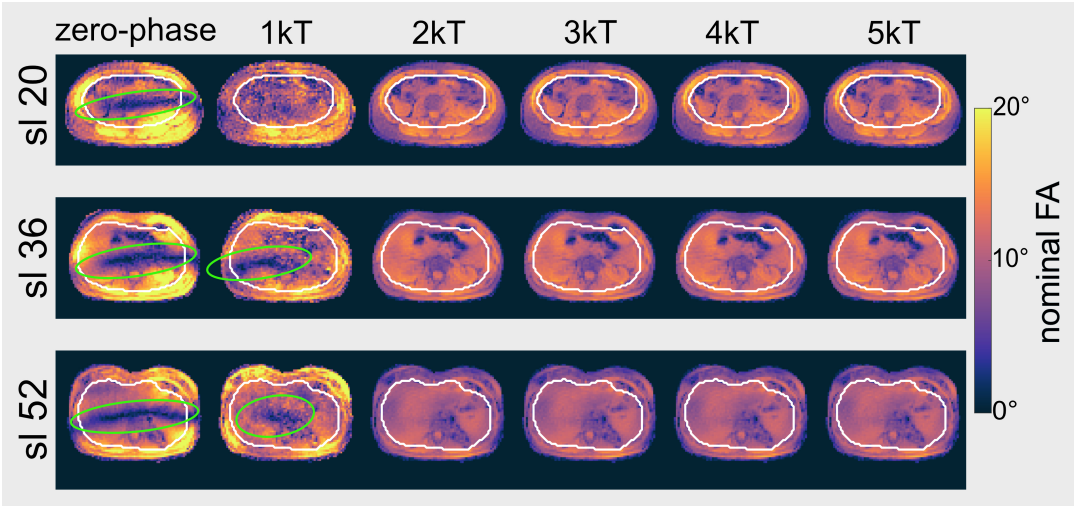

Figure 53: Predicted transversal FA maps for three example slices for Subject 3 using zero-phase shim and one to four k_T-points. FA dropouts for zero-phase shim and one k_T-point are marked with a green ellipse.

Figures 54 and 55 show GRE acquisitions (receive profile not removed) for Subject 1 and 2 in all orientations and the corresponding FA prediction for the transversal slice. The signal magnitudes of these small FA acquisitions match their corresponding predictions.

For both subjects, one k_T-point (i.e. phase/magnitude shimming) failed to homogeneously excite the whole abdomen which is visible in both the FA predictions and GRE acquisitions. There, a remaining FA dropout is visible in the transversal slice. With two k_T-points, no FA dropouts are observed within the abdomen in both the predictions and the GRE scans and a homogeneity of $CV = 31.3\%/32.8\%$ for Subject 1/Subject 2 can be achieved in the FA predictions.

In summary, the results demonstrated that whole abdomen shimming is feasible using a remote 32-channel whole-body coil array. Additionally, they reveal that only dynamic pTx, and not static pTx, is capable of achieving sufficient FA homogeneity.

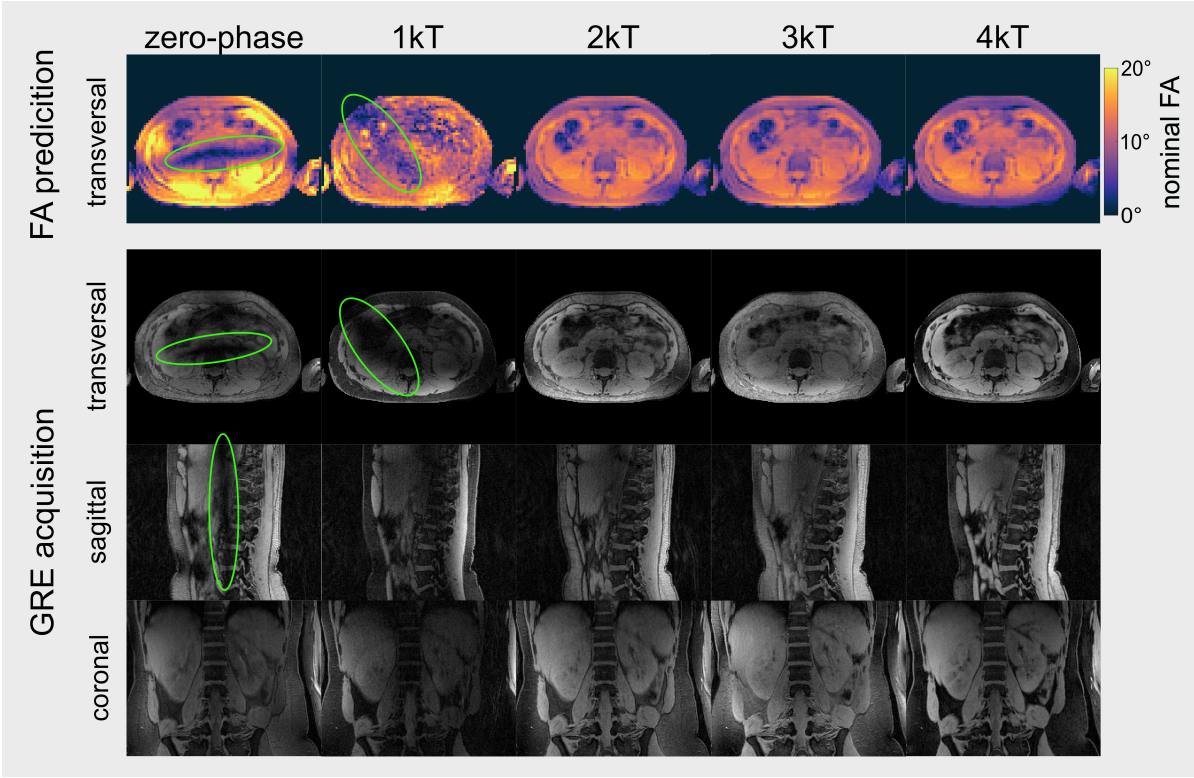

Figure 54: Predicted transversal FA maps and GRE acquisitions in all orientations of Subject 1. FA dropouts are marked in the zero-phase shim and for one k_T-point with a green ellipse.

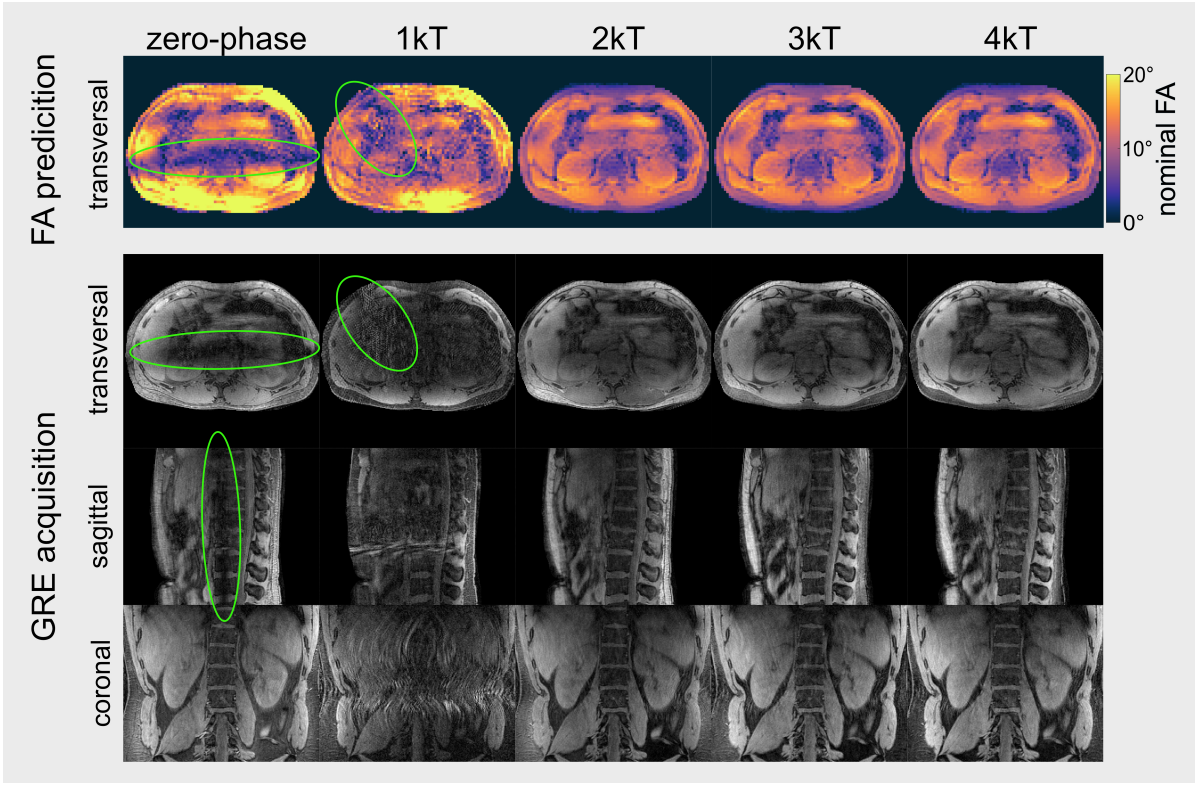

Figure 55: Predicted transversal FA maps and GRE acquisitions in all orientations of Subject 2. FA dropouts are marked in the zero-phase shim and for one k_T-point with a green ellipse.

5 Discussion

Various local multi-channel body coil arrays, featuring eight Tx channels, have been developed to enable pTx and address the challenges of FA variations in the human body at 7 T. More recently, a remote 32-channel coil array was developed. To evaluate the remote coil in comparison to existing local pTx body coils and to experimentally investigate its pTx capabilities through *in-vivo* measurements, this thesis was divided into two parts.

In the first part, the Tx and Rx performance of seven different existing local ^{1}H pTx coils for UHF body MRI from German sites and the remote 32-channel coil array, also in combination with a dedicated local Rx array, were quantitatively evaluated through phantom measurements. This comparison contextualized the remote coil relative to the local body coils. While the remote array exhibited lower B_1^+ efficiency at the phantom's center compared to local arrays, this limitation can be compensated by its four- or eight-fold higher available total RF power. Additionally, the remote array showed no substantial variation in the excitation profile along hf-direction making it a well-suited array for large field-of-excitation imaging. In terms of Rx performance, the remote array in combination with a dedicated local Rx array achieved the highest SNR values in the center of the phantom compared to the local pTx arrays.

The second part of this thesis experimentally investigated the pTx capabilities of the 32-channel remote coil array using *in-vivo* measurements. The first *in-vivo* study assessed its ability to achieve a homogeneous FA distribution across the liver, the largest internal organ, in all subjects. Static pTx yielded sufficient FA homogeneity, while two k_T-point pulses provided a good tradeoff between power and homogeneity. Furthermore, using all 32 Tx channels improved homogeneity compared to utilizing only eight channels for both, static and dynamic pTx. The second *in-vivo* study extended the excitation region to the entire abdomen. While static pTx failed to achieve uniform excitation, two k_T-point pulses obtained sufficient homogeneity across all subjects.

In the following, the methods and results concerning both the Tx and Rx performance of the eight different coils and the pTx capabilities of the remote 32-Tx-channel whole-body coil for large field-of-excitation imaging are discussed.

5.1 Comparison of various pTx RF body arrays for 7 T body imaging

All eight coils were evaluated using the same 7 T scanner, the same phantom, and the same measurement protocol. This ensured consistency and comparability. Different MRI scanners may have variations in hardware, such as gradients or amplifiers, which could introduce variations to the results. By employing the same scanner, any observed differences can be attributed to the coil designs rather than scanner-related factors. The same applies for different phantoms and measurement protocols. Differences in phantom properties or sequence parameters could introduce variability unrelated to the coil performance itself.

Rietsch et al. compared individual element types in simulations for their potential as remote 8-channel Tx coil, but did not asses them in comparison to their performance as local coils [107]. Furthermore, while most of the coils or element types were already evaluated individually [79, 81, 83, 86], a direct comparison between them has not yet been conducted through phantom measurements.

In addition, this study employed a new method for B_1^+ mapping [95], which enables highly accurate B_1^+ maps. Typically the AFI method is used for B_1^+ mapping, but the method is inaccurate for FA lower than 25°. Furthermore, the AFI method can produce inaccurate B_1^+ values in combination with the widely used PVP phantom [108]. However, PVP is still the prefered filling for body phantoms, due to its dielectric properties being similar to human tissue. Nevertheless, when combined with the AFI method, special attention must be given to potential interactions or inaccuracies that may arise [108].

The B1-MRF is highly accurate even for low FA, is not susceptible to T_1 and offers a high dynamic range [95]. Thus, very precise B_1^+ maps and values were achieved for all coils ensuring a highly accurate comparison.

This study was also subject to limitations. Different Tx/Rx switches were used for the coils, as it was not possible to connect all coils to the same switch. Variations in the performance of these switches could impact the results. Therefore, a future task will be to measure the attenuation and quantify the influence of different switches on the Tx and Rx performance.

All coils were placed in the exact same position. However, some variations remained

due to the scanner's alignment laser not being perfectly precise. The most significant misalignment was observed for the 8Tx8Rx coil from ELH (C4), which exhibited a shift of approximately 2 cm in the hf-direction between the anterior and posterior part of the coil. This shift was visible in Figure 33, where the excitation distribution in the sagittal slice appeared slightly displaced, towards the head on the anterior side and towards the feet on the posterior side. This misalignment may have contributed to a lower B_1^+ efficiency value in the center compared to other coils. However, since the excitation coverage in the hf-direction decreased by less than 2% within 2 cm around the maximum in the center, the impact on B_1^+ efficiency was minimal. Nevertheless, the alignment for the other coils was much more consistent.

Furthermore, only the center transversal slice was examined regarding SNR and acceleration potential. However, it would be valuable to consider additional transversal off-center slices, as well as sagittal and coronal slices, as these could provide more comprehensive insights into the Rx performance of the coils throughout the phantom. For example, sagittal and coronal slices would offer information about the SNR and acceleration potential of the coils in the hf-direction, while additional transversal slices could reveal the coils' behavior for larger FoV in hf-direction and for off-center slices. This would help assess the performance of the coils when scanning several regions or organs within the center of the coil but also off-center within one session, as well as their ability to investigate coronal and sagittal slices or even 3D volumes. In this context, coils with more Rx elements in the hf-direction might offer an advantage over coils with only one Rx element in that direction. Additionally, coils with larger off-center Rx performance would reduce preparation time, if the target region was not placed perfectly in the center.

The excitation performance of the coils in the hf-direction was evaluated using relative B_1^+ maps. However, this approach relies on the fast estimation technique by Van de Moortele et al. [91], which involves approximations that may introduce errors in determining the hf-excitation coverage. Therefore, an absolute 3D B_1^+ dataset, not based on the AFI method, would provide more accurate results. However, at the time of the study, a precise 3D B_1^+ mapping method was not yet available.

Additionally, only the magnitudes of the relative B_1^+ maps in hf-direction were examined. Although these magnitudes provide information about the hf-excitation coverage, they do not offer full insight into the pTx capabilities in hf-direction. Therefore, it would

be necessary to examine the phases of the relative channel-wise B_1^+ maps or of absolute channel-wise B_1^+ maps.

Despite these limitations, this comparison offered a valuable overview of the Tx and Rx performance of existing pTx coils in Germany. It is evident that no local coil is universally ideal for the general public. Each existing local coil has their own set of advantages and disadvantages regarding Tx performance, mainly achieving either high B_1^+ efficiency in the center or a large hf-excitation coverage. Regarding Rx performance, it has been shown that coils that can be folded to the sides of the phantom (i.e. C2, C4, C5 and C7) offer an advantage in SNR. But a standardized coil would be beneficial for multi-center studies, comparability studies and the potential extension of the existing 7 T CE label/FDA clearance for pTx brain imaging to whole-body imaging. Thus, the 8Tx32Rx array from ELH is recommended as a potential candidate for a standardized local pTx body coil as it achieved high B_1^+ in the center of the phantom, average hf-excitation coverage and one of the best Rx performance of the local coils.

The remote array, in combination with the dedicated local Rx array, performed overall very well. The 2.0-fold lower mean B_1^+ magnitude in the center of the phantom, which was expected due to the elements being placed further away, can be compensated by the four- or eight-fold higher available total RF power [31] of the current system at DKFZ. This ensures that the remote coil can also achieve high FA in the center of the phantom. Furthermore, the remote array showed minimal signal variation in hf-direction, making it an ideal choice for large field-of-excitation imaging. Additionally, the dedicated local Rx array achieved the highest SNR values in the center of the phantom. Similar to dedicated local Rx arrays at lower field strengths, they have the advantage to be placed at different positions without moving the Tx elements, thus the possibility to increase the SNR locally even more. However, as the remote coil needs an additional pTx system it is not directly usable for new sites. Therefore, the remote body coil in combination with an additional pTx is recommended for vendors to provide their new 7 T systems similar to 3 T or 1.5 T systems with a remote body coil placed behind the scanner bore liner and additionally dedicated local Rx arrays.

5.2 Validation of the RF pulse optimization method and the modified sequences

Phantom measurements were conducted to validate the k_T-point optimization method and the modified sequences. As the first pTx research articles showed that the acquired B_1^+ maps matched their corresponding FA predictions from Bloch simulations of the optimized RF pulses [14, 34, 109], no absolute B_1^+ mapping sequence with k_T-point was available and the focus was on *in-vivo* measurements, the pattern of the low FA GRE acquisition, with the receive profile still included, was compared with the FA predictions to validate the optimization method and the sequences [22, 110]. The dropouts in the FA predictions based on measured relative B_1^+ maps and in the signal magnitudes of the low FA acquisitions are located at the same position and also their pattern matched, thus validating the k_T-point optimization method and the modification of the sequences. If the modifications of the sequences would not be correct, the FA predictions and the GRE acquisition would not match and would lead to a FA dropout at a different position. The same would apply for the k_T-point optimization method. Nevertheless, residual signal intensity variations occurred in the magnitude images of the GRE acquisition using two and three k_T-points inside the ROI, which resulted from the receive sensitivities of the elements.

5.3 *In-vivo* studies

5.3.1 Investigation of homogeneous liver excitation using static and dynamic pTx

In-vivo measurements were conducted to investigate the performance of the remote 32-Tx-channel array for homogeneous liver excitation using static and dynamic pTx. Furthermore, the influence of different numbers of Tx channels on the resulting homogeneity was examined.

The measurements have demonstrated, that the remote array achieved sufficient FA homogeneity for normal-weight subjects using static pTx. CV values below 17.9% were reached in the FA predictions in all subjects and confirmed by the corresponding low FA acquisitions. The main advantage of static pTx for clinical applications is that the existing sequences do not have to be modified and thus, can directly be used in practice. This means that clinical studies investigating liver diseases [29, 111, 112, 113] have a

direct advantage when using a remote coil in combination with static pTx.

The remote coi in combination with two k_T-points reduced the CV even further. As more k_T-points did not reduce the homogeneity significantly, two k_T-points delivered a good tradeoff between RF power and FA homogeneity.

Comparing these results with work from Wu et al. [25], local coils with 8 Tx channels showed remaining FA dropouts in the liver in normal weight subjects in a single slice using static pTx. Also it has been shown that it is even more challenging to get a homogeneous excitation in the whole liver [26]. In both cases, dynamic pTx was needed to deliver a good homogeneity (two Spokes for a single slice in the liver and five k_T-points for the whole liver). For homogeneous heart excitation, a recent study showed that three to four k_T-points were necessary to achieve a practical tradeoff between FA homogeneity and RF power [22].

As the liver is the largest internal organ, similar results should be achieved for other internal organs or regions within the body with the size of the liver or smaller while using the 32-Tx-channel coil array in combination with static or dynamic pTx. This would benefit clinical studies requiring homogeneous excitation over a large area like investigating lymph nodes in pancreatic, duodenal, or periampullary adenocarcinoma [114] or for non-contrast enhanced renal angiography of both kidneys [18].

Another finding was that for two k_T-points a remote coil with 32 Tx channels provided an increase in homogeneity in comparison to using the remote coil with 8 Tx channels. To reach a comparable homogeneity with 8 Tx channels, a higher number of k_T-points was required. The benefits of a higher number of channels confirmed the results of Fiedler et al. [39], which investigated the influence of different numbers of channels on large 2D ROIs using simulated B_1^+ maps.

By selecting a relatively short total pulse length of approximately 1 ms, ΔB_0 influences are less pronounced [22]. As a result, additional acquisition of ΔB_0 maps for pulse optimization was not performed in favor of reducing the overall measurement time and making the approach more suitable for clinical applications.

During the subject measurements, instabilities were observed in some Tx channels, ei-

ther due to broken elements or damaged RF amplifiers. These issues were evident in the resulting B_1^+ maps, where affected channels displayed noticeably lower B_1^+ magnitude values. To address this issue, the relative B_1^+ maps were analyzed before each session, and channels exhibiting near-zero B_1^+ amplitude were excluded from pulse optimization. As a result, 28 functional channels were consistently used for all measurements. Nevertheless, despite four missing Tx channels, this work could demonstrate the benefit of the remote coil array in combination with a much higher number of Tx channels than the standard 8 or 16 channels of commercial pTx systems for liver applications.

Furthermore, local Rx arrays were necessary for relative B_1^+ mapping to enhance the SNR and improve the quality of the B_1^+ maps. However, this can have introduced additional bias, potentially making the underlying assumption [91] even less accurate. Nevertheless, the resulting FA predictions and the signal magnitudes of the small FA acquisitions matched, suggesting that the influence is limited.

It should also be mentioned, that the the experimental setup with the two local mechanically rigid Rx arrays was far from being ergonomic and comfortable. A more flexible anterior Rx array design like the anterior Rx array, which is nowadays available at the DKFZ, would provide increased subject comfort and would also place the individual Rx loop elements closer to the body surface for better Rx performance.

A key limitation in translating static and dynamic pTx into clinical application is the need for acquiring relative B_1^+ maps. This process is time-consuming, especially with higher channel counts (TA = 10:38 min), making it impractical for the use in clinical routine. To address this, ultra-fast B_1^+ mapping techniques using deep-learning based methods can be used, as the B_1^+ mapping time can be reduced to a few seconds [115, 116]. An alternative approach could be the use of calibration free universal dynamic pTx pulses, eliminating the need for subject-specific B_1^+ maps [105, 117, 118]. However, universal solutions generally offer lower homogeneity compared to subject-tailored pulses and the need for larger number of k_T-points.

5.3.2 Investigation of homogeneous abdomen excitation using static and dynamic pTx

In-vivo measurements were conducted to investigate the potential of the 32-Tx-channel remote array for whole abdomen imaging.

In comparison to liver excitation, static pTx did not deliver sufficient FA homogeneity for whole abdomen excitation. In this case, two k_T-points were necessary to achieve acceptable visual homogeneity in both FA predictions and signal magnitudes of the small FA acquisitions. However, GRE scans revealed small residual FA variations, which might be caused by ΔB_0 as it was not included in the design, yet. Additionally, different water-fat contrasts were achieved for different number of k_T-points, as the pulses were only optimized on the water frequency.

Ultrasmall superparamagnetic particles of ironoxide (USPIO)-enhanced MRI would directly benefit of homogeneous high-resolution abdomen imaging to find metastatic lymph nodes. Therefore, the current sequence needs to be extended to acquire multiple gradient echos to generate $T_2^\star$-weighted images in the upper abdomen [119]. Recent studies showed the advantages of USPIO-enhanced MRI for rectal cancer and prostate cancer screening which allowed more precise therapy and disease prognosis [120, 121].

Additionally, utilizing the remote array for Tx and Rx allows for the combination with X-nuclei arrays, enabling large FoV ^{1}H imaging alongside ^{23}Na imaging for metabolic quantification [41].

To improve the SNR of the measurements, the remote array can be used in combination with a dedicated local Rx array, i.e. the 32-Rx-channel array from Rapid, increasing the SNR in the center by a factor of 3.5.

TIAMO is an alternative to dynamic pTx and yielded sufficient FA homogeneity for the whole abdomen [32]. However, TIAMO requires longer measurement times compared to dynamic pTx which is a critical factor in clinical applications. There, a reduced measurement time is preferable, as either additional relevant sequences can be acquired or the total scanning time can be reduced which would also increase comfort for the patient. Another advantage of a shorter measurement time is the reduction of movement artifacts, as patient motion tends to increase with longer scan durations.

This study was also subject to limitations. Acquiring channel-wise relative B_1^+ maps of the abdomen using only the remote array extended the measurement time to 23:16 min as more data had to be acquired to overcome the lower SNR. For clinical translation,

fast mapping techniques [115, 116] are essential to reduce acquisition time to just a few seconds.

The experiments were conducted using a per channel RF power constraint for the safety supervision. In comparison to a VOP based safety supervision, this approach is more conservative, resulting in less RF power available, even for relative B_1^+ mapping. This led to noisier channel-wise B_1^+ maps in the center of the abdomen for the subjects, consequently also reducing the shimming performance. However, with the recent advancements in VOP calculation and compression algorithms [122], along with improved GPU power, a less conservative VOP-based real-time SAR supervision is now feasible [123]. This is expected to allow higher FA during the channel-wise B_1^+ mapping. Additionally, RF pulse optimization with local SAR constraint would be enabled, preventing local SAR hotspots [124].

Furthermore, the CV calculated for the different shims is biased by low proton density regions (i.e. air, bones). Masking these regions before optimization could further reduce the CV.

The acquired GRE images were reconstructed by averaging over the full respiratory cycle. However, it is possible to reconstruct the images for different respiratory states separately. This is expected to enhance image sharpness but will result in a reduced SNR [32].

Further subjects with a broader BMI range should be scanned to gain a comprehensive understanding of the application of k_T-points in the abdomen using the remote coil. Nevertheless, these *in-vivo* measurements demonstrated that whole-abdomen shimming is feasible using a remote 32-Tx-channel whole-body coil in combination with k_T-point pulses.

6 Conclusion

This thesis highlights the advantages of the MRexcite pTx system combined with a remote 32-channel coil array and a dedicated local 32-channel Rx array over local transceiver coils at 7 T. This setup achieves similarly high maximum B_1^+ values, superior excitation coverage in the hf-direction, and the highest SNR values. As the state-of-the-art solution for UHF body MRI, this system offers significant benefits for applications in clinical routine compared to commonly used local Tx/Rx coils. Despite the higher costs associated with the system and the remote coil, its advantages justify its adoption as the standard for future clinical 7 T MRI scanners. The phantom and *in-vivo* measurements performed within this work revealed that the dedicated local Rx array enhances handling, improves patient comfort, and thus, increases acceptance in clinical routine. Sufficient homogeneity was achieved in the liver with static pTx and 32 channels, whereas dynamic pTx was required with only eight remote and also local channels. The larger number of channels also enables a larger field-of-excitation in hf-direction, providing greater flexibility in patient positioning, an advantage for future applications. While reducing the number of channels could lower the costs, it would likely compromise hf-excitation coverage. However, this tradeoff could be promising for targeted abdominal or thoracic applications. Overall, the remote body coil is an essential step toward integrating UHF body MRI into clinical practice.

7 Appendix

7.1 Publications

Parts of this work are published in the following publications:

Conference Talks

Grimm, J.A.; Aigner, C.S.; Dietrich, S.; Orzada, S.; Nagel, A.M.; Ladd, M.E. and Schmitter, S. In-vivo 3D-Leberbildgebung bei 7T mit einer 32-Tx-Kanal-Ganzkörperspule und kT-Punkt pTx Pulsen. In *Proc. 53. Jahrestagung der Deutschen Gesellschaft für Medizinische Physik und 24. Jahrestagung der Deutschen Sektion der ISMRM, Aachen, Germany*, 2022, Abstract V076.

Grimm, J.A.; Aigner, C.S.; Dietrich, S.; Orzada, S.; Nagel, A.M.; Ladd, M.E. and Schmitter, S. In-vivo 3D liver imaging at 7T using kT-point pTx pulses and a 32-Tx-channel whole-body RF antenna array. In *Proc. 32nd Annual Meeting of ISMRM, Toronto, Canada*, 2023, Abstract 1419.

Grimm, J.A.; Aigner, C.S.; Dietrich, S.; Orzada, S.; Fiedler, T.M.; Nagel, A.M.; Ladd, M.E. and Schmitter, S. In-vivo validation of 3D liver imaging at 7T using kT-point pTx pulses with a 32-Tx-channel whole-body RF antenna array. In *Proc. 25. Jahrestagung der Deutschen Sektion der ISMRM, Berlin, Germany*, 2023.

Conference Posters

Grimm, J.A.; Aigner, C.S.; Dietrich, S.; Orzada, S.; Nagel, A.M.; Ladd, M.E. and Schmitter, S. Towards in-vivo 3D liver imaging at 7T using kT-point pTx pulses and a 32-Tx-channel whole-body RF coil. In *Proc. ISMRM Workshop on Ultra-High Field MR, Lisbon, Portugal*, 2022, Poster Abstract 42.

Grimm, J.A., Kraff, O.; May, M.; Lutz, M.; Orzada, O.; Quick, H.H., Ladd, M.E. and Schmitter, S. A comparison of various custom-built pTx RF arrays for body imaging at 7T with regard to their transmit efficiency. In *Proc. 33rd Annual Meeting of ISMRM, Singapore*, 2024, Abstract 4943.[1]

Grimm, J.A.; Aigner, C.S.; Schorling, C.; Dietrich, S.; Orzada, S.; Fiedler T.M.; Ladd, M.E. and Schmitter, S. In-vivo 7T body MRI with complete abdominal coverage using pTx and a 32-Tx-channel whole-body RF antenna array. In *Proc. 33rd Annual Meeting of ISMRM, Singapore*, 2024, Abstract 4941.

Grimm, J.A., Kraff, O.; May, M.; Lutz, M.; Orzada, O.; Fiedler, T.M.; Moeller, S.; Quick, H.H., Nagel, A.M.; Ladd, M.E. and Schmitter, S. A comparison of eight pTx RF body coils for 7T body imaging with regard to their Rx performance. *Proc. ISMRM Joint Workshop of the Ultra-High Field MR & Brain Function Study Groups, Annapolis, MD, USA*, 2025.

Further Submissions

Parts of this thesis have been submitted as a journal publication:

Research article

Grimm, J.A.; Aigner, C.S.; Dietrich, S.; Orzada, S.; Fiedler, T.M.; Schorling, C.; Quick, H.H.; Nagel, A.M.; Ladd, M.E. and Schmitter, S. In-vivo 3D liver imaging at 7T using kT-point pTx pulses and a 32-Tx-channel whole-body RF coil array. Submitted to: *NMR in Biomedicine*, 2024.

Further Scientific Contributions

In the following, further scientific contributions are listed:

Conference Talks

Scheipers, A.; Orzada, S.; **Grimm, J.A.**; Losch, J.; Fiedler, T.M.; Nagel, A.M.; Schmitter, S.; Ladd, M.E. and Platt, T. Quantitative Abdominal Sodium MRI

[1] This contribution was awarded the *3rd Place Award in the Hardware & Pulse Sequences Category* in the Ultra-High Field MR study.

Combined with 32-Channel Proton pTx MRI at 7T in a Large Field-of-View. In *Proc. 33rd Annual Meeting of ISMRM, Singapore*, 2024, Abstract 0522.

Bulanov, P.; Menshchikov, P.; **Grimm, J.A.**; Lutz, M.; Orzada, S.; Boyd, P.S.; Bachert, P.; Ladd, M.E.; Korzowski, A. and Schmitter, S. Relaxation-compensated CEST-MRI in the human liver at 7.0T. In *Proc. 40th Annual Scientific Meeting of ESMRMB, Barcelona, Portugal*, 2024.

Aigner, C.S.; **Grimm, J.A.**; Neelsen, C.J.; Jende, J.; Orzada, S.; Fiedler, T.M.; Schröder, S.; Kühn, S.; Ladd, M.E. and Schmitter, S. Imaging of the Entire Spinal Cord with a 32-Channel pTx Body Array at 7 T. In *Proc. 34th Annual Meeting of ISMRM, Honolulu, HI, United States*, 2025.

Conference Posters

Hadjikiriakos, K.; Krüger, F.; Zimmermann, F.; Riemann, L.; Degenhardt, K.; Hammernik, K.; **Grimm, J.A.**; Schmidt, S.; Metzger, G.; Ladd, M.E.; Schaeffter, T.; and Schmitter,S. Investigating the robustness of estimating B1maps by a neural network at different UHF sites. In *Proc. 33rd Annual Meeting of ISMRM, Singapore*, 2024, Abstract 4942.

Fiedler, T.M.; **Grimm, J.A.**; Klein, C.; Kratzer, F.; Mayer, F.; Orzada, S.; Schweins, L.; and Ladd, M.E. Real-time SAR Supervision for a 32-channel RF Transmit System with Virtual Observation Points. In *Proc. 33rd Annual Meeting of ISMRM, Singapore*, 2024, Abstract 3747.

Losch, J.; Scheipers, A.K.; **Grimm, J.A.**; Nagel, A.M.; Orzada, S.; Schmitter, S.; Ladd, M.E. and Platt, T. Quantification of Apparent Tissue Sodium Concentration (aTSC) in the Healthy Liver via 23Na and 1H MRI at 7T. In *Proc. 34th Annual Meeting of ISMRM, Honolulu, HI, United States*, 2025.

Aigner, C.S.; **Grimm, J.A.**; Neelsen, C.J.; Jende, J.; Orzada, S.; Fiedler, T.M.; Schröder, S.; Kühn, S.; Ladd, M.E. and Schmitter, S. Spinal Cord Imaging with a 32-Channel pTx Body Array at 7T. In *Proc. ISMRM Joint Workshop of the Ultra-High Field MR & Brain Function Study Groups, Annapolis, MD, USA*, 2025.

Bulanov, P.; Menshchikov, P.; **Grimm, J.A.**; Lutz, M.; Orzada, S.; Boyd, P.S.; Bachert, P.; Ladd, M.E.; Korzowski, A. and Schmitter, S. Reproducible liver CEST Imaging at 7 T with B1+ shimming. In *Proc. 34th Annual Meeting of ISMRM, Honolulu, HI, United States*, 2025.

Bulanov, P.; **Grimm, J.A.**; Lutz, M.; Orzada, S.; Bachert, P.; Ladd, M.E. and Schmitter, S. Liver and renal T1 relaxometry at 7 T. In *Proc. ISMRM Joint Workshop of the Ultra-High Field MR & Brain Function Study Groups, Annapolis, MD, USA*, 2025.

7.2 Further tools

For this thesis following additional tools have been used:

- Overleaf version 2024 for creation of the thesis in combination with LaTeX
- Overleaf template from Fabian Kratzer
- MATLAB R2018b and R2024b including MATLAB Toolboxes for coding, reconstruction and pulse optimization
- PTBToolbox as basis for B_1^+ mapping and pulse optimization
- Colormap CMOCEAN for creation of plots [125]
- MRF Reconstruction Toolbox from Max Lutz and all including Python packages
- ismrm_sunrise_matlab Toolbox from Michael Hansen for g-factor map calculation [126]
- IDEA for sequence development
- DeepL.com for translation
- Affinity Designer 2 for creation of figures
- ChatGPT-4o 2025 for linguistic revision and grammar
- Citavi 6 as reference manager

References

[1] M. C. Mabray, R. F. [JR] Barajas, and S. Cha. Modern brain tumor imaging. *Brain tumor research and treatment*, 3(1):8–23, 2015.

[2] M. Martucci, R. Russo, F. Schimperna, G. D'Apolito, M. Panfili, A. Grimaldi, A. Perna, A. M. Ferranti, G. Varcasia, C. Giordano, and S. Gaudino. Magnetic resonance imaging of primary adult brain tumors: State of the art and future perspectives. *Biomedicines*, 11(2), 2023.

[3] R. Bakshi, A. J. Thompson, M. A. Rocca, D. Pelletier, V. Dousset, F. Barkhof, M. Inglese, C. R. G. Guttmann, M. A. Horsfield, and M. Filippi. Mri in multiple sclerosis: current status and future prospects. *The Lancet. Neurology*, 7(7):615–625, 2008.

[4] M. Cosottini and L. Roccatagliata. Neuroimaging at 7 t: are we ready for clinical transition? *European Radiology Experimental*, 5(1):37, 2021.

[5] F. Lüsebrink, A. Sciarra, H. Mattern, R. Yakupov, and O. Speck. T 1 -weighted in vivo human whole brain mri dataset with an ultrahigh isotropic resolution of 250 μm. *Scientific Data*, 4, 2017.

[6] E. Springer, B. Dymerska, P. L. Cardoso, S. D. Robinson, C. Weisstanner, R. Wiest, B. Schmitt, and S. Trattnig. Comparison of routine brain imaging at 3 t and 7 t. *Investigative radiology*, 51(8):469–482, 2016.

[7] M. E. Ladd, P. Bachert, M. Meyerspeer, E. Moser, A. M. Nagel, D. G. Norris, S. Schmitter, O. Speck, S. Straub, and M. Zaiss. Pros and cons of ultra-high-field mri/mrs for human application. *Progress in nuclear magnetic resonance spectroscopy*, 109:1–50, 2018.

[8] J. T. Vaughan, C. J. Snyder, L. J. DelaBarre, P. J. Bolan, J. Tian, L. Bolinger, G. Adriany, P. Andersen, J. Strupp, and K. Ugurbil. Whole-body imaging at 7t: preliminary results. *Magnetic resonance in medicine*, 61(1):244–248, 2009.

[9] M. C. Maas, E. K. Vos, M. W. Lagemaat, A. K. Bitz, S. Orzada, T. Kobus, O. Kraff, S. Maderwald, M. E. Ladd, and T. W. J. Scheenen. Feasibility of t2 -weighted turbo spin echo imaging of the human prostate at 7 tesla. *Magnetic resonance in medicine*, 71(5):1711–1719, 2014.

[10] O. Kraff and H. H. Quick. Radiofrequency coils for 7 tesla mri. *Topics in magnetic resonance imaging : TMRI*, 28(3):145–158, 2019.

[11] Q. X. Yang, W. Mao, J. Wang, M. B. Smith, H. Lei, X. Zhang, K. Ugurbil, and W. Chen. Manipulation of image intensity distribution at 7.0 t: passive rf shimming and focusing with dielectric materials. *Journal of magnetic resonance imaging : JMRI*, 24(1):197–202, 2006.

[12] A. G. Webb. Dielectric materials in magnetic resonance. *Concepts in Magnetic Resonance*, 38A(4):148–184, 2011.

[13] P. Balchandani, M. Khalighi, G. Glover, J. Pauly, and D. Spielman. Self-refocused adiabatic pulse for spin echo imaging at 7 t. *Magnetic resonance in medicine*, 67:1077–1085, 2012.

[14] Y. Zhu. Parallel excitation with an array of transmit coils. *Magnetic resonance in medicine*, 51(4):775–784, 2004.

[15] U. Katscher and P. Börnert. Parallel rf transmission in mri. *NMR in Biomedicine*, 19(3):393–400, 2006.

[16] G. J. Metzger, C. Snyder, C. Akgun, T. Vaughan, K. Ugurbil, and P. F. van de Moortele. Local b1+ shimming for prostate imaging with transceiver arrays at 7t based on subject-dependent transmit phase measurements. *Magnetic resonance in medicine*, 59(2):396–409, 2008.

[17] L. Umutlu, O. Kraff, S. Orzada, A. Fischer, S. Kinner, S. Maderwald, G. Antoch, H. H. Quick, M. Forsting, M. E. Ladd, and T. C. Lauenstein. Dynamic contrast-enhanced renal mri at 7 tesla: preliminary results. *Investigative radiology*, 46(7):425–433, 2011.

[18] G. J. Metzger, E. J. Auerbach, C. Akgun, J. Simonson, X. Bi, K. Uğurbil, and P. F. van de Moortele. Dynamically applied b1+ shimming solutions for non-contrast enhanced renal angiography at 7.0 tesla. *Magnetic resonance in medicine*, 69(1):114–126, 2013.

[19] W. Zhao, J. Cohen-Adad, J. R. Polimeni, B. Keil, B. Guerin, K. Setsompop, P. Serano, A. Mareyam, P. Hoecht, and L. L. Wald. Nineteen-channel receive array and four-channel transmit array coil for cervical spinal cord imaging at 7t. *Magnetic resonance in medicine*, 72(1):291–300, 2014.

[20] A. Henning, W. Koning, A. Fuchs, A. Raaijmakers, J. J. Bluemink, C. A. T. van den Berg, V. O. Boer, and D. W. J. Klomp. 1h mrs in the human spinal cord at 7 t using a dielectric waveguide transmitter, rf shimming and a high density receive array. *NMR in Biomedicine*, 29(9):1231–1239, 2016.

[21] S. By, J. V. Rispoli, S. Cheshkov, I. Dimitrov, J. Cui, S. Seiler, S. Goudreau, C. Malloy, S. M. Wright, and M. P. McDougall. A 16-channel receive, forced current excitation dual-transmit coil for breast imaging at 7t. *PLOS ONE*, 9(11):e113969, 2014.

[22] C. S. Aigner, S. Dietrich, and S. Schmitter. Three-dimensional static and dynamic parallel transmission of the human heart at 7 t. *NMR in Biomedicine*, 34(3):e4450, 2021.

[23] J. Ellermann, U. Goerke, P. Morgan, K. Ugurbil, J. Tian, S. Schmitter, T. Vaughan, and P. F. van de Moortele. Simultaneous bilateral hip joint imaging at 7 tesla using fast transmit b_1 shimming methods and multichannel transmission - a feasibility study. *NMR in Biomedicine*, 25(10):1202–1208, 2012.

[24] C. M. Deniz, R. Brown, R. Lattanzi, L. Alon, D. K. Sodickson, and Y. Zhu. Maximum efficiency radiofrequency shimming: Theory and initial application for hip imaging at 7 tesla. *Magnetic resonance in medicine*, 69(5):1379–1388, 2013.

[25] X. Wu, S. Schmitter, E. Auerbach, K. Uğurbil, and P. F. van de Moortele. Mitigating transmit b1 inhomogeneity in the liver at 7t using multi-spoke parallel transmit rf pulse design. *Quantitative imaging in medicine and surgery*, 4:4–10, 2014.

[26] B. A. Runderkamp, W. van der Zwaag, T. Roos, G. J. Strijkers, M. W. A. Caan, and A. J. Nederveen. Whole-liver flip angle shimming at 7t using eight-channel parallel transmission kt-points pulses with fpe-dream b1+ mapping. *Proceedings of the 31st Annual Meeting of ISMRM, London, UK*, page #2869, 2022.

[27] A. Laader, K. Beiderwellen, O. Kraff, S. Maderwald, K. Wrede, M. E. Ladd, T. C. Lauenstein, M. Forsting, H. H. Quick, K. Nassenstein, and L. Umutlu. 1.5 versus 3 versus 7 tesla in abdominal mri: A comparative study. *PLOS ONE*, 12(11):e0187528, 2017.

[28] S. Orzada, S. Maderwald, B. A. Poser, A. K. Bitz, H. H. Quick, and M. E. Ladd. Rf excitation using time interleaved acquisition of modes (tiamo) to address b1 inhomogeneity in high-field mri. *Magnetic resonance in medicine*, 64(2):327–333, 2010.

[29] L. Umutlu, A. K. Bitz, S. Maderwald, S. Orzada, S. Kinner, O. Kraff, I. Brote, S. C. Ladd, T. Schroeder, M. Forsting, G. Antoch, M. E. Ladd, H. H. Quick, and T. C. Lauenstein. Contrast-enhanced ultra-high-field liver mri: A feasibility trial. *European Journal of Radiology*, 82(5):760–767, 2013.

[30] B. J. W. Philips, A. S. Fortuin, S. Orzada, T. J. Scheenen, and M. C. Maas. High resolution mr imaging of pelvic lymph nodes at 7 tesla. *Magnetic resonance in medicine*, 78(3):1020–1028, 2017.

[31] S. Orzada, K. Solbach, M. Gratz, S. Brunheim, T. M. Fiedler, S. Johst, A. K. Bitz, S. Shooshtary, A. Abuelhaija, M. N. Voelker, S. H. G. Rietsch, O. Kraff, S. Maderwald, M. Flöser, M. Oehmigen, H. H. Quick, and M. E. Ladd. A 32-channel parallel transmit system add-on for 7t mri. *PLOS ONE*, 14(9):e0222452, 2019.

[32] I. T. Maatman, J. Schulz, S. Ypma., K. T. Block, S. Schmitter, J. J. Hermans, E. J. Smit, M. C. Maas, and T. W. J. Scheenen. Free-breathing high-resolution respiratory-gated radial stack-of-stars magnetic resonance imaging of the upper abdomen at 7 t. *NMR in Biomedicine*, 37(10):e5180, 2024.

[33] R. Deichmann, C. D. Good, and R. Turner. Rf inhomogeneity compensation in structural brain imaging. *Magnetic resonance in medicine*, 47(2):398–402, 2002.

[34] M. A. Cloos, N. Boulant, M. Luong, G. Ferrand, E. Giacomini, D. Le Bihan, and A. Amadon. kt-points: Short three-dimensional tailored rf pulses for flip-angle homogenization over an extended volume. *Magnetic resonance in medicine*, 67(1):72–80, 2012.

[35] S. J. Malik, S. Keihaninejad, A. Hammers, and J. V. Hajnal. Tailored excitation in 3d with spiral nonselective (spins) rf pulses. *Magnetic resonance in medicine*, 67(5):1303–1315, 2012.

[36] S. Schmitter, L. DelaBarre, X. Wu, A. Greiser, D. Wang, E. J. Auerbach, J. T. Vaughan, K. Uğurbil, and P. F. van de Moortele. Cardiac imaging at 7 tesla:

Single- and two-spoke radiofrequency pulse design with 16-channel parallel excitation. *Magnetic resonance in medicine*, 70(5):1210–1219, 2013.

[37] B. A. Runderkamp, T. Roos, W. van der Zwaag, G. J. Strijkers, M. W. A. Caan, and A. J. Nederveen. Whole-liver flip-angle shimming at 7 t using parallel-transmit kt-point pulses and fourier phase-encoded dream b1+ mapping. *Magnetic resonance in medicine*, 91(1):75–90, 2024.

[38] S. Shirvani, B. Ding, I. Dragonu, P. Liebig, C. Rua, J. Karkouri, D. Klomp, A. T. Hess, and C. T. Rodgers. Initial experience on 7t terra for human parallel transmit (ptx) liver imaging. *Proceedings of the 29th Annual Meeting of ISMRM*, page #4288, 2020.

[39] T. M. Fiedler, S. Orzada, M. Flöser, S. H. G. Rietsch, H. H. Quick, M. E. Ladd, and A. K. Bitz. Performance analysis of integrated rf microstrip transmit antenna arrays with high channel count for body imaging at 7 t. *NMR in Biomedicine*, 34(7):e4515, 2021.

[40] T. M. Fiedler, S. Orzada, M. Flöser, S. H. G. Rietsch, S. Schmidt, J. K. Stelter, M. Wittrich, H. H. Quick, A. K. Bitz, and M. E. Ladd. Performance and safety assessment of an integrated transmit array for body imaging at 7 t under consideration of specific absorption rate, tissue temperature, and thermal dose. *NMR in Biomedicine*, 35(5):e4656, 2022.

[41] A. K. Scheipers, S. Orzada, J. A. Grimm, J. Felz, T. M. Fiedler, A. M. Nagel, S. Schmitter, M. E. Ladd, and T. Platt. Quantitative abdominal sodium mri combined with 32-channel proton ptx mri at 7t in a large field-of-view. *Proceedings of the 33rd Annual Meeting of ISMRM, Singapur*, page #0522, 2024.

[42] A. Abragam. *The Principles of Nuclear Magnetism*. International series of monographs on physics. Clarendon Press, 1961.

[43] P. T. Callaghan. *Principles of nuclear magnetic resonance microscopy*. Oxford science publications. Clarendon Press, Oxford, 1. publ. as paperback with corr edition, 1993.

[44] C. P. Slichter. *Principles of Magnetic Resonance*. Springer Series in Solid-State Sciences. Springer Berlin Heidelberg, 1996.

[45] R. K. Harris, E. D. Becker, Cabral De Menezes, S. M., R. Goodfellow, and P. Granger. Nmr nomenclature: Nuclear spin properties and conventions for chemical shifts. iupac recommendations 2001. *Solid State Nuclear Magnetic Resonance*, 22(4):458–483, 2002.

[46] M. A. Bernstein, K. F. King, and X. J. Zhou. *Handbook of MRI Pulse Sequences*. Academic Press, 2004.

[47] E. M. Haacke, R. W. Brown, M. R. Thompson, and R. Venkatesan. *Magnetic Resonance Imaging: Physical Principles and Sequence Design*. Wiley, 1999.

[48] J. W. Cooley and J. W. Tukey. An algorithm for the machine calculation of complex fourier series. *Mathematics of Computation*, 19(90):297–301, 1965.

[49] J. Pauly, D. Nishimura, and A. Macovski. A k-space analysis of small-tip-angle excitation. *Journal of Magnetic Resonance*, 81(1):43–56, 1989.

[50] Di Hoult. The solution of the bloch equations in the presence of a varying b1 field—an approach to selective pulse analysis. *Journal of Magnetic Resonance*, 35(1):69–86, 1979.

[51] W. S. Hinshaw and A. H. Lent. An introduction to nmr imaging: From the bloch equation to the imaging equation. *Proceedings of the IEEE*, 71(3):338–350, 1983.

[52] D.I Hoult and Paul C. Lauterbur. The sensitivity of the zeugmatographic experiment involving human samples. *Journal of Magnetic Resonance (1969)*, 34(2):425–433, 1979.

[53] E. R. McVeigh, R. M. Henkelman, and M. J. Bronskill. Noise and filtration in magnetic resonance imaging. *Medical physics*, 12(5):586–591, 1985.

[54] H. Gudbjartsson and S. Patz. The rician distribution of noisy mri data. *Magnetic resonance in medicine*, 34(6):910–914, 1995.

[55] National Electrical Manufacturers Association. Determination of signal-to-noise ratio (snr) in dagnostic magnetic resonance imaging. *NEMA Standards Publication*, MS 1-2008 (R2014, R2020), 2021.

[56] P. B. Roemer, W. A. Edelstein, C. E. Hayes, S. P. Souza, and O. M. Mueller. The nmr phased array. *Magnetic resonance in medicine*, 16(2):192–225, 1990.

[57] J. Hamilton, D. Franson, and N. Seiberlich. Recent advances in parallel imaging for mri. *Progress in nuclear magnetic resonance spectroscopy*, 101:71–95, 2017.

[58] M. A. Griswold, P. M. Jakob, R. M. Heidemann, M. Nittka, V. Jellus, J. Wang, B. Kiefer, and A. Haase. Generalized autocalibrating partially parallel acquisitions (grappa). *Magnetic resonance in medicine*, 47(6):1202–1210, 2002.

[59] K. P. Pruessmann, M. Weiger, M. B. Scheidegger, and P. Boesiger. Sense: Sensitivity encoding for fast mri. *Magnetic resonance in medicine*, 42(5):952–962, 1999.

[60] International Electrotechnical Commission. *Medical electrical equipment - Part 2-33: Particular requirements for the basic safety and essential performance of magnetic resonance equipment for medical diagnosis*, volume IEC 60601-2-33 of *Norme internationale*. International Electrotechnical Commission, Geneva, Switzerland, edition 4.0 edition, 2022.

[61] B. Guérin, J. F. Villena, A. G. Polimeridis, E. Adalsteinsson, L. Daniel, J. K. White, and L. L. Wald. The ultimate signal-to-noise ratio in realistic body models. *Magnetic resonance in medicine*, 78(5):1969–1980, 2017.

[62] R. Pohmann, O. Speck, and K. Scheffler. Signal-to-noise ratio and mr tissue parameters in human brain imaging at 3, 7, and 9.4 tesla using current receive coil arrays. *Magnetic resonance in medicine*, 75(2):801–809, 2016.

[63] Caroline Le Ster, Andrea Grant, P. F. van de Moortele, A. Monreal-Madrigal, G. Adriany, A. Vignaud, F. Mauconduit, C. Rabrait-Lerman, B. A. Poser, K. Uğurbil, and N. Boulant. Magnetic field strength dependent snr gain at the center of a spherical phantom and up to 11.7t. *Magnetic resonance in medicine*, 88(5):2131–2138, 2022.

[64] D. Stucht, K. A. Danishad, P. Schulze, F. Godenschweger, M. Zaitsev, and O. Speck. Highest resolution in vivo human brain mri using prospective motion correction. *PLOS ONE*, 10(7):e0133921, 2015.

[65] E. Moser, F. Stahlberg, M. E. Ladd, and S. Trattnig. 7-t mr—from research to clinical applications? *NMR in Biomedicine*, 25(5):695–716, 2012.

[66] M. Zaiss and A. Mennecke. Chapter 28 - chemical exchange saturation transfer mri in the human brain at ultra-high fields. In B. K. Markenroth, M. Guye, and B. A.

Poser, editors, *Advances in Magnetic Resonance Technology and Applications : Ultra-High Field Neuro MRI*, volume 10, pages 463–473. Academic Press, 2023.

[67] N. S. Arango, B. Pinho-Meneses, and J. P. Stockmann. Chapter 6 - b0 inhomogeneity: Causes and coping strategies. In Markenroth B. K., M. Guye, and B. A. Poser, editors, *Advances in Magnetic Resonance Technology and Applications : Ultra-High Field Neuro MRI*, volume 10, pages 75–96. Academic Press, 2023.

[68] B. P. Sutton and F. Lam. Chapter 12 - imaging in the presence of magnetic field inhomogeneities. In M. Akçakaya, M. Doneva, and C. Prieto, editors, *Advances in Magnetic Resonance Technology and Applications : Magnetic Resonance Image Reconstruction*, volume 7, pages 327–354. Academic Press, 2022.

[69] K. Uğurbil. Imaging at ultrahigh magnetic fields: History, challenges, and solutions. *NeuroImage*, 168:7–32, 2018.

[70] P. Börnert and B. Aldefeld. On spatially selective rf excitation and its analogy with spiral mr image acquisition. *Magnetic Resonance Materials in Physics, Biology and Medicine*, 7(3):166–178, 1998.

[71] C. Yip, J. A. Fessler, and D. C. Noll. Iterative rf pulse design for multidimensional, small-tip-angle selective excitation. *Magnetic resonance in medicine*, 54(4):908–917, 2005.

[72] F. Padormo, A. Beqiri, J. V. Hajnal, and S. J. Malik. Parallel transmission for ultrahigh-field imaging. *NMR in Biomedicine*, 29(9):1145–1161, 2016.

[73] W. Grissom, C. Yip, Z. Zhang, V. A. Stenger, J. A. Fessler, and D. C. Noll. Spatial domain method for the design of rf pulses in multicoil parallel excitation. *Magnetic resonance in medicine*, 56(3):620–629, 2006.

[74] J. Petzold, S. Schmitter, B. Silemek, L. Winter, O. Speck, and Ittermann, B. Seifert, F. Investigation of alternative rf power limit control methods for 0.5t, 1.5t, and 3t parallel transmission cardiac imaging: A simulation study. *Magnetic resonance in medicine*, 91(4):1659–1675, 2024.

[75] I. Brote, S. Orzada, O. Kraff, S. Maderwald, H. H. Quick, P. Yazdanbakhsh, K. Solbach, K. Wicklow, A. Bahr, T. Bolz, M. E. Ladd, and A. K. Bitz. A multichannel sar prediction and online monitoring system at 7t. *Proceedings of the 17th Annual Meeting ISMRM, Honolulu, HI*, page #4788, 2009.

[76] I. Graesslin, P. Vernickel, P. Börnert, K. Nehrke, G. Mens, P. Harvey, and U. Katscher. Comprehensive rf safety concept for parallel transmission mr. *Magnetic resonance in medicine*, 74(2):589–598, 2015.

[77] R. Gumbrecht, U. Fontius, H. Adolf, T. Benner, F. Schmitt, E. Adalsteinsson, L. L. Wald, and H.-P. Fautz. Online local sar supervision for transmit arrays at 7t. *Proceedings of the 21st Annual Meeting of ISMRM, Montréal, Québec*, page #4420, 2013.

[78] S. Schmidt. *Aufbau einer 8-Kanal Sende-/Empfangsspule zur 1H-Bildgebund des Körperrumpfes bei 7 Tesla*. Bachelor thesis, Universität Heidelberg, 2014.

[79] S. Orzada, H. H. Quick, M. E. Ladd, A. Bahr, T. Bolz, P. Yazdanbakhsh, K. Solbach, and A. K. Bitz. A flexible 8–channel transmit/receive body coil for 7 t human imaging. *Proceeding of the 17th Annual Meeting of ISMRM, Honolulu, HI*, page #2999, 2009.

[80] S. G.H. Rietsch, H. H. Quick, and S. Orzada. Impact of different meander sizes on the rf transmit performance and coupling of microstrip line elements at 7 t. *Medical physics*, 42(8):4542–4552, 2015.

[81] M. Terekhov, D. Lohr, T. Reiter, I. A. Elabyad, M. Hock, and L. M. Schreiber. New commercial 8tx/16rx array for clinical 7t cardiac mri: initial experience. *Proceedings of the 29th Annual Meeting ISMRM, virtual*, page #1584, 2021.

[82] M. Weirauch. *Entwicklung und Evaluation eines 8-Kanal Sende- und Empfangsarray-Gehäuses zur Optimierung der Körperbildgebung mittels 7 Tesla MRT*. Bachelor thesis, Hochschule Ruhr West, 2023.

[83] S. G.H. Rietsch, S. Orzada, S. Maderwald, S. Brunheim, B. W. J. Philips, T. J.W. Scheenen, M. E. Ladd, and H. H. Quick. 7t ultra-high field body mr imaging with an 8-channel transmit/32-channel receive radiofrequency coil array. *Medical physics*, 45(7):2978–2990, 2018.

[84] S. Dietrich, C. S. Aigner, C. Kolbitsch, J. Mayer, J. Ludwig, S. Schmidt, T. Schaeffter, and S. Schmitter. 3d free-breathing multichannel absolute mapping in the human body at 7t. *Magnetic resonance in medicine*, 85(5):2552–2567, 2021.

[85] MRI.TOOLS GmbH. Large fov torso transceiver array rf coil, 2025.

[86] M. A. Ertürk, A. J. E. Raaijmakers, G. Adriany, K. Uğurbil, and G. J. Metzger. A 16-channel combined loop-dipole transceiver array for 7 tesla body mri. *Magnetic resonance in medicine*, 77(2):884–894, 2017.

[87] N. Schoen, F. Seifert, J. Petzold, G. J. Metzger, O.r Speck, B. Ittermann, and S. Schmitter. The impact of respiratory motion on electromagnetic fields and specific absorption rate in cardiac imaging at 7t. *Magnetic resonance in medicine*, 88(6):2645–2661, 2022.

[88] S. H. G. Rietsch, S. Brunheim, S. Orzada, M. N. Voelker, Maderwald, S. Bitz, A. K., Gratz, M. Ladd, M. E., and H. H. Quick. Development and evaluation of a 16-channel receive-only rf coil to improve 7t ultra-high field body mri with focus on the spine. *Magnetic resonance in medicine*, 82(2):796–810, 2019.

[89] W. A. Grissom, M.-M. Khalighi, L. I. Sacolick, B. K. Rutt, and M. W. Vogel. Small-tip-angle spokes pulse design using interleaved greedy and local optimization methods. *Magnetic Resonance in Medicine*, 68(5):1553–1562, 2012.

[90] Z. Cao, X. Yan, and W. A. Grissom. Array-compressed parallel transmit pulse design. *Magnetic Resonance in Medicine*, 76(4):1158–1169, 2016.

[91] P. F. van de Moortele and K. Ugurbil. Very fast multi channel b1 calibration at high field in the small flip angle regime. *Proceedings of the 17th Annual Meeting ISMRM, Honolulu, HI*, page #367, 2009.

[92] V. L. Yarnykh. Actual flip-angle imaging in the pulsed steady state: A method for rapid three-dimensional mapping of the transmitted radiofrequency field. *Magnetic resonance in medicine*, 57(1):192–200, 2007.

[93] K. Nehrke and P. Börnert. Dream—a novel approach for robust, ultrafast, multi-slice b1 mapping. *Magnetic resonance in medicine*, 68(5):1517–1526, 2012.

[94] R. Pohmann and K. Scheffler. A theoretical and experimental comparison of different techniques for b_1 mapping at very high fields. *NMR in Biomedicine*, 26(3):265–275, 2013.

[95] M. Lutz, C. S. Aigner, S. Flassbeck, F. Krueger, C. G. F. Gatefait, C. Kolbitsch, B. Silemek, F. Seifert, T. Schaeffter, and S. Schmitter. B1-mrf: Large dynamic range mrf-based absolute mapping in the human body at 7t. *Magnetic resonance in medicine*, 92(6):2473–2490, 2024.

[96] P. F. van de Moortele, C. Snyder, L. DelaBarre, G. Adriany, J. T. Vaughan, and K. Ugurbil. Calibration tools for rf shim at very high field with multiple element rf coils: from ultra fast local relative phase to absolute magnitude b1+ mapping. *Proceedings of the 15th Annual Meeting ISMRM, Berlin, Germany*, page #1676, 2007.

[97] S. Brunheim, M. Gratz, S. Johst, A. K. Bitz, T. M. Fiedler, M. E. Ladd, H. H. Quick, and S. Orzada. Fast and accurate multi-channel mapping based on the tiamo technique for 7t uhf body mri. *Magnetic resonance in medicine*, 79(5):2652–2664, 2018.

[98] P. Kellman and E. R. McVeigh. Image reconstruction in snr units: a general method for snr measurement. *Magnetic resonance in medicine*, 54(6):1439–1447, 2005.

[99] M. Uecker, P. Lai, M. J. Murphy, P. Virtue, M. Elad, J. M. Pauly, S. S. Vasanawala, and M. Lustig. Espirit–an eigenvalue approach to autocalibrating parallel mri: where sense meets grappa. *Magnetic resonance in medicine*, 71(3):990–1001, 2014.

[100] P. M. Robson, A. K. Grant, A. J. Madhuranthakam, R. Lattanzi, D. K. Sodickson, and C. A. McKenzie. Comprehensive quantification of signal-to-noise ratio and g-factor for image-based and k-space-based parallel imaging reconstructions. *Magnetic resonance in medicine*, 60(4):895–907, 2008.

[101] C. Prieto, S. Uribe, R. Razavi, D. Atkinson, and T. Schaeffter. 3d undersampled golden-radial phase encoding for dce-mra using inherently regularized iterative sense. *Magnetic resonance in medicine*, 64(2):514–526, 2010.

[102] C. Buerger, R. E. Clough, A. P. King, T. Schaeffter, and C. Prieto. Nonrigid motion modeling of the liver from 3-d undersampled self-gated golden-radial phase encoded mri. *IEEE transactions on medical imaging*, 31(3):805–815, 2012.

[103] J. Mayer. *Imaging vulnerable coronary plaques using 3D motion-corrected simultaneous PET/MR*. PhD thesis, Technische Universität Berlin, 2021.

[104] J. I. Jackson, C. H. Meyer, D. G. Nishimura, and A. Macovski. Selection of a convolution function for fourier inversion using gridding computerised tomography application. *IEEE transactions on medical imaging*, 10(3):473–478, 1991.

[105] C. S. Aigner, S. Dietrich, and S. Schmitter. Respiration induced b1+ changes and their impact on universal and tailored 3d kt-point parallel transmission pulses for 7t cardiac imaging. *Magnetic resonance in medicine*, 87(6):2862–2871, 2022.

[106] D. O. Walsh, A. F. Gmitro, and M. W. Marcellin. Adaptive reconstruction of phased array mr imagery. *Magnetic resonance in medicine*, 43(5):682–690, 2000.

[107] S. G.H. Rietsch, S. Orzada, A. K. Bitz, Gratz, M. Ladd, M.E., and H. H. Quick. Parallel transmit capability of various rf transmit elements and arrays at 7t mri. *Magnetic resonance in medicine*, 79(2):1116–1126, 2018.

[108] N. Himburg, M. Lutz, L. Mitschang, J. G. Frintz, and S. Schmitter. Signal interferences in actual flip angle imaging (afi) of polyvinylpyrrolidone (pvp) solutions. *Proceedings of the 33rd Annual Meeting of ISMRM, Singapur*, page #4429, 2024.

[109] U. Katscher, P. Börnert, C. Leussler, and J. S. van den Brink. Transmit sense. *Magnetic resonance in medicine*, 49(1):144–150, 2003.

[110] X. Wu, S. Schmitter, E. J. Auerbach, J. Pfeuffer, M. Hamm, K. Ugurbil, and P. F. van de Moortele. Parallel transmission in liver mri at 7t: initial results. *Proceedings of the 19th Annual Meeting ISMRM, Montréal, Québec, Canada HI*, page #2940, 2011.

[111] A. Fischer, O. Kraff, S. Maderwald, K. Beiderwellen, M. E. Ladd, M. Forsting, T. C. Lauenstein, and L. Umutlu. Non-enhanced t1-weighted liver vessel imaging at 7 tesla. *PLOS ONE*, 9(6):e97465, 2014.

[112] A. Shimizu, K. Ito, K. Sasaki, M. Hayashida, M. Tanabe, K. Shimizu, and N. Matsunaga. Small hyperintense hepatic lesions on t1-weighted images in patients with cirrhosis: evaluation with serial mri and imaging features for clinical benignity. *Magnetic resonance imaging*, 25(10):1430–1436, 2007.

[113] L. N. Vu, J. N. Morelli, and J. Szklaruk. Basic mri for the liver oncologists and surgeons. *Journal of hepatocellular carcinoma*, 5:37–50, 2017.

[114] G. Litjens, A. Nakamoto, L. A. A. Brosens, M. C. Maas, T. W. J. Scheenen, P. Zámecnik, E. J. M. van Geenen, M. Prokop, K. J. H. M. van Laarhoven, and J. J. Hermans. Ferumoxtran-10-enhanced mri for pre-operative metastatic lymph node detection in pancreatic, duodenal, or periampullary adenocarcinoma. *European Radiology*, 2024.

[115] F. Krueger, C. S. Aigner, K. Hammernik, S. Dietrich, M. Lutz, J. Schulz-Menger, T. Schaeffter, and S. Schmitter. Rapid estimation of 2d relative b1+-maps from localizers in the human heart at 7t using deep learning. *Magnetic resonance in medicine*, 89(3):1002–1015, 2023.

[116] B. Eberhardt, B. A. Poser, N. J. Shah, and J. Felder. B1 field map synthesis with generative deep learning used in the design of parallel-transmit rf pulses for ultra-high field mri. *Zeitschrift fur medizinische Physik*, 32(3):334–345, 2022.

[117] N. Egger, S. Nagelstraßer, S. Wildenberg, A. Bitz, L. Ruck, J. Herrler, C. R. Meixner, R. Kimmlingen, T. Lanz, S. Schmitter, M. Uder, and A. M. Nagel. Accelerated mapping and robust parallel transmit pulse design for heart and prostate imaging at 7 t. *Magnetic resonance in medicine*, 92(5):1933–1951, 2024.

[118] V. Gras, A. Vignaud, A. Amadon, D. Le Bihan, and N. Boulant. Universal pulses: A new concept for calibration-free parallel transmission. *Magnetic resonance in medicine*, 77(2):635–643, 2017.

[119] T. W. J. Scheenen and P. Zamecnik. The role of magnetic resonance imaging in (future) cancer staging: Note the nodes. *Investigative radiology*, 56(1):42–49, 2021.

[120] R. C. H. Stijns, B. W. J. Philips, I. D. Nagtegaal, F. Polat, J. H. W. de Wilt, C. A. P. Wauters, P. Zamecnik, J. J. Fütterer, and T. W. J. Scheenen. Uspio-enhanced mri of lymph nodes in rectal cancer: A node-to-node comparison with histopathology. *European Journal of Radiology*, 138:109636, 2021.

[121] R. A. M. Heesakkers, A. M. Hövels, Ge. J. Jager, H. C. M. van den Bosch, J. A. Witjes, H. P. J. Raat, J. L. Severens, E. M. M. Adang, C. H. van der Kaa, J. J. Fütterer, and J. Barentsz. Mri with a lymph-node-specific contrast agent as an alternative to ct scan and lymph-node dissection in patients with prostate cancer: a prospective multicohort study. *The Lancet. Oncology*, 9(9):850–856, 2008.

[122] S. Orzada, T. M. Fiedler, and M. E. Ladd. Hybrid algorithms for sar matrix compression and the impact of post-processing on sar calculation complexity. *Magnetic resonance in medicine*, 92(6):2696–2706, 2024.

[123] T. M. Fiedler, J. A. Grimm, C. Klein, F. Kratzer, F. Mayer, S. Orzada, L. Schweins, and M. E. Ladd. Real-time sar supervision for a 32-channel rf transmit system with

virtual observation points. *Proceedings of the 33rd Annual Meeting of ISMRM, Singapur*, page #3747, 2024.

[124] B. Guérin, M. Gebhardt, S. Cauley, E. Adalsteinsson, and L. L. Wald. Local specific absorption rate (sar), global sar, transmitter power, and excitation accuracy trade-offs in low flip-angle parallel transmit pulse design. *Magnetic resonance in medicine*, 71(4):1446–1457, 2014.

[125] K. Thyng, C. Greene, R. Hetland, H. Zimmerle, and S. DiMarco. True colors of oceanography: Guidelines for effective and accurate colormap selection. *Oceanography*, 29(3):9–13, 2016.

[126] M. S. Hansen. Ismrm 2014 sunrise course on parallel imaging. `https://hansenms.github.io/sunrise/sunrise2014/`. Accessed: 2025-01-15.

Acronyms

AFI actual flip angle imaging

ap anterior-posterior

B1R relative channel-wise B_1^+

BMI body mass index

BOLD blood-oxygen-level-dependent

CEST chemical exchange saturation transfer

CNR contrast-to-noise ratio

CV coefficient of variation

DKFZ German Cancer Research Center

DREAM dual refocusing echo acquisition mode

ELH Erwin L. Hahn Institute

FA flip angle

FAU Friedrich-Alexander-Universität

fb free-breathing

FDA U.S. Food and Drug Administration

FFT fast Fourier transform

FID free induction decay

fMRI functional magnetic resonance imaging

FoV field of view

GRAPPA generalized autocalibrating partially parallel acquisitions

GRE gradient recalled echo

hf head-foot

IDEA integrated developement environment for applications

IEC International Electrotechnical Commission

lr left-right

MRA magnetic resonance angiography

MRF magnetic resonance fingerprinting

MRI magnetic resonance imaging

MRS magnetic resonance spectroscopy

NMR nuclear magnetic resonance

NUFFT non-uniform fast Fourier transform

PE phase encoding

PTB Physikalisch-Technische Bundesanstalt Berlin

pTx parallel transmit

PVP polyvinylpyrrolidone

rect rectangular

RF radiofrequency

RMS root mean squared

RO readout

ROI region of interest

RPE radial phase-encoding

rsos root sum of squares

Rx receive

SAR specific absorption rate

satTFL saturated TurboFLASH

SENSE sensitivity encoding

SNR signal-to-noise ratio

SOM sum of magnitudes

SWI susceptibility weighted imaging

TIAMO time-interleaved acquisition of modes

Tx transmit

UHF ultra-high field

USPIO ultrasmall superparamagnetic particles of ironoxide

VOP virtual observation point

List of Figures

List of Tables

Acknowledgments

Abschließend möchte ich mich bei allen Personen bedanken, die mich während der Promotion begleitet und unterstützt haben. Im Besonderen danke ich

- Prof. Dr. Mark E. Ladd für die Möglichkeit, meine Arbeit in der Abteilung für Medizinische Physik in der Radiologie am Deutschen Krebsforschungszentrum (DKFZ) durchzuführen und für die Vertretung meiner Arbeit gegenüber der Fakultät. Ebenfalls möchte ich mich für die angenehme Atmosphäre bedanken, die in seiner Arbeitsgruppe herrscht.

- Prof. Dr. Leif Schröder für die Übernahme des Zweitgutachtens und auch meiner restlichen Prüfungskommission, Prof. Dr. Blaum und Prof. Dr. Plehn.

- Dr. Sebastian Schmitter für die fantastische Betreuung während der Promotionszeit. Trotz der etwas größeren Entfernung von Berlin nach Heidelberg, waren seine Betreuung und seine Ratschläge sehr wertvoll. Auch konnte ich sehr viel von unseren gemeinsamen Scansessions in Heidelberg mitnehmen und habe viel von Ihm gelernt.

- Dr. Thomas M. Fiedler für die vielen Diskussionen zur Sicherheitsüberwachung der Remote-Spule und deren Validierung. Ebenfalls möchte ich Ihm danken für das Korrekturlesen der Arbeit.

- Dr. Stephan Orzada für die Geduld, die er bei meinen vielen Fragen zum MRExcite System hatte.

- Dr. Simon Schmidt für die konstruktiven Diskussionen zum Ende der Promotionszeit hin und das Korrekturlesen der Arbeit.

- Dr. Sebastian Dietrich für den informativen Austausch zur GRE-RPE Sequenz.

- Dr. Fabian Kratzer für die Einführung in den 7T Scanner und die Beantwortung meiner Fragen am Anfang, trotz dessen, dass er so kurz vor dem Ende seiner Promotion stand.

- Dr. Christoph Aigner für die gemeinsamen Messsessions in Heidelberg und dass er immer zur Verfügung stand, falls ich Fragen hatte.

- Max Lutz für das zur Verfügung stellen der B1-MRF Sequenz und ihrer Rekonstruktion und für die zahlreichen Diskussionen über das B1 mapping.

- Dr. Markus May, Dr. Oliver Kraff und Prof. Dr. Armin Nagel für das bereitwillige zur Verfügung stellen ihrer Spulen und die damit verbundenen Messzeiten in Heidelberg.

- Christian Neelsen, Dr. Daniel Paech und Dr. Johann Jende für die anregenden Konversationen über die klinischen Anforderungen und Anwendungsmöglichkeiten des MRexcite Systems.

- Dr. Steen Moeller für seinen Beispielcode für die SNR Auswertung und die Diskussionen bezüglich der Empfangsauswertung der Spulen.

- meinen HiWis Constantin Schorling und Seraphin Bücklers, die mich mit ihren Fragen stets dazu gebracht haben, mein eigenes Verständis bezüglich MR und den Sequenzen zu überdenken und zu festigen. Die konstruktive Zusammenarbeit hat mir sehr viel Spaß gemacht.

- meinen Kolleginnen und Kollegen in der 7T Gruppe für die schöne Zeit und den vielen Diskussionen während der Mittagspause.

- meinen Freunden, insbesondere Kim-Louis Simmoteit und Oliver Drozdowski für die vielen gemeinsamen Stunden die wir während des Studiums miteinander verbracht haben.

- meinen Eltern und meinen Schwestern für die tatkräftige Unterstützung, den Zuspruch und die Geduld in den letzten Jahren.

- meiner Verlobten Christine, die die letzten fünf Jahre zu den schönsten meines Lebens gemacht hat und mit mir in dieser Zeit durch Höhen und Tiefen gegangen ist.

- meinen beiden Söhnen Matteo und Julian, die ein wundervoller Ausgleich zu meiner Arbeit sind.